

NPS-OC-97-007

# NAVAL POSTGRADUATE SCHOOL MONTEREY, CALIFORNIA



## THESIS

DTIC QUALITY INSPECTED 4

19980417 150

**A LARGE-SCALE MODELING STUDY OF THE  
CALIFORNIA CURRENT SYSTEM**

by

James T. Monroe

December 1997

Thesis Advisor:

Mary L. Batteen

Approved for public release; distribution is unlimited.

Prepared for:  
National Science Foundation  
4201 Wilson Boulevard  
Arlington, VA 22230

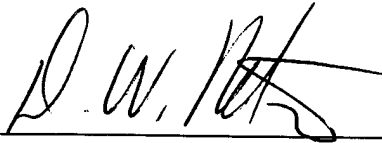
**NAVAL POSTGRADUATE SCHOOL  
MONTEREY, CALIFORNIA**

Rear Admiral Marsha J. Evans  
Superintendent

This thesis was prepared in conjunction with research sponsored in part by the National Science Foundation, 4201 Wilson Boulevard, Arlington, VA 22230.

Reproduction of all or part of this report is authorized.

Released by:



---

David W. Netzer, Associate Provost and Dean of Research

**REPORT DOCUMENTATION PAGE**

Form Approved OMB No. 0704-0188

Public reporting burden for this collection of information is estimated to average 1 hour per response, including the time for reviewing instruction, searching existing data sources, gathering and maintaining the data needed, and completing and reviewing the collection of information. Send comments regarding this burden estimate or any other aspect of this collection of information, including suggestions for reducing this burden, to Washington Headquarters Services, Directorate for Information Operations and Reports, 1215 Jefferson Davis Highway, Suite 1204, Arlington, VA 22202-4302, and to the Office of Management and Budget, Paperwork Reduction Project (0704-0188) Washington DC 20503.

1. AGENCY USE ONLY (Leave blank)		2. REPORT DATE December 1997	3. REPORT TYPE AND DATES COVERED Master's Thesis	
4. TITLE AND SUBTITLE A LARGE-SCALE MODELING STUDY OF THE CALIFORNIA CURRENT SYSTEM			5. FUNDING NUMBERS	
6. AUTHOR(S) Monroe, James T.				
7. PERFORMING ORGANIZATION NAME(S) AND ADDRESS(ES) Naval Postgraduate School Monterey, CA 93943-5000			8. PERFORMING ORGANIZATION REPORT NUMBER NPS-OC-97-007	
9. SPONSORING/MONITORING AGENCY NAME(S) AND ADDRESS(ES) National Science Foundation 4201 Wilson Boulevard Arlington, VA. 22230			10. SPONSORING/MONITORING AGENCY REPORT NUMBER	
11. SUPPLEMENTARY NOTES The views expressed in this thesis are those of the author and do not reflect the official policy or position of the Department of Defense or the U.S. Government.				
12a. DISTRIBUTION/AVAILABILITY STATEMENT Approved for public release; distribution is unlimited.			12b. DISTRIBUTION CODE	
13. ABSTRACT (maximum 200 words) A high-resolution, multi-level, primitive equation ocean model is used to investigate the combined role of wind forcing, thermohaline gradients, and coastline irregularities on the formation of currents, meanders, eddies, and filaments in the California Current System (CCS) from 22.5° N to 47.5° N. An additional objective is to further characterize the formation of the Davidson Current, seasonal variability off Baja California, and the meandering jet south of Cape Blanco. The model includes a realistic coastline and is forced from rest using climatological winds, temperatures, and salinities. The migration pattern of the North Pacific Subtropical High plays a significant role in the generation and evolution of CCS structures. In particular, variations in wind stress induce flow instabilities which are enhanced by coastline perturbations. An inshore train of cyclonic eddies, combined with a poleward undercurrent of varying seasonal depths, forms a discontinuous countercurrent called the Davidson Current north of Point Conception. Off Baja, the equatorward surface jet strengthens (weakens) during spring and summer (fall and winter). Model results also substantiate Point Eugenia as a persistent cyclonic eddy generation area. The model equatorward jet south of Cape Blanco is a relatively continuous feature, meandering offshore and onshore, and divides coastally-influenced water from water of offshore origin.				
14. SUBJECT TERMS Primitive equation model, California Current System, currents, meanders, eddies, filaments			15. NUMBER OF PAGES 148	
			16. PRICE CODE	
17. SECURITY CLASSIFICATION OF REPORT Unclassified	18. SECURITY CLASSIFICATION OF THIS PAGE Unclassified	19. SECURITY CLASSIFICATION OF ABSTRACT Unclassified	20. LIMITATION OF ABSTRACT UL	

NSN 7540-01-280-5500

Standard Form 298 (Rev. 2-89)  
Prescribed by ANSI Std. Z39-18 298-102



Approved for public release; distribution is unlimited.

**A LARGE-SCALE MODELING STUDY OF THE  
CALIFORNIA CURRENT SYSTEM**

James T. Monroe  
Lieutenant Commander, United States Navy  
B.S., United States Naval Academy, 1987

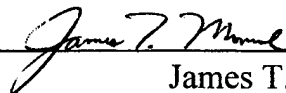
Submitted in partial fulfillment  
of the requirements for the degree of

**MASTER OF SCIENCE IN METEOROLOGY AND PHYSICAL  
OCEANOGRAPHY**

from the

**NAVAL POSTGRADUATE SCHOOL  
December 1997**

Author:



James T. Monroe

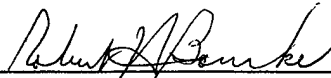
Approved by:



Mary L. Batteen, Thesis Advisor



Curt A. Collins, Second Reader



Robert H. Bourke, Chairman  
Department of Oceanography



## ABSTRACT

A high-resolution, multi-level, primitive equation ocean model is used to investigate the combined role of wind forcing, thermohaline gradients, and coastline irregularities on the formation of currents, meanders, eddies, and filaments in the California Current System (CCS) from 22.5° N to 47.5° N. An additional objective is to further characterize the formation of the Davidson Current, seasonal variability off Baja California, and the meandering jet south of Cape Blanco. The model includes a realistic coastline and is forced from rest using climatological winds, temperatures, and salinities.

The migration pattern of the North Pacific Subtropical High plays a significant role in the generation and evolution of CCS structures. In particular, variations in wind stress induce flow instabilities which are enhanced by coastline perturbations. An inshore train of cyclonic eddies, combined with a poleward undercurrent of varying seasonal depths, forms a discontinuous countercurrent called the Davidson Current north of Point Conception. Off Baja, the equatorward surface jet strengthens (weakens) during spring and summer (fall and winter). Model results also substantiate Point Eugenia as a persistent cyclonic eddy generation area. The model equatorward jet south of Cape Blanco is a relatively continuous feature, meandering offshore and onshore, and divides coastally-influenced water from water of offshore origin.





## TABLE OF CONTENTS

I.	INTRODUCTION .....	1
II.	MODEL DESCRIPTION .....	5
	A. MODEL EQUATIONS .....	5
	B. METHOD OF SOLUTION .....	7
	C. FORCING CONDITIONS AND EXPERIMENTAL DESIGN .....	10
III.	RESULTS .....	13
	A. THE BASIC SIMULATION .....	13
	1. Spin-up Phase .....	14
	2. Quasi-equilibrium Phase .....	20
	B. MODEL SIMULATION APPLICATIONS .....	28
	1. The Davidson Current .....	29
	2. Seasonal Variability Off Baja .....	35
	3. The Meandering Jet South of Cape Blanco .....	42
IV.	SUMMARY .....	45
	LIST OF REFERENCES .....	121
	INITIAL DISTRIBUTION LIST .....	127



## LIST OF FIGURES

1. Model domain, coastline, and generalized classical circulation of the California Current System (CCS). The domain is bounded by 22.5° N to 47.5° N, 107.5° W to 132.5° W. The broad, slow surface equatorward California Current (CC) overlies the narrow, poleward California Undercurrent (CUC). Surface poleward flows include the Davidson Current (DC) north of Point Conception, and the Southern California Eddy (SCE) and Southern California Countercurrent (SCC) south of Point Conception. ....51
2. Climatological winds over the California Current System used to force the model. The climatological (1980-1989) ECMWF winds are shown here for (a) January, (b) April, (c) July, and (d) October. ....52
3. Time series plots of monthly temperature fields used as seasonal forcing in the basic simulation. The '\*' symbol represents data at 22.5° N, 132.5° W, while the '+' symbol represents data at 47.5° N, 132.5° W for levels (a) 13 m and (b) 46 m. ....56
4. Long-term mean atmospheric sea level pressure for January and July over the north Pacific and western North America (From Huyer, 1983). ....58
5. Day 3 density contours and velocity vectors at 13 m depth for (a) the northern half and (b) the southern half of the model domain. Contour interval is 0.1 g/cm<sup>3</sup>; maximum velocity vector is 50 cm/s. In this and the following figures, to avoid clutter, vectors are plotted at every third or fourth grid point in the cross-shore and alongshore directions, and velocities less than 5 cm/s are not plotted. ....59
6. Day 15 density contours and velocity vectors at 13 m depth for (a) the northern half and (b) the southern half of the model domain. Contour interval is 0.1 g/cm<sup>3</sup>; maximum velocity vector is 50 cm/s. ....61
7. Day 45 density contours and velocity vectors at 13 m depth for (a) the northern half and (b) the southern half of the model domain. Contour interval is 0.1 g/cm<sup>3</sup>; maximum velocity vector is 50 cm/s. ....63
8. Cross-shore sections of meridional velocity ( $v$ ) at (a) 40.5° N (off Cape Mendocino) on day 45, and (b) 28.5° N (north of Point Eugenia) on day 105. Contour interval is 2 cm/s in (a) and 1 cm/s in (b). .... 65
9. Day 105 density contours and velocity vectors at depths: (a) and (b) 13 m, and (c) and (d) 316 m for the northern and southern portions of the model domain. Contour interval is 0.1 g/cm<sup>3</sup>; maximum velocity vector is 50 cm/s in (a) and (b), and 20 cm/s in (c) and (d)...67
10. Day 195 density contours and velocity vectors at depths: (a) and (b) 13 m, and (c) and (d) 316 m for the northern and southern portions of the model domain. Contour interval is 0.2 g/cm<sup>3</sup> in (a) and (b), and 0.1 g/cm<sup>3</sup> in (c) and (d); maximum velocity vector is 50 cm/s in (a) and (b) and 20 cm/s in (c) and (d). ....71
11. Cross-shore sections of  $v$  at (a) 46° N (off northern Oregon) and (b) 25° N (off Cape San Lazaro) on day 195. The contour interval is 2.5 cm/s (5 cm/s) for poleward (equatorward) flow.....75

12. Cross-shore sections of $v$ at (a) $25^\circ$ N (off Cape San Lazaro), (b) $29^\circ$ N (north of Point Eugenia), (c) $32.5^\circ$ N (Southern California Bight), (d) $36.5^\circ$ N (off Point Sur), and (e) $43^\circ$ N (off Cape Blanco) on day 285. The contour interval is 2.5 cm/s (5 cm/s) for poleward (equatorward) flow. ....	77
13. Day 300 density contours and velocity vectors at 13 m depth for the northern portion of the domain from $42^\circ$ N to $46^\circ$ N. Contour interval is $0.1 \text{ g/cm}^3$ ; maximum velocity vector is 30 cm/s. ....	82
14. Day 300 density contours and velocity vectors at (a) 13 m and (b) 316 m depth for the central portion of the domain from $32^\circ$ N to $39.5^\circ$ N. The contour interval is $0.2 \text{ g/cm}^3$ in (a) and $0.1 \text{ g/cm}^3$ in (b). Maximum velocity vector is 50 cm/s. ....	83
15. Cross-shore sections of mean $v$ for January of model year 3 at (a) $44.2^\circ$ N (off Oregon), (b) $41.6^\circ$ N (off northern California), (c) $34.2^\circ$ N (south of Point Conception), and (d) $26.3^\circ$ N (south of Point Eugenia). The contour interval is 2.5 cm/s (5 cm/s) for poleward (equatorward) flow. ....	85
16. Cross-shore sections of mean $v$ for July of model year 3 at (a) $44.2^\circ$ N (off Oregon), (b) $41.6^\circ$ N (off northern California), (c) $34.2^\circ$ N (south of Point Conception), and (d) $26.3^\circ$ N (south of Point Eugenia). The contour interval is 2.5 cm/s (5 cm/s) for poleward (equatorward) flow. ....	89
17. Horizontal maps at 13 m depth of (a) mean kinetic energy (MKE), and (b) eddy kinetic energy (EKE) for July of model year 3. Contour interval is $200 \text{ cm}^2/\text{s}^2$ in (a) and $100 \text{ cm}^2/\text{s}^2$ in (b). ....	93
18. Cross-shore sections of mean $v$ for January of model year 3 at (a) $36.5^\circ$ N (off Point Sur) and (b) $34.6^\circ$ N (off Point Conception), and June at (c) $36.5^\circ$ N and (d) $34.6^\circ$ N. The contour interval is 2.5 cm/s (5 cm/s) for poleward (equatorward) flow in (a, c, d) and 4 cm/s (5 cm/s) for poleward (equatorward) flow in (b). ....	95
19. Cross-shore sections of mean $v$ for November of model year 3 at (a) $33.5^\circ$ N (south of Point Conception), (b) $34.6^\circ$ N (off Point Conception), and (c) $35.5^\circ$ N (north of Point Conception). The contour interval is 2.5 cm/s (5 cm/s) for poleward (equatorward) flow. ....	99
20. Cross-shore sections of mean $v$ at $32^\circ$ N for (a) August, (b) September, (c) October, and (d) November of model year 3. The contour interval is 1 cm/s (5 cm/s) for poleward (equatorward) flow in (a) and 2.5 cm/s (5 cm/s) for poleward (equatorward) flow in (b, c, d). ....	102
21. Cross-shore sections of (a) salinity on day 924 (mid-July) and (b) mean $v$ for July of model year 3 at $26^\circ$ N (south of Point Eugenia). The contour interval is 0.1 ppt in (a) and 2.5 cm/s (5 cm/s) for poleward (equatorward) flow in (b). ....	106
22. Cross-shore sections of (a) salinity on day 750 (mid-January) and (b) mean $v$ for January of model year 3 at $30.5^\circ$ N (off northern Baja). The contour interval is 0.1 ppt in (a) and 2.5 cm/s (5 cm/s) for poleward (equatorward) flow in (b). ....	108

23. Cross-shore sections of mean  $v$  at  $25^\circ$  N (off Cape San Lazaro) for (a) January, (b) April, (c) July, and (d) October of model year 3. The contour interval is 2.5 cm/s (5 cm/s) for poleward (equatorward) flow in (a, b, d) and 5cm/s for both in (c). .....110

24. Cross-shore sections of (a)  $v$  and (b) salinity on day 834 (mid-April) of model year 3 at  $29.9^\circ$  N (off Point Baja). The contour interval is 2.5 cm/s (5 cm/s) for poleward (equatorward) flow in (a) and 0.1 ppt in (b). .....114



## LIST OF PLATES

1. Mean temperature and velocity vectors at 13 m depth for (a) January, (b) April, (c) July, and (d) October of model year 3. Contour interval is  $0.1^{\circ}$  C; maximum velocity vector is 100 cm/s. ....116





## LIST OF TABLES

1. Values of Constants Used in the Model.....	120
---	-----



## ACKNOWLEDGEMENT

I would like to extend my sincere appreciation to a handful of individuals without whom this effort would have been a monumental struggle. First and foremost, thanks goes out to my advisor, Dr. Mary Batteen, for her professional guidance and advice which always kept me focused in the right direction. Her substantial knowledge surrounding the California Current System was the single most important ingredient to the success of this study.

Huge thanks as well to Pete Braccio, Mike Cook, and Phaedra Green who were always available to provide crucial assistance with programming and graphics hurdles, of which there were many. Additionally, the constructive advice provided by Dr. Curt Collins, as second reader, was greatly appreciated.

Above all, a special thank you to my wife, whose steadfast love and patience have seen me through the past two and a half years. With her at my side any goal seems attainable.

Thank you!



## I. INTRODUCTION

The California Current System (CCS) is a classical eastern boundary current (EBC) system located off the west coast of North America extending approximately from the Strait of Juan de Fuca southward to the tip of the Baja Peninsula (Hickey, 1997). As in other EBC regimes, satellite infrared sea surface temperature (SST) imagery of the CCS has revealed a distinct complex flow structure with seasonal variations. Dominant mechanisms responsible for the observed large-scale structure within the CCS have been shown to be seasonal variations in alongshore wind stress (Bakun and Nelson, 1991), coastline irregularities (e.g., Batteen, 1997), bottom topography (e.g., Ikeda *et al.*, 1984), and temperature and salinity variations (Batteen *et al.*, 1995; Batteen and Vance, 1997).

In the mean, the greater CCS is comprised of several large-scale currents (Figure 1). The basic flow is a broad (~1000 km offshore), shallow (surface to ~500 m), slow (~10 cm/s), year-round equatorward current known as the California Current (CC). Embedded within this basic flow are the California Undercurrent (CUC), the Davidson Current (DC), the Southern California Countercurrent (SCC), and the Southern California Eddy (SCE). The CUC is a relatively narrow (~10-40 km width), weak (~2-10 cm/s), subsurface poleward flow which is strongest at ~100-300 m depth and varies seasonally. The DC is a weak, inshore, poleward surface flow north of Point Conception during fall and winter. Other poleward surface flows include the SCC south of Point Conception

and the SCE shoreward of the Channel Islands within the Southern California Bight (Hickey, 1979, 1997).

Within the mean, large-scale structure of the CCS there exist perturbations in the form of mesoscale meanders, eddies, filaments, and jets which vary in both space and time (Bernstein *et al.*, 1977; Chelton, 1984; Strub *et al.*, 1991). Recent numerical modeling efforts by Batteen *et al.* (1989) and Batteen (1997) successfully simulated this complex eddy-mean flow interaction within the CCS using a high-resolution, multi-level, primitive equation (PE) ocean model emphasizing the role of wind-forcing and coastline irregularities. Specifically, the seasonal variation of the alongshore component of wind stress was critical in generating realistic horizontal and vertical structures for the surface equatorward CC and the subsurface poleward CUC. Both baroclinic and barotropic instability contributed to the generation of meanders, filaments, and eddies. Additionally, coastline irregularities were shown to help “anchor” upwelling filaments and enhance the growth of meanders and eddies. In particular, the region off Cape Blanco was identified as the location where the CC leaves the coast and develops a meandering jet to the south. In recent studies on the combined effect of temperature and salinity on density, Batteen *et al.* (1995) and Batteen and Vance (1997) concluded that the distribution of salinity as well as temperature is important in defining the large-scale structure and circulation of the CCS.

Here we expand the process-oriented model of Batteen (1997) to include the entire CCS region, building upon previous studies which were restricted poleward of 35°

N. We examine the ability of the model to successfully simulate the known current structure using seasonal wind forcing, temperature and salinity gradients and a realistic coastline. An additional focus of this research is to utilize model results to contribute to the discussion and characterization of certain key issues and unknowns regarding the CCS raised by Hickey (1997) in a recent comprehensive description of the greater CCS. Here we briefly highlight three of the issues, described by Hickey (1997) as poorly understood, unknown, or unexplained, to be addressed in the present study.

First, is the DC the result of the CUC surfacing (Pavlova, 1966; Huyer and Smith, 1974) or due to the SCC successfully rounding Point Conception? Hickey (1997) maintains that the CUC has a seasonal maxima in summer to early fall while the SCC has a seasonal maxima in winter, coincident with the development of the DC. One objective of this modeling study is to reproduce and further define the relationship between the DC, CUC, and SCC/SCE.

Next, what is the seasonal variability of large-scale and coastal currents off the Baja Peninsula? Hickey (1997) states that due to few direct current observations, the seasonal cycle over the southern Baja Peninsula coastal region is unknown at the present time and the existence of mesoscale features suggests that the circulation may be complex. A second objective of this study is to use the model with the aforementioned wind forcing, temperature and salinity gradients in conjunction with a realistic Baja coastline to better define current structure and variability in this area.

Finally, Hickey (1997) recommends, as an area of future research, investigation of the relationship between the meandering jet that originates near Cape Blanco and jets and filaments that originate near other coastal promontories. In the present study, we inquire if the Cape Blanco jet is a continuous feature and examine its role in the large-scale CCS.

This study is organized as follows: the PE model and experimental conditions used in the basic study are presented in section II. Results and model simulation applications are described in section III. A summary is presented in section IV.



## II. MODEL DESCRIPTION

### A. MODEL EQUATIONS

The PE model in this study was originally a coarse resolution model used in closed basin studies by Haney (1974). It has recently been adapted by Batteen (1997) for eddy-resolving, limited EBC regions with open boundaries to the north, south, and west. The model is multi-level, non-adiabatic, and uses the beta-plane approximation. It has both baroclinic and barotropic velocity components and uses the hydrostatic and Boussinesq approximations as well as a rigid lid. The governing equations are as follows:

$$\frac{du}{dt} = \frac{-1}{\rho_0} \frac{\partial p}{\partial x} + fv - A_M \nabla^4 u + K_M \frac{\partial^2 u}{\partial z^2} \quad (1)$$

$$\frac{dv}{dt} = \frac{-1}{\rho_0} \frac{\partial p}{\partial y} - fu - A_M \nabla^4 v + K_M \frac{\partial^2 v}{\partial z^2} \quad (2)$$

$$\frac{\partial u}{\partial x} + \frac{\partial v}{\partial y} + \frac{\partial w}{\partial z} = 0 \quad (3)$$

$$\frac{\partial p}{\partial z} = -\rho g \quad (4)$$

$$\rho = \rho_0 [1 - \alpha(T - T_0) + \beta(S - S_0)] \quad (5)$$

$$\frac{dT}{dt} = -A_H \nabla^4 T + K_H \frac{\partial^2 T}{\partial z^2} \quad (6)$$

$$\frac{dS}{dt} = -A_H \nabla^4 S + K_H \frac{\partial^2 S}{\partial z^2} \quad (7)$$

In the above equations,  $t$  is time and  $(x,y,z)$  is a right-handed Cartesian coordinate system with  $x$  pointing toward shore,  $y$  alongshore, and  $z$  upward. The corresponding velocity components are  $(u,v,w)$ .  $T$ ,  $S$ , and  $p$  are temperature, salinity and pressure, respectively, and  $\rho$  is density. Table 1 provides a list of other symbols found in the model equations, as well as values of constants used throughout the study.

A space-staggered B-scheme (Arakawa and Lamb, 1977) is used for the horizontal finite differencing. This scheme has been shown by Batteen and Han (1981) to be appropriate when grid spacing is approximately the same order as, or less than, the Rossby radius of deformation. The horizontal grid spacing is 9 km in the east-west direction and 11 km in the north-south direction, while the internal Rossby radius of deformation is  $\sim 30$  km.

The model uses ten vertical layers, with constant z-levels, at depths of 13, 46, 98, 182, 316, 529, 870, 1416, 2283, and 3656 m. This vertical scheme is designed to concentrate more layers above the thermocline in the dynamically active portion of the ocean, consistent with Haney (1974).

The model domain (Figure 1) encompasses the west coast of the United States and the Baja Peninsula, from  $22.5^\circ$  N to  $47.5^\circ$  N (2816 km alongshore), and from  $107.5^\circ$  W to  $132.5^\circ$  W offshore (2304 km cross-shore). The coastal boundary of the model domain is closed, and has both tangential and normal velocity components set to zero. To isolate the role of wind forcing from the possible coupled effect of wind forcing and topography (which will be considered in a separate study), bottom topography has been omitted and

the eastern boundary is modeled as a vertical wall. The constant depth used in the model is 4500 m. A modified version of the radiation boundary conditions of Camerlengo and O'Brien (1980) is used for the open boundaries to the north, south, and west with some spatial smoothing applied in the vicinity of these boundaries (Batteen, 1997).

Biharmonic lateral heat and momentum diffusion is used in the model with the same choice of coefficients (i.e.,  $2.0 \times 10^{17} \text{ cm}^4/\text{s}$ ) as in Batteen (1997). Holland (1978) showed that biharmonic diffusion acts predominantly on submesoscales, while Holland and Batteen (1986) found that baroclinic mesoscale processes can be damped by Laplacian lateral heat diffusion. As a result, the use of biharmonic lateral diffusion should allow mesoscale eddy generation via barotropic (horizontal shear) and/or baroclinic (vertical shear) instability mechanisms. As in Batteen (1997), weak ( $0.5 \text{ cm}^2/\text{s}$ ) vertical eddy viscosities and conductivities are used and bottom stress is parameterized by a simplified quadratic drag law (Weatherly, 1972).

## **B. METHOD OF SOLUTION**

Equations (1) through (7) comprise a closed system of seven scalar equations and seven unknowns,  $u$ ,  $v$ ,  $w$ ,  $p$ ,  $\rho$ ,  $T$ , and  $S$ . The variables,  $u$ ,  $v$ ,  $T$ , and  $S$  are prognostic variables whose time rates of change are predicted from (1), (2), (6) and (7), respectively. Although the diagnostic variables  $w$ ,  $p$ , and  $\rho$  can be determined from (3), (4), and (5), respectively, additional constraints are imposed on  $p$  and  $w$  by the choice of the rigid lid

boundary condition. Specifically, the vertically integrated pressure can no longer be obtained by integrating the hydrostatic equation (4) for the free surface, and the vertically-integrated horizontal velocity is subsequently constrained to be non-divergent,

$$\text{i.e.,} \quad \int_H^0 \left( \frac{\partial u}{\partial x} + \frac{\partial v}{\partial y} \right) d\varepsilon = 0, \quad (8)$$

which is obtained by integrating (3) and applying the vertical boundary conditions where  $\varepsilon$  is a dummy variable representing the vertical coordinate.

For any quantity  $q$ , let its vertical average be denoted by  $\bar{q}$  and its departure (vertical shear) by  $q'$ . From (8) the vertical mean flow can then be described by a stream function  $\psi$ , such that:

$$\bar{u} = -\frac{1}{H} \frac{\partial \psi}{\partial y}, \quad (9)$$

$$\bar{v} = \frac{1}{H} \frac{\partial \psi}{\partial x}. \quad (10)$$

The stream function  $\psi$  is predicted from the vorticity equation, which is derived from the vertical average of (1) and (2). Applying the curl operator and using (9) and (10) the vorticity equation becomes

$$\begin{aligned}
\frac{\partial \zeta}{\partial t} &= \frac{\partial}{\partial t} \left[ \frac{1}{H} \left( \frac{\partial^2 \psi}{\partial x^2} \right) + \frac{1}{H} \left( \frac{\partial^2 \psi}{\partial y^2} \right) + \frac{\partial \psi}{\partial x} \frac{\partial H^{-1}}{\partial x} + \frac{\partial \psi}{\partial y} \frac{\partial H^{-1}}{\partial y} \right] \\
&= - \left[ \frac{\partial}{\partial x} \left( \frac{f}{H} \frac{\partial \psi}{\partial y} \right) - \frac{\partial}{\partial y} \left( \frac{f}{H} \frac{\partial \psi}{\partial x} \right) \right] \\
&\quad - \left[ \frac{\partial}{\partial x} \left( \frac{g}{H \rho_0} \int_H^0 \int_z^0 \frac{\partial \rho}{\partial y} d\epsilon dz \right) - \frac{\partial}{\partial y} \left( \frac{g}{H \rho_0} \int_H^0 \int_z^0 \frac{\partial \rho}{\partial x} d\epsilon dz \right) \right] \\
&\quad + \frac{\partial}{\partial x} \left( \frac{1}{H} \int_H^0 G dz \right) - \frac{\partial}{\partial y} \left( \frac{1}{H} \int_H^0 F dz \right),
\end{aligned} \tag{11}$$

where  $G$  and  $F$  represent the collective contributions of nonlinear and viscous terms from equations (1) and (2).

The vorticity equation (1) is solved by obtaining an updated value of  $\zeta$  by applying the leapfrog (or every 11 time steps, the Euler-backward) time-differencing scheme. The associated value of  $\psi$  can then be obtained from:

$$\zeta = \frac{1}{H} \left( \frac{\partial^2 \psi}{\partial x^2} \right) + \frac{1}{H} \left( \frac{\partial^2 \psi}{\partial y^2} \right) + \frac{\partial \psi}{\partial x} \frac{\partial H^{-1}}{\partial x} + \frac{\partial \psi}{\partial y} \frac{\partial H^{-1}}{\partial y}, \tag{12}$$

which is an elliptic equation. A solution to (1) is fully prescribed by specifying the values of  $\psi$  on the open and closed boundaries of the model domain. Currently, to solve (1), the model uses successive over-relaxation techniques.

The vertical shear current ( $u'$ ,  $v'$ ) is predicted from (1) and (2) after subtracting the vertical mean flow. The results are:

$$\frac{\partial u'}{\partial t} = \frac{-1}{\rho_0} \frac{\partial u'}{\partial x} + f v' - A_M \nabla^4 u' + K_M \frac{\partial^2 u'}{\partial x^2} + F - \bar{F} - \frac{\tau^y}{\rho_0 H}, \tag{13}$$

$$\frac{\partial v'}{\partial t} = \frac{-1}{\rho_0} \frac{\partial v'}{\partial y} - f u' - A_M \nabla^4 v' + K_M \frac{\partial^2 v'}{\partial y^2} + G - \bar{G} - \frac{\tau^x}{\rho_0 H}. \tag{14}$$

In (13) and (14),  $p'$ , which represents the departure of the pressure from the vertical average, is, using (4), expressed in terms of  $\rho$  as:

$$p' = \int_z^0 \rho g d\varepsilon - \frac{1}{H} \int_{-H}^0 \left( \int_z^0 \rho g d\varepsilon \right) dz. \quad (15)$$

The method of solution consists of predicting  $\nabla^2 \psi, \psi, u', v', T$ , and  $S$  from (11), (12), (13), (14), (6) and (7), respectively. The total current is then obtained by adding the vertical shear part to the vertical average part, after the latter is obtained from  $\psi$  using (9) and (10). The diagnostics  $\rho$ ,  $w$ , and  $p'$  are then obtained explicitly from the equation of state (5), continuity equation (8), and hydrostatic relation (15) respectively.

### C. FORCING CONDITIONS AND EXPERIMENTAL DESIGN

Previous experiments by Batteen *et al.* (1989) investigated the role of steady alongshore, upwelling-favorable winds, with and without alongshore variability, on the generation of features in the CCS. More recently, Batteen (1997) studied the contributions of seasonal wind forcing and irregular coastline geometry to the generation of eddies, jets and filaments in the CCS between 35° N and 47.5° N. Following Batteen (1997), in this study, seasonal wind forcing, temperature and salinity variations, and irregular coastline geometry will be used to investigate the generation of similar features throughout the entire CCS.

To explore the effects of seasonal wind forcing, the model is forced from rest with climatological wind fields from a  $2.5^\circ$  by  $2.5^\circ$  grid of European Centre for Medium-Range Weather Forecasts (ECMWF) near-surface wind analyses (Trenberth *et al.*, 1990). The monthly mean stresses based on twice daily wind analyses from 1980-1989 have been interpolated spatially to the 9 by 11 km model resolution and temporally to daily wind values.

Sample wind fields used in the basic study are shown in Figure 2, which depicts the seasonal influence and migration of flow around the North Pacific Subtropical High over the area encompassed by the model domain. Figure 2a shows a divergence of flow at the coast in the vicinity of Cape Mendocino (see Figure 1 for geographical locations) during winter as winds circulate anticyclonically around the Subtropical High to the south and cyclonically around the Aleutian Low to the north. By spring (Figure 2b), the Subtropical High has begun its westward and northward expansion, producing increased equatorward winds over most of the model domain and causing the divergence of flow to move north off the Washington coast. In July (Figure 2c), equatorward, upwelling-favorable winds dominate along the entire coastline as the Subtropical High reaches its maximum extent. Figure 2d shows a decrease in magnitude of equatorward winds during fall as the Subtropical High once again begins to recede southward.

The effects of thermohaline gradients in the CCS are included using monthly temperature and salinity climatology from Levitus *et al.* (1994) and Levitus and Boyer (1994) to initialize the model, and once a day to force the model at the western boundary

(132.5° W). Forcing occurs over the upper seven levels, which are initially assumed to be zonally homogeneous. Since the lower three levels do not exhibit significant horizontal variation in temperature and salinity, constants are assumed for each level. Temperature values used for levels 8, 9, and 10 are 2.56° C, 2.08° C, and 2.00° C, respectively, while the salinity constant used for the lower three levels is 34.7. Only the upper layer (13 m and 46 m) temperature forcing conditions for the northern (47.5° N) and southern (22.5° N) boundaries show significant seasonal variability with a temperature maximum in late summer to early fall and minimum in late winter to early spring throughout the region (Figure 3a and 3b). Below these depths, both the seasonal temperature fluctuations and temperature gradient weaken. Conversely, salinity forcing conditions at all seven levels, which show less (more) saline water to the north (south), have no significant seasonal cycle (not shown).

The design of the basic study is as follows. To focus on the combined role of seasonal wind forcing and thermohaline gradients, model integrations start from a state of rest and once a day the model is updated with ECMWF winds and, at the western boundary with temperature and salinity. Additionally, a realistic North American coastline is used to include the effects of irregular coastline geometry over the entire CCS region. To allow the model to reach a state of quasi-equilibrium, the experiment is run for three years.



### III. RESULTS

#### A. THE BASIC SIMULATION

Before interpreting the model response to climatological wind forcing and thermohaline gradients, it is first important to review the mean atmospheric and oceanic regimes in the CCS region. The atmospheric circulation over the greater CCS is dominated by the relative positions and intensities of the North Pacific Subtropical High, the Aleutian Low, and the pressure pattern over the western North American continent which vary seasonally (Figure 4). In winter, the Subtropical High weakens and migrates equatorward while strong high pressure dominates over the cold continental land mass. The Aleutian Low deepens and extends equatorward, influencing most of the extreme northern Pacific. Conversely, during summer the Subtropical High builds and migrates poleward while surface pressures over the southwestern U.S. and northern Mexico are dominated by a thermal low. As a result, the offshore pressure gradient over most of the CCS is strongest in summer (Huyer, 1983).

The CCS is also influenced by at least three different watermasses. Cold, low salinity Pacific Subarctic Water is advected from the north while warmer, more saline North Pacific Central Water enters from the west. Warm, high salinity Southern Water is advected from the south by the poleward undercurrent (Hickey, 1997). Unlike other eastern boundary currents, salinity increases rather than decreases with depth in the CCS (Wooster and Reid, 1963).

## 1. Spin-up Phase

The model is initiated under wintertime forcing conditions with the first model day corresponding to the first day of January. By model day 3, there is a general trend of density decreasing equatorward over the entire domain. In the northern portion of the domain, the density gradient is stronger due to a stronger temperature gradient present in the midlatitude regime (Figure 5a). The southern half of the domain encompasses a subtropical environment where temperature, and thus density, gradients are weaker (Figure 5b). In January, wind forcing over the CCS is affected by the pressure gradient between the Aleutian Low to the north and the Subtropical High, adjacent to stronger high pressure over a cold continent, in the south (Figure 4). These conditions result in a horizontal pressure gradient force from south to north that, when balanced by Coriolis, produces a generally onshore geostrophic flow in the interior ocean. As the flow approaches the eastern boundary it turns poleward, except in the extreme south where there are persistent northwesterly winds from the Subtropical High year-round. As seen in Figures 5a and 5b, this alongshore flow increases in magnitude to the north due to a stronger density gradient, and decreases to the south as the density gradient weakens. By day 15, the surface poleward boundary current in the midlatitude portion of the model domain (Figure 6a) advects warmer, less dense water from the south at maximum speeds of  $\sim 30\text{-}50$  cm/s alongshore. To the south below about  $31.5^\circ$  N (Figure 6b), the flow turns equatorward at the coast, advecting cooler, more dense water from the north at speeds of  $\sim 2\text{-}5$  cm/s.

Perturbations in the density field nearshore become more pronounced in the vicinity of coastal promontories by day 45 as warmer, less dense water is advected poleward at maximum speeds of  $\sim 30$  cm/s above  $35^\circ$  N (Figure 7a), and cooler, more dense water is advected equatorward at maximum speeds of  $\sim 15$  cm/s below  $35^\circ$  N (Figure 7b). Poleward current speeds increase to the north as flow at the eastern boundary is continuously augmented by onshore geostrophic flow from the interior ocean. Equatorward flow in the south is largely driven by circulation around the Subtropical High which at day 45 (mid-February), has migrated to its most southerly position,  $\sim 28^\circ$  N,  $130^\circ$  W (Huyer, 1983). An anticyclonic eddy in the vicinity of Point Conception roughly marks the division of the flow field (Figure 7b). Cross-sections of meridional velocity taken to the north and south show predominantly poleward flow in the north off Cape Mendocino with an inshore equatorward flow increasing with depth (Figure 8a), and predominantly equatorward flow in the south, at  $28.5^\circ$  N, with inshore poleward flow increasing with depth (Figure 8b).

By day 105, which corresponds to mid-April of model year one, wind forcing is in transition as the Aleutian Low retreats poleward and the Subtropical High advances toward its summertime position and strengthens. Consequently, the surface flow field responds as equatorward flow alongshore extends farther to the north and strengthens while poleward flow in the north begins to retreat and weaken (Figures 9a and 9b). Development of anticyclonic eddies occurs off northern California and Oregon as the mass field adjusts to the transitional flow regime, i.e., the Subtropical High ridging

northward (Figure 9a). These eddies extend well below the surface to a depth of 316 m (Figure 9c). In the south (Figure 9b), a density front develops along the coast with the highest density water inshore, where northwesterly winds parallel the coastline, due to upwelling of cooler water from below. At 316 m depth, an inshore poleward flow of ~2-10 cm/s is present over the southern portion of the domain (Figure 9d). Seaward of this poleward undercurrent the nearshore flow remains equatorward. A cyclonic meander is present in the vicinity of Point Eugenia (Figure 9b) coincident with the location of maximum poleward undercurrent velocities (Figure 9d).

Batteen (1997) noted that barotropic and baroclinic instabilities in the surface flow and undercurrent result in the generation of meanders, filaments, and eddies. The dynamical reasons for the generation and stability of the eddies described above are examined using the techniques described by Batteen *et al.* (1992). From energy transfer analysis, the location and magnitude of baroclinic and barotropic transfers can be found and examined to argue for the type of instability mechanism (e.g., barotropic, baroclinic, or mixed) which leads to initial eddy generation.

Model days 15 (Figure 6a) and 45 (Figure 7a) show the initial development of nearshore anticyclonic meanders in the northern portion of the model domain between ~38° N-44° N, which culminates in the alongshore anticyclonic eddies present in the same vicinity by day 105 (Figure 9a). Likewise, in the southern half of the domain, day 105 (Figure 9b) shows a cyclonic meander north of Point Eugenia at ~28.5° N, which leads to offshore cyclonic eddy activity by day 195 (Figure 10b).

Figures 8a (day 45 for the northern region) and 8b (day 105 for the southern region) show that horizontal and vertical current shear exists in both regions with varying intensities. Barotropic instability can result from horizontal current shear, while baroclinic instability can result from vertical shear in the currents. Thus, both types of instability (i.e., mixed) may be present simultaneously. Energy transfer analyses, based on Batteen *et al.* (1992), which consist of barotropic (mean kinetic energy to eddy kinetic energy) and baroclinic (mean potential energy to eddy potential energy to eddy kinetic energy) components, were performed over the period of meander and eddy development for the locations described above.

Results from the instability analysis for days 30 to 45 (not shown) show that in the northern portion of the domain, off Cape Mendocino, both barotropic and baroclinic instability (i.e., mixed) play a significant role in the development of anticyclonic meanders, which ultimately results in the field of anticyclones seen by day 105 (Figure 9a). This analysis is consistent with Figure 8a, which portrays both vertical and horizontal upper layer current shear. In contrast, at  $28.5^{\circ}$  N, in the vicinity of Point Eugenia, the instability analysis for days 93 to 120 (not shown) shows baroclinic instability to be the dominant generation mechanism for cyclonic meander development, which ultimately leads to the formation of a cyclonic eddy by day 195 (Figure 10b). This analysis is consistent with Figure 8b which shows a relatively stronger vertical than horizontal gradient in upper layer current shear at the time of the initial instability.

During summer, north to northwesterly (i.e., upwelling-favorable) wind forcing increases in magnitude as the entire CCS is under the influence of return circulation around the Subtropical High. Additionally, the pressure gradient between the Subtropical High offshore and the thermal low over the southwestern U.S. and northern Mexico is a maximum (Figure 4), resulting in enhanced upwelling over the model domain south of Point Sur. By day 195, surface equatorward flow is present all along the coast with cold, dense, upwelled water inshore south of Point Sur where the coastline approximately parallels the wind direction (Figures 10a and 10b).

Production of anticyclonic eddies in the northern part of the domain has subsided by day 195 as coastal flow adjusts to northerly wind forcing around the Subtropical High. The eddy field which extended to either side of Cape Mendocino during April has propagated westward and has coalesced into a large region of anticyclonic turning offshore (Figure 10a). Meander activity has increased to the south, with cyclonic eddies forming south of Point Conception and north and south of Point Eugenia (Figure 10b). An equatorward coastal jet is discernible as a relatively narrow coastal flow in the north, which broadens in scope as it progresses southward. Maximum speeds in the northern half of the domain are  $\sim 20$  cm/s whereas current speeds associated with cyclonic eddy activity in the south are  $\sim 30$ - $50$  cm/s. Similarly, the inshore poleward flow at 316 m depth seen in April has increased dramatically in the south (maximum speeds  $\sim 15$ - $20$  cm/s) and can be traced northward across the entire model domain (Figure 10c and 10d). A cross-section of meridional velocity at the extreme northern portion of the domain

(Figure 11a) shows that the poleward flow, with velocities of  $\sim 7.5$  cm/s, has migrated offshore. Inshore equatorward flow, with velocities of  $\sim 20$  cm/s, overlies a poleward undercurrent with velocities of  $\sim 2.5$  cm/s below  $\sim 300$  m depth. A cross-section of meridional velocity off Cape San Lazaro in the extreme south (Figure 11b), shows that the surface equatorward flow is more intense, extends further offshore, and is shallower than its northern counterpart. Additionally, a poleward undercurrent with a core velocity of  $\sim 7.5$  cm/s, at  $\sim 325$  m depth, is present.

In the fall, the Aleutian Low begins to deepen and the Subtropical High migrates toward its wintertime position in the south. With this transition, poleward wind stress returns to the northern portion of the model domain as the regional pressure gradient strengthens. By day 285, which corresponds to mid-October, poleward flow at the coast shows significant trends of fluctuating depth and intensity (Figures 12a-12e). Off Cape San Lazaro, a strong poleward undercurrent is centered below  $\sim 300$  m depth with speeds up to  $\sim 15$  cm/s (Figure 12a). North of Point Eugenia this poleward flow surfaces and weakens (Figure 12b). At  $32.5^\circ$  N, within the Southern California Bight, the poleward undercurrent is weak, broad, and confined below  $\sim 250$  m depth (Figure 12c). North of Point Conception in the vicinity of Point Sur, the coastal undercurrent strengthens, with a maximum of  $\sim 10$  cm/s below  $\sim 500$  m depth (Figure 12d). Further north, off Cape Blanco, poleward flow is once again present throughout the water column at the coast with a core velocity of  $\sim 7.5$  cm/s centered at  $\sim 320$  m depth (Figure 12e).

Since the model is nonlinear, producing mesoscale meanders and eddies, the return of the pressure gradient force and poleward wind stress in the north does not initiate an immediate flow field response in the same direction. Rather, above Cape Blanco ( $\sim 43^\circ$  N) by day 300 (Figure 13), the alongshore maximum in equatorward flow is observed to have moved farther westward from its coastal position seen at day 195 (Figure 10a). This results in a more pronounced alongshore density gradient with higher density water penetrating farther equatorward into the model interior as the blocking effect of the Subtropical High lessens in the north. Thus, as the equatorward jet at the coast decreases in intensity, upwelling-favorable transport diminishes, resulting in a tongue of low density water adjacent to the northern Oregon coastline seen in Figure 13. Equatorward of Point Arena at day 300 (Figure 14a), the highest density water is again adjacent to the coast, coincident with equatorward wind forcing still under the dominant influence of circulation around the Subtropical High. Between days 195 (Figures 10a-10d) and 300 (Figures 14a and 14b), there has been a substantial increase in meander activity, and, in the Southern California Bight, a cyclonic, cold-core eddy has developed and extends to  $\sim 316$  m depth (Figure 14b).

## **2. Quasi-equilibrium Phase**

Longer run times ( $\sim 3$  years) with model output fields averaged every 3 days for the months of January, April, July, and October illustrate the seasonal variability and complex structure of the CCS. By year 3, the model CC core is embedded with numerous eddies, meanders, and upwelling filaments (Plates 1a-1d), which is shown in



section III.B to be consistent with real-world observations (e.g., Lynn and Simpson, 1987). Although the mean direction of flow remains equatorward near the surface, the circulation contains large zonal components with intense onshore and offshore transports.

Model results show that in winter (Plate 1a), flow at the coast meanders equatorward, increasing in velocity where the flow turns anticyclonic toward the coast and decreasing in intensity where it is directed cyclonically offshore. These coastal meanders in the flow field advect colder water near the coast offshore and warmer water from the west onshore throughout the model domain. Both cyclonic and anticyclonic eddies exist on either side of the equatorward coastal jet and closed, cold-core eddies of  $O(100 \text{ km})$  diameter are present off San Francisco at  $\sim 38.5^\circ \text{ N}$ ,  $127^\circ \text{ W}$ , and in the southwest corner of the domain at  $\sim 25.5^\circ \text{ N}$ ,  $127.5^\circ \text{ W}$ . The coldest water found in the model is located adjacent to the southern Baja coastline coincident with persistent northwesterly winds due to the wintertime position of the Subtropical High (Figure 2a). Average current speeds of the equatorward surface jet range from  $\sim 10\text{-}50 \text{ cm/s}$ , consistent with observations of the CC using drifters (Davis, 1985).

In spring (Plate 1b), meander activity is more pronounced along the model coastline and more closed eddies exist offshore within the core of the equatorward model CC. Eddies present in January have propagated westward at speeds of  $\sim 1\text{-}3 \text{ km/day}$ , consistent with Rossby wave propagation speeds. The coldest water has moved north up the Baja and Southern California coastline in conjunction with the seasonal migration of the Subtropical High and subsequent expansion of upwelling-favorable winds. Similarly,

in the model, spring marks an increase in magnitude of the equatorward surface jet from speeds present in January. Using CalCOFI data, Lynn and Simpson (1987) noted that a large-scale intensification in equatorward flow along much of the coastal CCS accompanied the onset of springtime conditions.

In summer (Plate 1c), temperatures adjacent to the coast in the northern portion of the model (i.e., above  $\sim 40^\circ$  N) have decreased as upwelling-favorable winds now approximately parallel the coastline throughout the domain (Figure 2c). Evidence of cold, offshore-flowing, upwelling filaments exists in the vicinity of Cape Blanco, Cape Mendocino, south of Point Sur, in the Southern California Bight, and below Point Eugenia. These filaments extend  $\sim 80$ - 200 km offshore and merge with the equatorward jet that meanders cyclonically and anticyclonically at speeds of  $\sim 30$ -50 cm/s with alongshore wavelengths of  $\sim 100$ -300 km. These findings are consistent with those from a recent process-oriented modeling study of the CCS, between  $35^\circ$  N- $47.5^\circ$  N, by Batteen (1997). An outstanding example of a mesoscale disturbance embedded within the CCS is illustrated by the cyclonic meander that forms off Point Eugenia in January (Plate 1a), intensifies in April (Plate 1b), and breaks away by July (Plate 1c) to propagate southwestward in the CC. Bernstein *et al.* (1977) noted similar mesoscale activity off Point Eugenia using data from CalCOFI surveys of the CCS taken from April to July, 1952. In the vicinity of the U.S.-Mexico border ( $\sim 32.5^\circ$  N) within the Southern California Bight, a division of flow is evident (Reid, 1963) in the equatorward jet

offshore as a portion of the jet turns cyclonically shoreward (Plate 1c). This division of flow is consistent with the summertime formation of the SCE (Lynn and Simpson, 1987).

By early fall (Plate 1d), as the upwelling system begins to weaken with the equatorward migration of the Subtropical High, the sharp nearshore temperature front present during summer north of Cape Blanco has become more diffuse. The coastal equatorward surface jet in this region is now oriented farther offshore and embedded streams of colder water flow southwestward into a cold-core eddy west of Cape Mendocino. South of Point Conception, the division of flow is more pronounced as a branch of the equatorward surface jet rotates cyclonically onshore and poleward while the main portion of the jet continues southward offshore. This flow structure within the Southern California Bight concurs with a seasonal maxima in the SCE from summer to early fall (Hickey, 1997). As in January (Plate 1a), in the vicinity of Point Eugenia, a cyclonic meander in the equatorward jet is discernible. In time (not shown), this meander intensifies, closes off, and propagates southwestward through the stream.

An examination of model upwelling along the Baja Peninsula in July (Plate 1c) and October (Plate 1d) reinforces conclusions drawn by Bakun and Nelson (1991) regarding the effects of cyclonic wind stress curl on upwelling in the vicinity of capes and coastal bights. Plate 1c shows that during summer, the most intense upwelling in the model occurs just south of Point Baja, off Point Eugenia, and extending westward from Cape San Lazaro. Conversely, Plate 1d shows that in fall, the largest areas of coldest water are located primarily in coastline indentations between these points. Bakun and

Nelson (1991) note that the mean equatorward alongshore wind stress in the CCS typically has an offshore maximum located ~200-300 km from the coast, which decays with distance either side of the maximum, such that cyclonic wind stress curl shoreward enhances coastal upwelling. During summer, when offshore winds are strongly equatorward across the CCS, alongshore variations in wind stress (offshore Ekman transport at the coast), combined with cyclonic wind stress curl (oceanic Ekman pumping), act to locally enhance upwelling adjacent to capes. In fall and winter, when equatorward winds weaken, cyclonic curl maxima are frequently located within coastal bights, as when winds around cyclonic storms are directed into coastal indentations, become compressed alongshore, and reach maximum velocities adjacent to the coastal boundary (Bakun and Nelson, 1991).

In the model, the coldest coastal water is present in the south and extends equatorward from Point Baja. Huyer (1983) notes that, although upwelling-favorable winds, and thus significant offshore Ekman transport, persist off southern Baja year-round, there is an absence of cold coastal water. Bakun and Nelson (1977) postulate that reduced cloud cover in this region leads to rapid surface heating which may diminish the effects of upwelling on sea surface temperatures. Further study using a coupled atmosphere/ocean model to better define the roles of air-ocean fluxes in this region is warranted.

Nearshore poleward flow occurs throughout the model domain at varying depths and intensities during different seasons. In January (Figure 15), poleward flow maintains

an undercurrent structure, underlying surface equatorward flow which generally increases in scope and magnitude southward. In the northern portion of the domain off the coast of Oregon (Figure 15a), the undercurrent lies primarily below ~200 m depth, increasing in velocity with depth to speeds of ~12.5 cm/s below ~500 m. Off northern California (Figure 15b), poleward flow has an undercurrent structure with speeds up to ~10 cm/s near the coast, and a relative maximum of ~2.5 cm/s extending westward to the surface. Just south of Point Conception, within the Southern California Bight (Figure 15c), weak poleward flow is present throughout the water column at the coast and attains an undercurrent structure with a maximum of ~7.5 cm/s seaward beneath the maximum surface equatorward flow. In the southern portion of the domain, below Point Eugenia (Figure 15d), the undercurrent core of ~5 cm/s lies between ~250-550 m depth. These results are consistent with direct current observations of the CUC (e.g., Reid, 1962; Wooster and Jones, 1970) which show the undercurrent core to be a narrow zone of higher speed water of ~20 km in width and spanning ~300 m adjacent to the continental slope. Likewise, Lynn and Simpson (1987) characterized the CUC at many locations during winter as being diminished in strength with a general deepening of the core poleward flow.

Conversely, by summer the CUC increases in strength, shoals, and in some locations merges with or becomes a poleward surface current (Lynn and Simpson, 1987). Cross-sections of meridional velocity taken in July of model year 3 (Figure 16) at the same locations as those shown in Figure 15 for January support the above conclusions.

Off the coast of Oregon (Figure 16a), poleward flow near the coast has more than doubled in magnitude to  $\sim 25$  cm/s and now extends to the surface. Similarly, off northern California (Figure 16b), the undercurrent has shoaled and become a narrow ribbon of high speed water of  $\sim 12.5$  cm/s near the coast. In the Southern California Bight, just south of Point Conception (Figure 16c), flow remains weakly poleward throughout the water column at the coast in association with the return limb of the SCE. Below Point Eugenia (Figure 16d), surface poleward flow is still present, but the undercurrent offshore is better defined, more intense, and shallower than its counterpart in January. Thus, model results qualitatively support both observational and physical descriptions of seasonal variations in depth, intensity, and extent of poleward flow within the CCS (Lynn and Simpson, 1987; Hickey, 1997).

Horizontal maps of upper layer mean kinetic energy (MKE) and eddy kinetic energy (EKE) for July are shown in Figures 17a and 17b respectively. Maps of MKE and EKE are indicative of mean and eddy energy source locations (Holland *et al.*, 1983). A comparison of Plate 1c with Figures 17a and 17b shows that high values of MKE and EKE are found both along the meandering axis of the equatorward coastal jet and offshore in the vicinity of westward propagating eddies. Maxima in MKE are seen wherever flow velocity increases. These regions occur along the coast where the equatorward surface jet meanders cyclonically and anticyclonically, on the eastern (western) side of anticyclonic (cyclonic) eddies due to the additive effect of the mean equatorward flow, and where flow enhancement takes place between cyclonic and

anticyclonic eddy pairs. Figures 17a and 17b show that, during the upwelling season, maxima in MKE and EKE occur in the same vicinity and values of MKE exceed those of EKE. This is consistent with the results of Batteen (1997), which also showed that the meridional variability of the winds and the beta-effect are important in generating realistic vertical and horizontal current structures, and baroclinic/barotropic instabilities in the mean equatorward current and poleward undercurrent, which result in the production of meanders, filaments, and eddies. Thus, regions of high model EKE values correspond to areas where eddies are likely to be generated, such as off Cape Blanco, offshore and downstream of Cape Mendocino and Point Arena, in the Southern California Bight, and in the coastal indentations on either side of Point Eugenia (Figure 17b).

Kelly *et al.* (1997) recently used both drifter and TOPEX/POSEIDON altimeter observations to investigate the variability of near-surface EKE in the CCS west of 124° W between 33° N-40.5° N. A qualitative and quantitative comparison of EKE results from the present study with their observations shows good correlation. Both Kelly *et al.* (1997) and model results (not shown) show maximum values of EKE in late summer to early fall between ~36° N-40° N and ~125° W, coincident with increased equatorward flow, and minimum values in spring. Specifically, maximum (minimum) EKE values observed by Kelly *et al.* (1997) within their study area were ~0.02 m<sup>2</sup>/s<sup>2</sup> (0.01 m<sup>2</sup>/s<sup>2</sup>) while maximum (minimum) values in the model were ~0.03 m<sup>2</sup>/s<sup>2</sup> (0.005 m<sup>2</sup>/s<sup>2</sup>). Additionally, both studies reveal a tendency of EKE maxima to propagate westward in time.

By the end of the quasi-equilibrium phase, it is satisfying to see that the model appears to respond favorably to both atmospheric and oceanic forcing. The successful reproduction of major features within the CCS, and their seasonal horizontal and vertical characteristics and energetics, shows good agreement with previous descriptive, field, and modeling studies as discussed, and should provide a useful investigation into specific questions concerning CCS variability.

## **B. MODEL SIMULATION APPLICATIONS**

An additional goal of this study is to utilize model results to discuss and characterize key issues and/or unknowns within the large-scale CCS. Specifically, the seasonal appearance of the DC, seasonal variability off the Baja Peninsula, and the meandering jet south of Cape Blanco are investigated. Is the DC the result of the CUC surfacing (Pavlova, 1966; Huyer and Smith, 1974) or due to the SCC successfully rounding Point Conception (Hickey, 1997)? What is the seasonal variability of large-scale and coastal currents off Baja? Finally, is the meandering jet that originates near Cape Blanco a continuous feature and what is the role of the jet in the large-scale CCS?



## 1. The Davidson Current

Poleward flow, both surface (countercurrents) and subsurface (undercurrents), on the eastern side of ocean basins has been a subject of extensive study over the past several decades. Here we focus on the flow regime off Central and Southern California in terms of the seasonal appearance of the DC. First, several previous studies concerning poleward flow in this region are highlighted.

Chelton (1984) used 23 years of hydrographic measurements to describe the seasonal geostrophic velocity off Point Sur and Point Conception. The nearshore surface flow was found to be equatorward from March to September and poleward from October to February at both locations. Off Point Sur, a poleward undercurrent along the continental slope, within 75-100 km of the coast, first appeared in June/July, remained through February, and was absent at depth from March to May. This poleward flow extended to the surface from October to February with a maximum poleward velocity occurring at the surface in December (~14 cm/s). Off Point Conception, Chelton (1984) noted that the poleward undercurrent was still located ~75-100 km from the coast but persisted year-round with velocity maxima in June (~6 cm/s) and December (~8 cm/s). Poleward flow extended to the surface from October to February as off Point Sur, but the maximum velocity remained subsurface throughout the year.

Lynn and Simpson (1987) refer to the seasonal change in direction of surface flow, from equatorward to poleward, that occurs within ~150 km of the coast during fall

and winter as the Inshore Countercurrent (IC) instead of the DC, considering that it may be a general rather than a regional phenomenon. According to Hickey (1979), this poleward flow also occurs along southern California and Baja and is sometimes continuous around Point Conception. It is discontinuous in space and time and may appear as the poleward expression of inshore cyclonic eddies (Lynn and Simpson, 1987). Lynn and Simpson (1987) further surmise that periods of maximum IC flow correspond in general to periods of maximum CUC flow and suggest that the appearance in fall and winter of the IC is associated with the shoaling of the CUC. They also conclude that a strong semiannual variation of both the IC and CUC in the Southern California Bight and regions north of Point Conception may be tied to the seasonal development of the SCE.

Hickey (1997) notes that south of Point Conception, a branch of the equatorward CC turns cyclonically shoreward then poleward. This flow is called the SCC if it rounds Point Conception, and the SCE during periods when it exists as a closed circulation within the Southern California Bight. Hickey (1997) points out that the SCC has a seasonal maxima in winter which coincides with the development of the DC north of Point Conception, but that evidence also exists which attributes the DC to a shoaling of the CUC in late fall (Pavlova, 1966; Huyer and Smith, 1974).

In addition to numerous descriptive and field studies, there have recently been significant modeling efforts surrounding the major features of the CCS, including the DC. Auad *et al.* (1991) used an 8-layer, wind-forced, quasi-geostrophic numerical model

which included bottom topography and a realistic coastline to simulate the main components of the CCS. The model successfully achieved inshore poleward flow in January which related favorably in time and location to the DC. Auad *et al.* (1991) concluded that bottom topography played a significant role in the mean geostrophic transport, and formation of the SCE, within the Southern California Bight.

Pares-Sierra and O'Brien (1989), used a 1½-layer, wind-driven, reduced gravity model to successfully reproduce an observed shoreward excursion of a portion of the southeastward CC at ~32° N. Pavlova (1966) suggested a division of flow in the shoreward branch such that a northward component feeds an inshore countercurrent and the SCE, while a southward component continues as part of the main equatorward CC (Hickey, 1979). Further, Pavlova (1966) postulated that the shoreward tendency in the flow is caused by both bottom topography as well as the prevailing coastal winds. The model of Pares-Sierra and O'Brien (1989) consistently reproduced this structure but did not include bottom topography. Hence, Pares-Sierra and O'Brien (1989) concluded that the likely cause of the split in equatorward flow is a minimum in tangential winds in the vicinity of 34° N due to the seaward extension of the coastline from within the Southern California Bight toward Point Conception. Additionally, Pares-Sierra *et al.* (1992) found that the 1½-layer PE model successfully simulated Geosat altimetric sea-level observations and that shoreward of a sea-level trough off the California coast, an increase in sea-level was indicative of the presence of a coastal countercurrent. Model results also showed maximum sea-level variability to be located in the waveguide adjacent to coastal

California. The most intense variability occurred between Monterey and Cape Mendocino and south of Point Conception. Both locations are areas of enhanced variability, and even reversals, in seasonal wind stress fields (Pares-Sierra *et al*, 1992). Thus, it seems logical that a single concrete description as to the cause or origin of the DC and/or poleward flow in this region has not surfaced. Rather, several theories exist and we examine in this study which one, if any, our model most closely resembles.

In the present study, the appearance of the DC in fall and winter is best simulated as a surfacing of the undercurrent nearshore, combined with poleward return flow, adjacent to the coast, around inshore cyclonic eddies of varying scales, which form a discontinuous chain along the entire coastline. Thus, the biggest drivers of this countercurrent may be the seasonal variations in wind stress and wind stress curl as well as variations in coastline geometry. Additionally, although not included in the model, bottom topography is believed to impact the variability of coastal circulation in the CCS and should be included in future modeling studies of this area.

The model successfully simulates many aspects of the nearshore flow field described by Chelton (1984) from observational data. Specifically, the model produces a seasonal change in surface flow alongshore off both Point Sur and Point Conception. In January of year 3, poleward flow at the coast extends throughout the upper water column at both locations (Figures 18a and 18b). In June, equatorward flow adjacent to the coast

is present at both locations with a weak poleward undercurrent at depth alongshore (Figures 18c and 18d).

Likewise, the model supports virtually all descriptions and conclusions drawn by Lynn and Simpson (1987). In particular, the model consistently shows discontinuous inshore poleward flow near the coast, both inside and outside the Southern California Bight, at various times throughout the year (not shown). In many cases, this flow is adjacent to strong equatorward flow throughout the upper water column offshore, supporting the presence of inshore cyclonic eddies. Off Southern California, this inshore poleward flow is sometimes continuous around Point Conception as illustrated for November of year 3 in Figures 19a (south of Point Conception), 19b (off Point Conception), and 19c (north of Point Conception), and described by Hickey (1979). Furthermore, the model develops the SCE at approximately the correct time and geographical location within the Southern California Bight which Lynn and Simpson (1987) link (along with the undercurrent surfacing) to the development of, or seasonal variation in, the IC (Plate 1d). The seasonal transition of the poleward undercurrent, from weak subsurface flow nearshore, toward strengthening and shoaling to surface poleward flow, is illustrated at 32° N in Figures 20a-20d. In August (Figure 20a), weak poleward flow is centered at ~250 m depth and underlies equatorward flow at the surface. In September (Figure 20b), the undercurrent core shallows to ~175 m depth and strengthens to ~2.5 cm/s. By October (Figure 20c), poleward flow extends to the surface with a core maximum of ~5 cm/s centered at ~40 m depth. Finally, in November (Figure 20d), a

strong countercurrent of  $\sim 12.5$  cm/s is present at the surface alongshore. The SCE appears in the model as one eddy in a discontinuous chain of cyclonic turning regions adjacent to the coast where major indentations immediately follow prominent bulges in the coastline. Such areas can be seen south of Cape Mendocino, in the vicinity of Point Sur, south and southeast of Point Conception, and between Point Baja and Point Eugenia, and are characterized by maximum equatorward flow offshore rapidly decreasing to minimum poleward or equatorward flow with decreasing distance toward shore (e.g., Plate 1a). Wherever and whenever these cyclonic flow regions interact with the shoaling undercurrent, poleward flow alongshore is enhanced, as off Point Sur in January (Plate 1a and Figure 18a).

The presence of a large anticyclonic meander in the surface equatorward jet consistently turns a portion of the flow shoreward in the vicinity of Point Conception (Plates 1a-1d). However, there is no appreciable evidence in the model to support the enhancement of a continuous countercurrent north of Point Conception, caused by a wrap-around of this divergent branch of the jet, to form the SCC and accompanying the seasonal formation of the DC as described by Hickey (1997). Rather, model results indicate that variations in wind stress induce flow instabilities which are enhanced by coastline perturbations. An inshore train of cyclonic eddies, combined with a poleward undercurrent of varying seasonal depths, forms a discontinuous countercurrent alongshore. Thus, as equatorward winds diminish in fall and winter, the CUC shoals and interacts with poleward return flow around these eddies. The net effect is additive,

producing the poleward surface flow observed nearshore at various locations throughout the CCS and known as the DC north of Point Conception.

## **2. Seasonal Variability Off Baja**

With the possible exception of northern Baja (which has been regularly sampled by CalCOFI and covers the region north of Point Baja to the U.S.-Mexico border), much of the peninsula's shelf remains a data sparse region and has an unknown seasonal cycle (Hickey, 1997). One of the objectives of this study is to utilize the model to better describe and define CCS structure and variability off the Baja Peninsula. Toward this end, we describe known circulation patterns in this region based on previous studies and then examine the model's ability or inability to reproduce observed flow features, as well as to contribute support as to their cause.

Huyer (1983) uses mean monthly SST maps (from Robinson, 1976), coupled with profiles of Ekman transport over the CCS, to show the correspondence of coldest water at the coast to regions of large offshore Ekman transport. Off Baja, these maps show that cold coastal water occurs off northern Baja in winter, along most of the peninsula in spring and summer, and again off northern Baja in early fall. Huyer (1983) points out that an exception exists off southern Baja where, despite year-round upwelling-favorable winds and offshore Ekman transport, there is an absence of cold water at the coast. Huyer (1983) offers two possibilities as to the cause of this phenomenon. First, low cloud cover south of Point Eugenia enhances surface heating in this region such that the effect of upwelling on SST is diminished (Bakun and Nelson, 1977). Huyer (1983) also

notes that more detailed maps (Lynn, 1967) reveal a thin band of colder water at the coast south of Point Eugenia from April through July. This timeframe corresponds to the period of most intense upwelling along Baja and may represent cold, upwelled water dominating the contrary effects of low cloud cover in the south. According to Nelson (1977), local upwelling-favorable winds are strongest in May when colder water at the coast exists where the coastline parallels northwesterly winds such as between San Diego and Point Baja and from Point Eugenia south to Cape San Lazaro. The second possibility offered by Huyer (1983) as to the lack of cold surface water adjacent to the southern Baja coast is that a strong poleward undercurrent, and associated downward-sloping isopycnals, overwhelms the tendency for upwelling in this region.

In the model, which does not include the effects of cloud cover, cold coastal water is present all along Baja California by year 3 (Plates 1a-1d) in agreement with the year-round upwelling-favorable winds (Figures 2a-2d). In January (Plate 1a), the coldest water extends equatorward from the large coastal bight south of Point Eugenia. In April (Plate 1b), the coldest water has expanded to northern Baja and offshore-flowing cold filaments are more evident. By July (Plate 1c), cold coastal water and filaments are more extensive and a well-defined temperature front is present alongshore south of Point Eugenia. October (Plate 1d) shows cold, upwelled water alongshore extending from southern Baja to Point Conception. While the model does produce discontinuous subsurface poleward flow off southern Baja, the results do not support the presence of a



persistently strong poleward undercurrent year-round below  $25^{\circ}$  N which mitigates upwelling tendencies in this region.

Lynn and Simpson (1987) describe the surface, near-surface, and subsurface flow and water mass characteristics off the Baja Peninsula based on analyses of 23 years of CalCOFI data. Surface equatorward flow, as described by Lynn and Simpson (1987), is strongest along the coast, showing significant seasonal variability, with maximum flow of  $\sim 20$  cm/s occurring in March and April. This inshore equatorward flow is present most of the year with no spring transition as observed north of the border. However, Lynn and Simpson (1987) note an exception south of Point Eugenia where a wintertime IC exists. In the model, the core of the surface equatorward jet remains offshore, seaward of weak poleward and weak equatorward flows adjacent to the coast which appear to be associated with inshore regions of cyclonic and anticyclonic activity (Plates 1a-1d). The model supports maximum equatorward current speeds of  $\sim 20$ - $30$  cm/s offshore during spring (Plate 1b), coincident with strongest equatorward wind speeds (Figure 2b). While the model does not show core equatorward surface flow nearshore along most of the peninsula, it does support strong seasonal variability in the equatorward surface jet offshore. In spring and summer (Plates 1b and 1c), the jet is strongest and closer to the coast while in fall and winter (Plates 1a and 1d) the jet weakens, meanders farther offshore, and is embedded in a more chaotic flow regime.

The near-surface watermass characteristics described by Lynn and Simpson (1987) include a subsurface low-salinity core at ~50-100 m depth (Reid *et al.*, 1958) close to the coast which indicates the path of the CC. This salinity minimum exhibits seasonal variations, spreads laterally toward the south with the equatorward CC, and may possess values as low as 33.7 as far as southern Baja (Lynn and Simpson, 1987). The model shows good qualitative agreement with the above description. In mid-July of model year 3, south of Point Eugenia, a core minimum of salinity of ~33.7 (Figure 21a) is present just below the surface and represents the location of a branch of the meandering equatorward surface jet which turns shoreward around an anticyclone (Figure 21b). Additionally, the salinity minimum in this region spreads laterally toward the south and shows significant seasonal variability in both position and magnitude (not shown).

The qualitative agreement between model results and previous descriptions of subsurface flow along the Baja Peninsula is encouraging. Relatively high salinities and temperatures distinguish Southern Water, which enters the CCS from the south with the poleward undercurrent (Hickey, 1997). Thus, as with the CC and its associated fresher water near the surface, vertical salinity distributions can be used to indicate the flow of the CUC, as saline subtropical water is transferred northward along the coast (Lynn and Simpson, 1987). According to Badan-Dangon *et al.* (1989), subsurface poleward flow exists off Baja most of the year and is primarily expressed as a series of cyclonic gyres along the coast. The undercurrent is particularly well-defined from late winter to early summer and adjoins the continental slope northward from the tip of Baja (Badan-Dangon

*et al.*, 1989). Lynn and Simpson (1987) estimate that, in general, maximum CUC velocities occur between ~200-300 m depth in summer and occasionally in winter and that high salinity values coincide with this maximum subsurface poleward flow. This is well-supported by the model. For example, off northern Baja, at 30.5° N, a closed salinity maximum of ~34.4 is centered at ~180 m depth in close proximity to the coast during mid-January of year 3 (Figure 22a). Likewise, a cross-section of mean meridional velocity in January shows a well-defined poleward undercurrent with speeds of ~7.5 cm/s below ~175 m depth at the same location (Figure 22b).

The region southeast of Point Eugenia, which represents the largest coastline perturbation along the Baja Peninsula, is the location of a seasonally intensifying cyclonic eddy such that return flow north of the eddy center transports warmer water hundreds of kilometers offshore between October and January (Lynn and Simpson, 1987). Although the model does not support the exact location of this eddy, it does uphold Point Eugenia and the region to the south as an area of strong seasonal variability as well as a generation region for cyclonic eddies. In January of year 3 (Plate 1a), an inshore branch of the equatorward surface jet with speeds as high as ~25 cm/s turns cyclonically away from the coast in the vicinity of Point Eugenia to rejoin the main stream offshore, indicating development of a cyclonic eddy. In April (Plate 1b), the cyclonic meander is better developed and has begun to detach from the vicinity of Point Eugenia. By July (Plate 1c), the meander has closed off to form a cold-core eddy which has propagated southwestward and is now centered at ~25° N, 118.5° W. A thin filament of colder water

extends south from Point Eugenia, transported by the high-speed inshore near-surface equatorward flow. Additionally, cyclonic turning is once again evident in the equatorward surface jet, but at a slightly different location from January, west-northwest of Point Eugenia. By October (Plate 1d), cyclonic turning to the west-northwest has further intensified and approaches the pattern shown for January (Plate 1a). Note that in January (Plate 1a), a cyclonic eddy centered at  $\sim 26^\circ$  N,  $123^\circ$  W has also formed and propagated westward in time from the same generation area. Thus, according to model results, Point Eugenia appears to play a significant role in cyclonic eddy generation and subsequent westward propagation. Although the position of the cyclonic meander, which indicates eddy production, varies to either side of the coastal point, model results clearly indicate a fairly well-correlated, seasonally-repeating pattern of eddy development at this location.

Although a data sparse region, the area off southern Baja is believed to be a highly dynamic environment for meanders, filaments, and eddies (Lynn and Simpson, 1987; Poulain and Niiler, 1989; Poulain, 1990; Niiler *et al.*, 1989). Model results from year 3 strongly support this description for the region south of Point Eugenia. Shoreward anticyclonic meanders in the equatorward surface jet (Plates 1a and 1b), sharp temperature fronts alongshore and offshore-flowing cold filaments (Plates 1c and 1d), combined with the flow field effects of cyclonic eddies detaching from Point Eugenia to propagate southwestward, all contribute toward a highly variable and complicated current structure in the model.

In reality, the pattern off southern Baja is perhaps no less complex. Strong seasonal variations in positions and intensities of atmospheric forcing mechanisms such as the Subtropical High and its interaction with the Trade Winds, the Mexican Low, and the Intertropical Convergence Zone, lead to robust seasonal changes in the oceanic flow field in this area. Consequently, the net flow pattern off southern Baja is the result of the seasonal strength of the CC and the position where it leaves the coast to feed the North Equatorial Current as well as the strength and position of the North Equatorial Countercurrent and the northwestward-flowing Costa Rica Coastal Current (Badan-Dangon *et al.*, 1989).

An example of near-surface and subsurface variability in the model for this area is illustrated through cross-sections of mean meridional velocity taken at 25° N, in the vicinity of Cape San Lazaro. In January (Figure 23a), equatorward flow persists near the surface with a maximum of ~25 cm/s nearshore and a second maximum of ~35 cm/s farther offshore. A poleward undercurrent structure is present within ~60 km of the coast with a maximum of ~10 cm/s below ~300 m depth. In April (Figure 23b), equatorward flow is still present nearshore but adjacent poleward flow offshore is now surface-intensified to ~25 cm/s and extends throughout the upper water column, indicating the presence of an anticyclonic eddy nearshore. Farther offshore, the equatorward jet has intensified to ~50 cm/s in response to the occurrence of maximum equatorward winds in spring. By July (Figure 23c), cyclonic turning is evident near the coast along with anticyclonic rotation offshore, as flow transitions seaward from poleward to equatorward

back to poleward throughout the water column. By October (Figure 23d), the nearshore cyclonic rotation has migrated slightly westward, giving way to a narrow band of surface-intensified equatorward flow of  $\sim 15$  cm/s alongshore. Plate 1d shows that this pattern is instrumental in advecting a thin, cold filament offshore in this region.

Model results off Point Baja also qualitatively support the conclusion by Lynn and Simpson (1987) that seasonal variations in watermass characteristics accompany variations in intensity of the CUC. For example, on day 834, which corresponds to mid-April of model year 3, a well-defined poleward undercurrent exists adjacent to the coast below  $\sim 100$  m depth with maximum speeds of  $\sim 7.5$  cm/s below  $\sim 300$  m depth (Figure 24a). A corresponding cross-section of salinity (Figure 24b) reveals a core maximum of  $\sim 34.4$  centered at  $\sim 185$  m depth which hugs the coast. During other seasons at this location, the undercurrent is less-developed or nonexistent and water at depth along the coast less saline (not shown).

### **3. The Meandering Jet South of Cape Blanco**

Satellite imagery (Strub *et al.*, 1991; Strub and James, 1995), field studies using Lagrangian drifter results (Barth *et al.*, 1994; Barth and Smith, 1996a,b), and recent numerical modeling efforts (Batteen, 1997) all suggest that the offshore separation of the equatorward coastal jet in the vicinity of Cape Blanco marks the start of a continuous meander along a temperature front that can be traced equatorward throughout the CCS during spring and summer. Results obtained in the present study for the large-scale CCS support the evidence cited above. Although small-scale eddies and meanders are known

to exist off Washington and northern Oregon (Ikeda and Emery, 1984) and are reproduced in the model (e.g., Plates 1a-1d show a cyclonic eddy centered at  $\sim 45^\circ$  N, which subsequently propagates offshore), it is not until Cape Blanco, where large-scale variations in coastline geometry begin to occur, that the equatorward jet significantly leaves the coast and undergoes a series of meanders downstream. By spring of model year 3 (Plate 1b), when the predominant wind direction transitions to equatorward across the entire CCS, maximum equatorward flow off the Oregon coast wanders southwestward in the vicinity of Cape Blanco and subsequently turns shoreward to meander anticyclonically near the coast off Cape Mendocino. The flow then undergoes alternating cyclonic (offshore) and anticyclonic (onshore) excursions, shedding westward propagating eddies which form along a temperature front near the coast, as it proceeds equatorward. By summer of model year 3 (Plate 1c), an upwelling front has formed inshore north of Cape Blanco and remains relatively uniform in association with only mild variations in coastline orientation. South of Cape Blanco the region of cold water near the coast gradually widens with distance equatorward as coastal water is pulled farther offshore with increased meander activity.

Previous modeling efforts have successfully reproduced meander activity using a uniform wind stress, a straight coastline, and no bottom topography (Batteen *et al.*, 1989; McCreary *et al.*, 1991). However, meanders and eddies approach realistic magnitude and variability when topographic features are included (Ikeda *et al.*, 1984; Haidvogel *et al.*, 1991), as well as when a realistic coastline, and spatially and temporally varying wind

forcing are incorporated (Batteen, 1997). Baroclinic and/or barotropic instability, wind, coastline irregularities, and topographic processes all appear to be important in generating the well-recorded meander activity off the North American west coast south of Cape Blanco.

While the model used in the present study successfully reproduced many realistic characteristics of the meandering jet, future research endeavors with this model will incorporate bottom topography in order to examine effects of the continental margin on the flow field, upwelling fronts, and MKE/EKE maxima locations. Additionally, the effects of major variations in terrain such as the Mendocino Ridge, the Monterey Submarine Canyon, and others will be explored.



#### IV. SUMMARY

This study was designed to investigate the combined role of wind forcing, temperature and salinity gradients, and coastline irregularities on the formation of currents, meanders, eddies, and filaments in the large-scale circulation of the California Current System. An additional goal of this research was to further characterize the formation of the Davidson Current, seasonal variability off the Baja Peninsula, and the meandering jet south of Cape Blanco. Toward these ends, a high-resolution, multi-level, PE model using a realistic North American coastline, was forced from rest with spatially and temporally varying winds, temperatures, and salinities. The migration pattern of the North Pacific Subtropical High, and its effects on the seasonal variability in alongshore winds, played a significant role in the generation, maintenance, and duration of observed current features throughout the model domain.

Due to the atmospheric pressure gradient, as well as alongshore temperature and salinity gradients built in using climatological forcing conditions, the model initially produced an onshore geostrophic flow in the interior ocean. By day 45 this flow turned poleward (equatorward) north (south) of the model midpoint ( $35^{\circ}$  N) at the coast, advecting warmer (colder) water poleward (equatorward) alongshore. In time, eddy development occurred at the coast as the mass field adjusted to seasonally varying forcing conditions. Initial instabilities which led to the production of anticyclonic (cyclonic) eddies in the northern (southern) portion of the model domain resulted from barotropic and baroclinic instability processes of varying scales.

By day 195, the equatorward jet moved north and overlaid a poleward undercurrent. Cold, dense water was present alongshore where the coast approximately paralleled the wind direction, indicating upward vertical motion of water adjacent to the coast due to offshore Ekman transport. By day 285, poleward flow alongshore showed significant trends of fluctuating depth and intensity.

Longer run times successfully illustrated the seasonal variability and complex structure of the CCS. By year 3, the equatorward surface flow was embedded with numerous eddies, meanders, and upwelling filaments consistent with real-world observations (Lynn and Simpson, 1987). These eddies and meanders, which propagated westward at Rossby wave speeds, induced large onshore and offshore transports in the equatorward surface jet. Springtime conditions in the model marked an increase in magnitude of the jet, consistent with Lynn and Simpson (1987). During summer, when upwelling-favorable winds paralleled the coastline throughout the domain, offshore-flowing cold filaments of realistic spatial scales (Batteen, 1997) existed in the vicinity of many coastline perturbations. By fall, the upwelling system weakened and within the Southern California Bight, a division of flow in the equatorward jet, first observed in summer, was more pronounced, consistent with a seasonal maxima in the SCE (Hickey, 1997).

The coldest water in the model was consistently located adjacent to the southern Baja coastline, coincident with persistent northwesterly winds in this area. In reality, this year-round cold coastal water is not observed (Huyer, 1983), with the effects of upwelling

on SST possibly diminished due to rapid surface heating resulting from reduced cloud cover (Bakun and Nelson, 1977). Further study using a coupled atmosphere/ocean model to delineate the roles of air-ocean fluxes in this area is recommended. Model results along Baja did however support conclusions by Bakun and Nelson (1977) regarding the effects on upwelling of cyclonic wind stress curl in that the most intense upwelling was located adjacent to capes during spring and summer, and within coastal bights during fall and winter.

Nearshore poleward flow occurred throughout the model domain at various depths and intensities during different seasons. These results support both observational and physical descriptions of seasonal variations in depth, intensity, and extent of poleward flow within the CCS (Lynn and Simpson, 1987; Hickey, 1997). Specifically, during winter, poleward flow primarily maintained an undercurrent structure with a deep core, whereas in summer this flow strengthened and shoaled in many locations.

Maps of MKE and EKE were used to indicate mean and eddy energy source locations (Holland *et al.*, 1983). Model results showed maxima in MKE and EKE during upwelling season wherever flow velocity increased, such as along the meandering axis of the equatorward coastal jet as well as in the vicinity of westward propagating eddies. EKE maxima tended to propagate westward in time, consistent with Kelly *et al.*, (1997), and disclosed eddy generation areas off Cape Blanco, offshore and downstream of Cape

Mendocino and Point Arena, in the Southern California Bight, and in the coastal indentations on either side of Point Eugenia.

The seasonal appearance of the DC was examined through comparison of model results with previous studies concerning the flow regime off central and southern California. The model supported the appearance of the DC as a surfacing of the undercurrent nearshore, combined with coastal poleward return flow around inshore cyclonic eddies of varying scales. Variations in wind stress induced flow instabilities which were enhanced by coastline perturbations. An inshore train of cyclonic eddies, combined with a poleward undercurrent of varying seasonal depths, formed a discontinuous countercurrent alongshore. Thus, it is hypothesized that as equatorward winds diminish in fall and winter, the CUC shoals (i.e., stretches vertically toward the surface) and interacts with poleward return flow around these eddies, producing a net poleward surface flow known as the DC north of Point Conception.

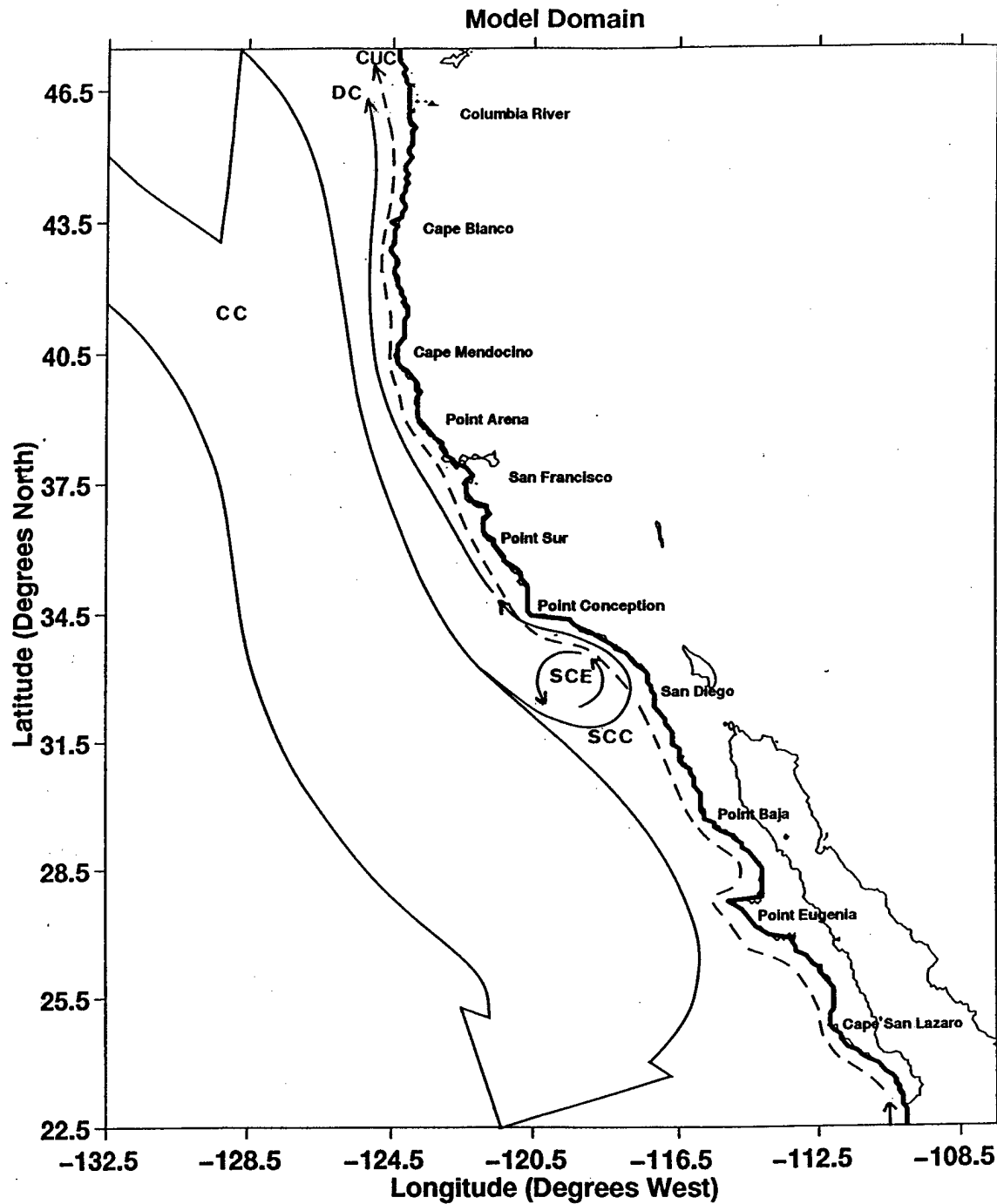
The model was also successful in reproducing many surface, near-surface, and subsurface flow characteristics off the Baja Peninsula described by Lynn and Simpson (1987). In spring and summer, the equatorward surface jet off Baja was strong and located closer to the coast. Conversely, during fall and winter, the jet weakened, meandered farther offshore, and was embedded in a more chaotic flow regime. Vertical salinity distributions off Baja successfully illustrated the fresher, near-surface flow of the equatorward jet offshore, as well as the influx of more saline Southern Water with the

poleward undercurrent near the coast. Model results also strongly supported the area surrounding Point Eugenia, which represents the largest coastline perturbation along the peninsula, as a persistent cyclonic eddy generation region. Likewise, the belief that strong seasonal variations in positions and intensities of atmospheric forcing mechanisms produce a complex and highly variable flow regime off southern Baja was well-supported by the model.

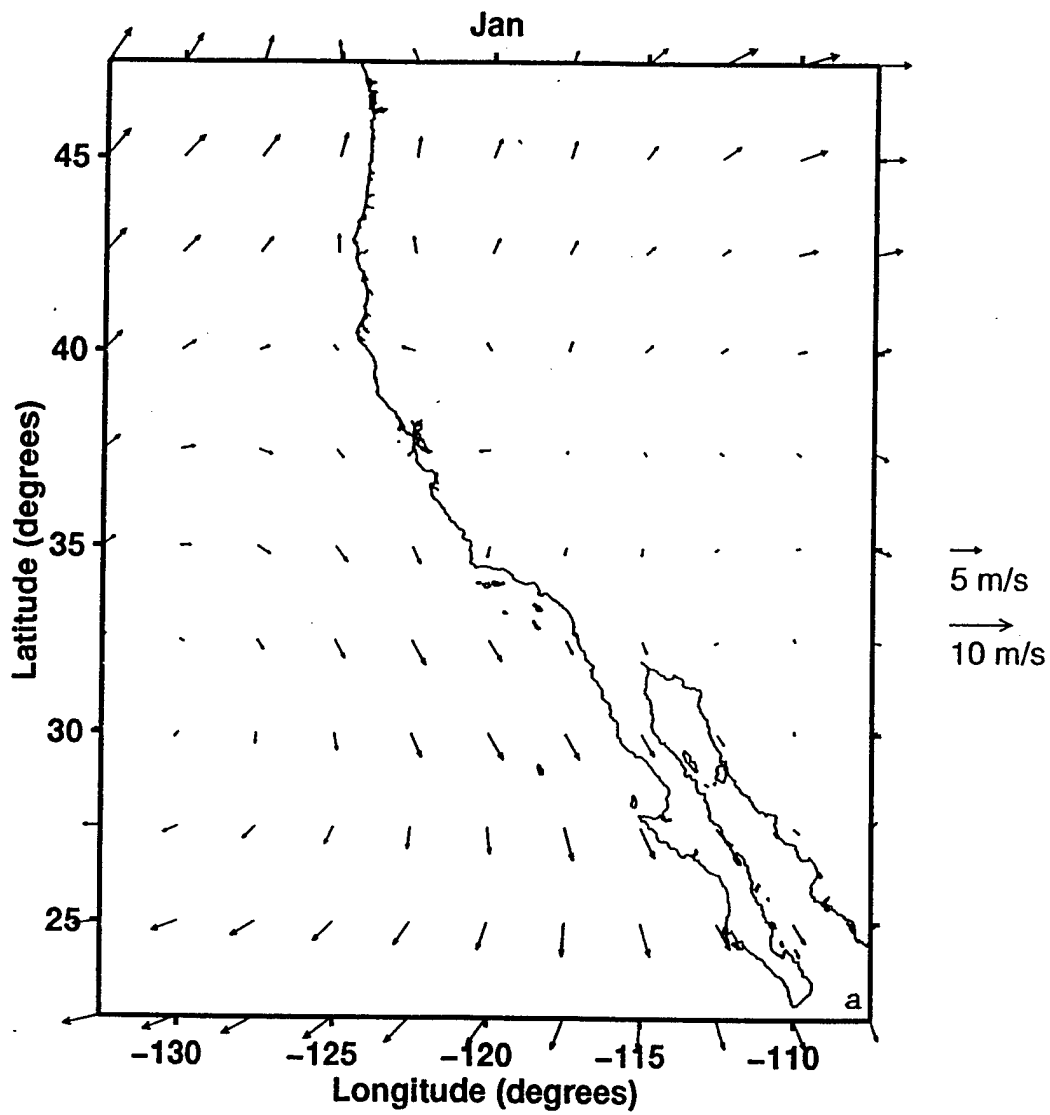
Finally, model results supported the equatorward jet as a relatively continuous feature which marks a division between cold, upwelled, coastally-influenced water and water of offshore origin. The jet remained within close proximity of the coast north of Cape Blanco, equatorward of which it underwent a series of cyclonic and anticyclonic excursions as coastline perturbations became more pronounced. As it proceeded equatorward, meander activity increased and the region of coastally-influenced water widened. Mixing of coastal and offshore waters took place through offshore-flowing cold filaments and westward-propagating eddies.

Results from this model simulation showed that the inclusion of a realistic coastline, spatially and temporally varying wind forcing, and temperature and salinity gradients led to both barotropic and baroclinic instability processes, generating observed current structures within the model CCS. In addition, bottom topography along the continental margin is believed to play an important role in the stability of the water column and the complex variability off the North American west coast. The addition of

bottom topography, the use of finer resolution spatial and temporal wind forcing, as well as atmospheric model coupling will lead to future modeling improvements and a better understanding of this highly complex regime.

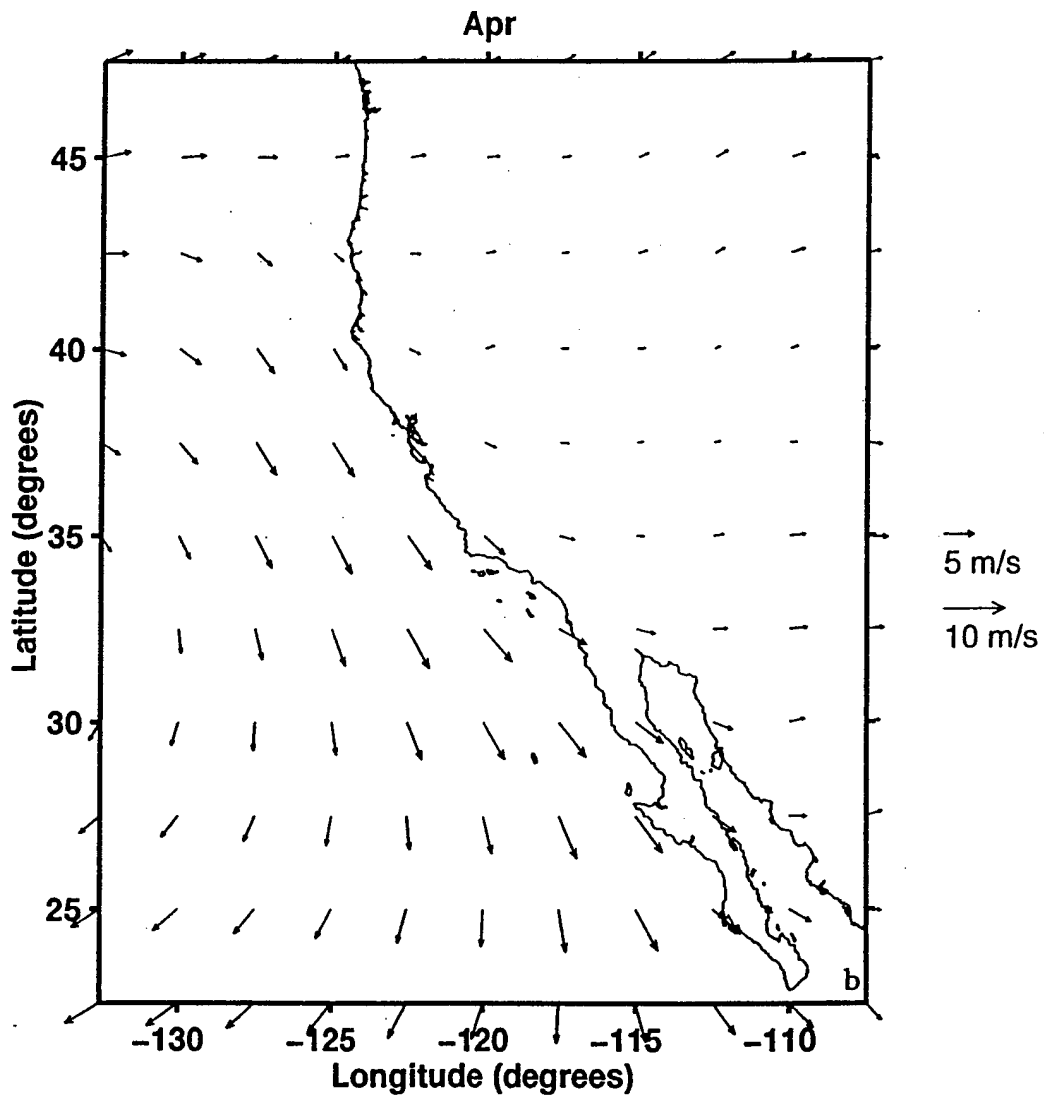


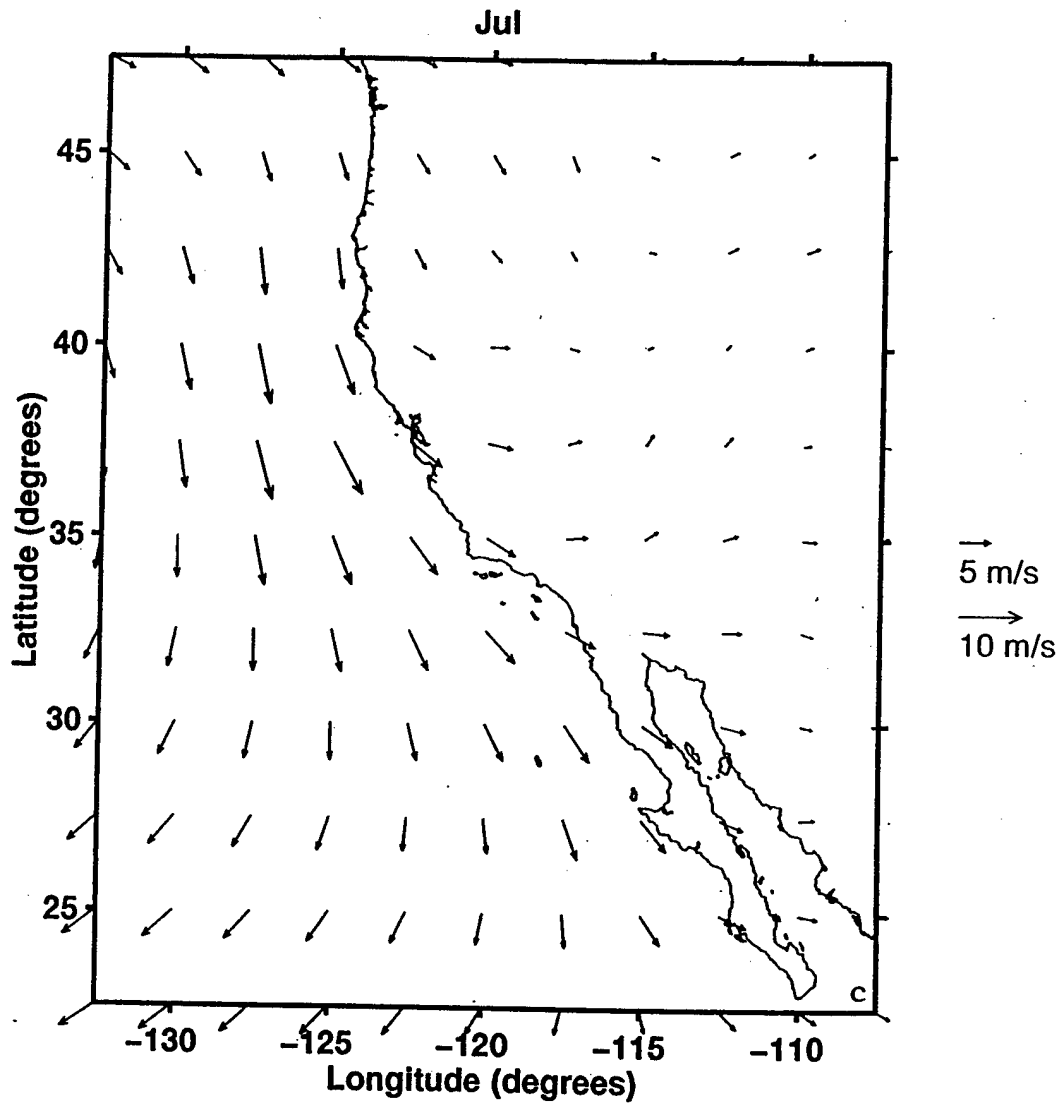
**Figure 1.** Model domain, coastline, and generalized classical circulation of the California Current System (CCS). The domain is bounded by 22.5° N to 47.5° N, 107.5° W to 132.5° W. The broad, slow surface equatorward California Current (CC) overlies the narrow, poleward California Undercurrent (CUC). Surface poleward flows include the Davidson Current (DC) north of Point Conception, and the Southern California Eddy (SCE) and Southern California Countercurrent (SCC) south of Point Conception.

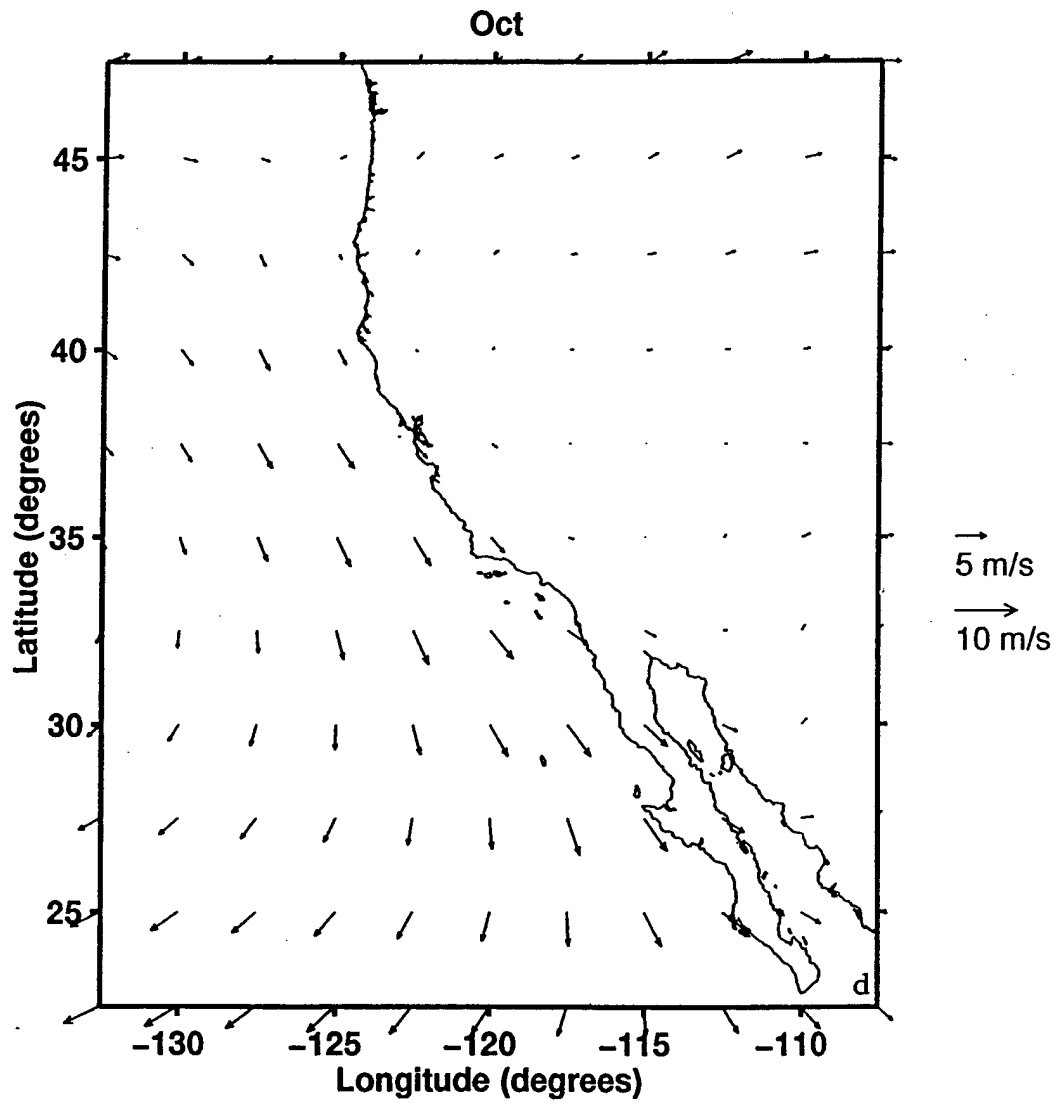


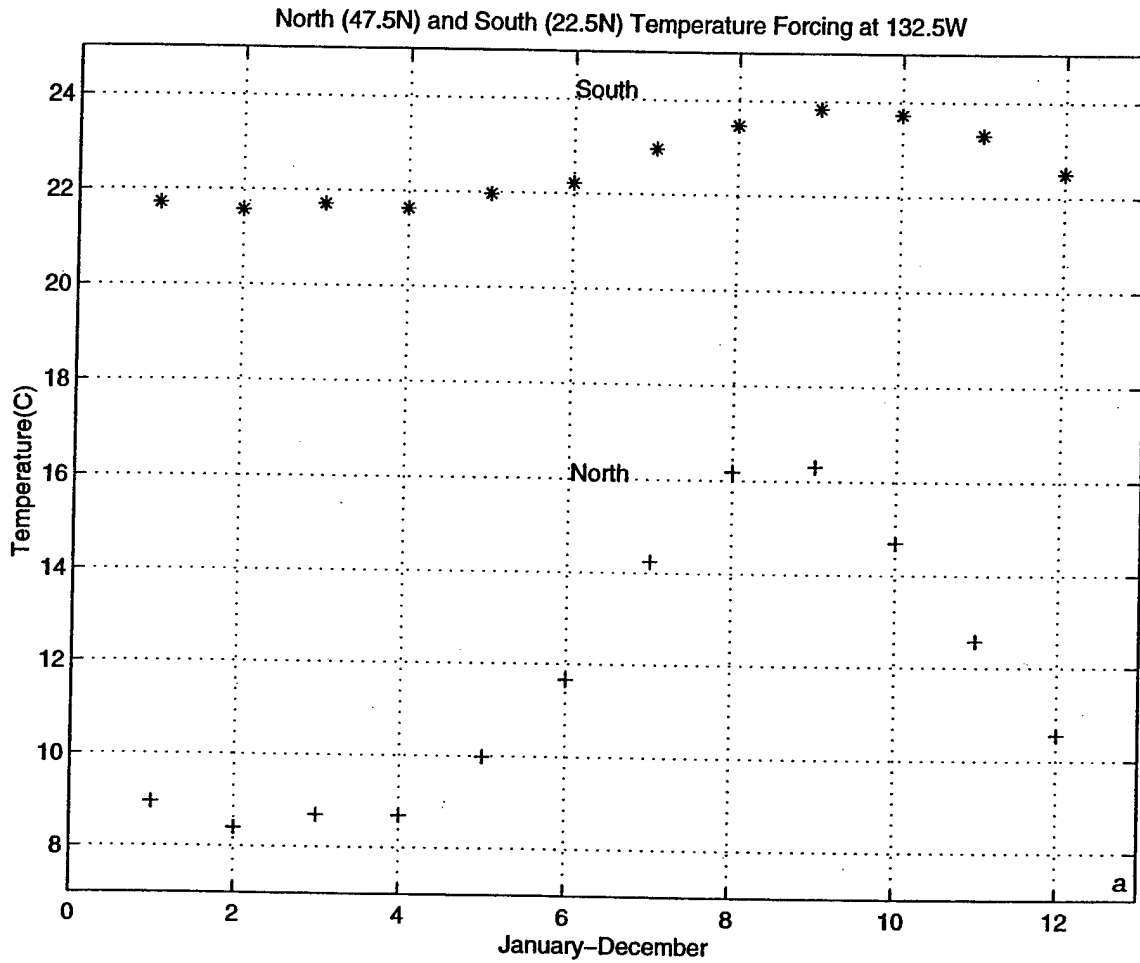
**Figure 2.** Climatological winds over the California Current System used to force the model. The climatological (1980-1989) ECMWF winds are shown here for (a) January, (b) April, (c) July, and (d) October





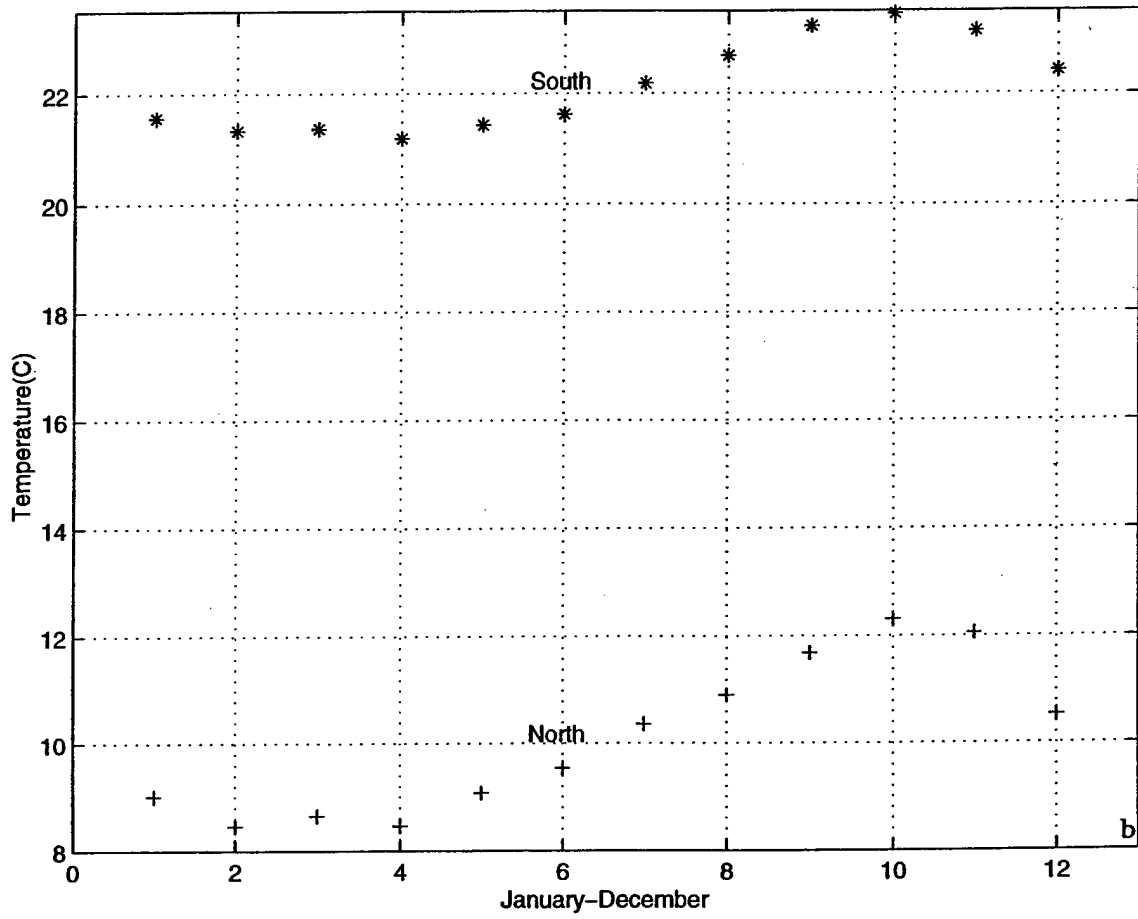






**Figure 3.** Time series plots of monthly temperature fields used as seasonal forcing in the basic simulation. The '\*' symbol represents data at 22.5° N, 132.5° W, while the '+' symbol represents data at 47.5° N, 132.5° W for levels (a) 13 m and (b) 46 m.

North (47.5N) and South (22.5N) Temperature Forcing at 132.5W



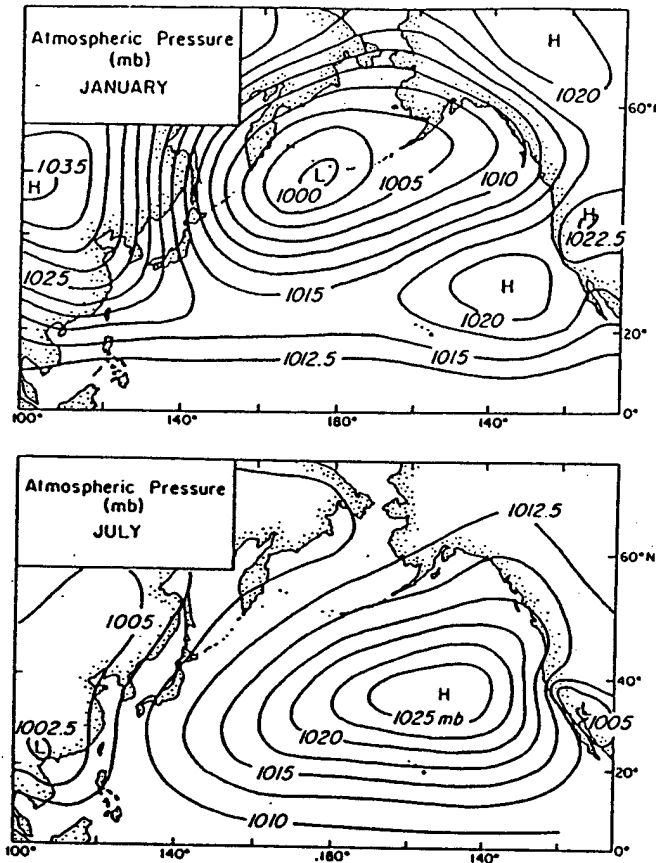


**Figure 4.** Long-term mean atmospheric sea level pressure for January and July over the north Pacific and western North America (From Huyer, 1983).

DEPTH : 13m  
T (DAY) : 3

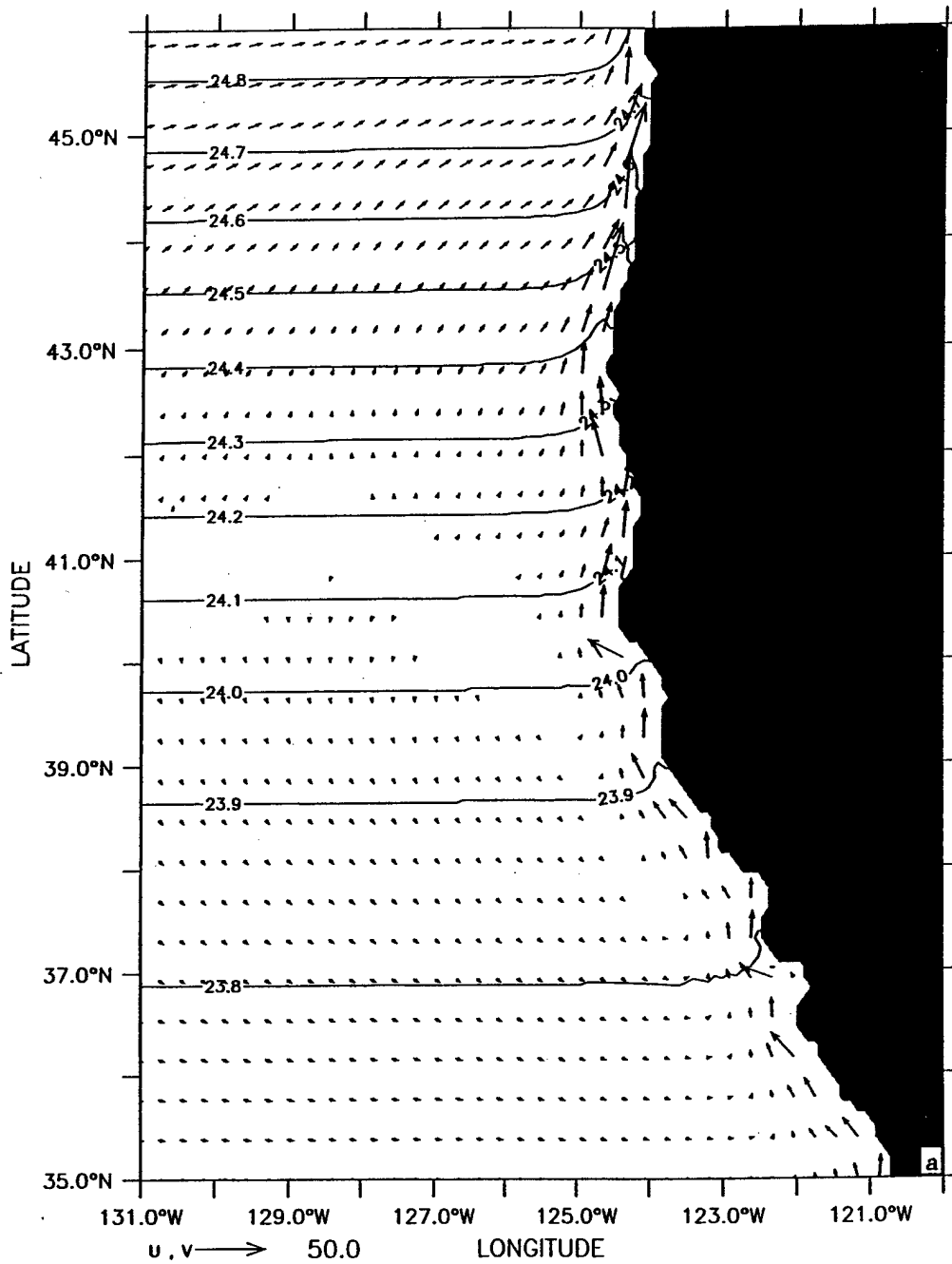
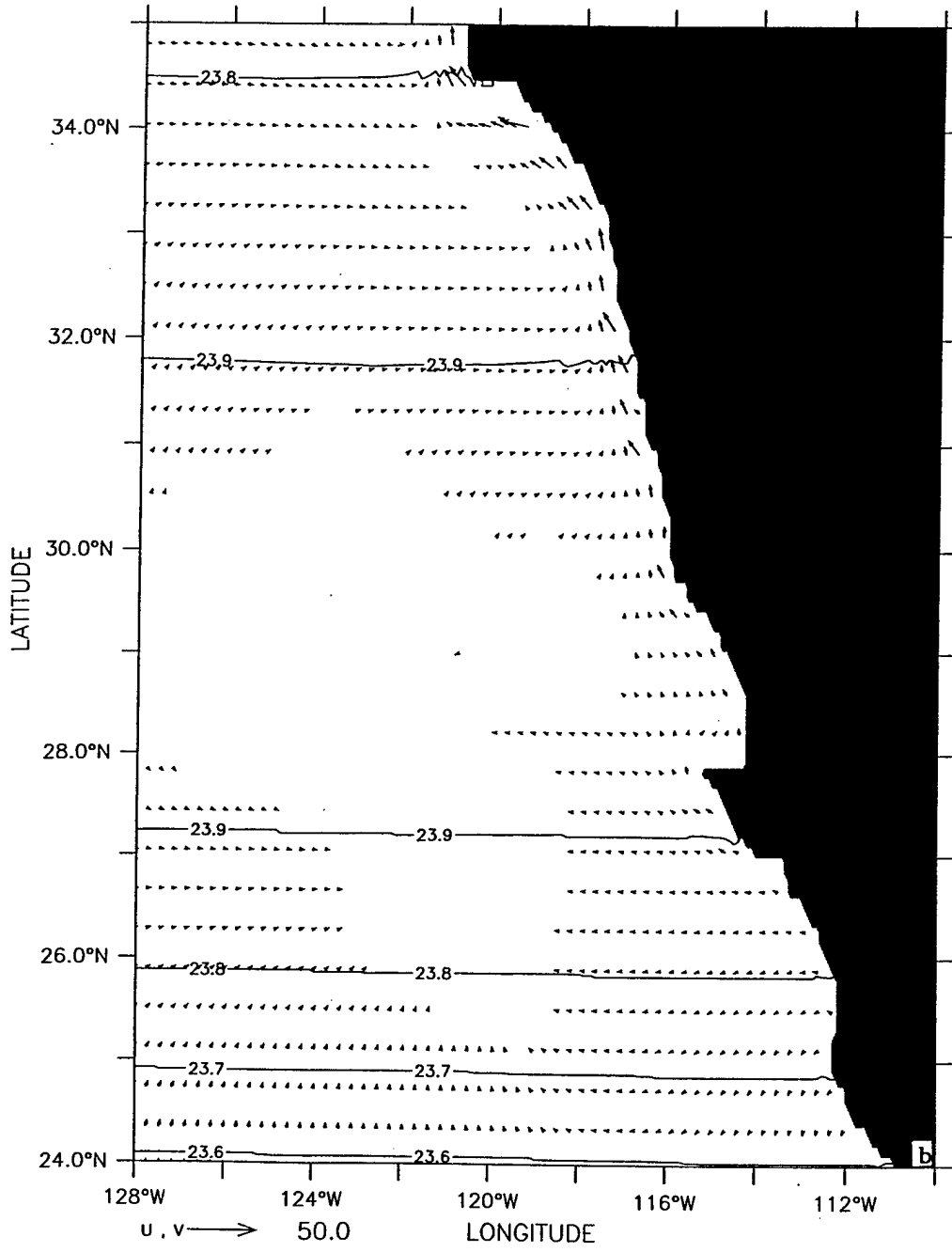


**Figure 5.** Day 3 density contours and velocity vectors at 13 m depth for (a) the northern half and (b) the southern half of the model domain. Contour interval is  $0.1 \text{ g/cm}^3$ ; maximum velocity vector is 50 cm/s. In this and the following figures, to avoid clutter, vectors are plotted at every third or fourth grid point in the cross-shore and alongshore directions, and velocities less than 5 cm/s are not plotted.

DEPTH : 13m  
T (DAY) : 3





DEPTH : 13m  
T (DAY) : 15

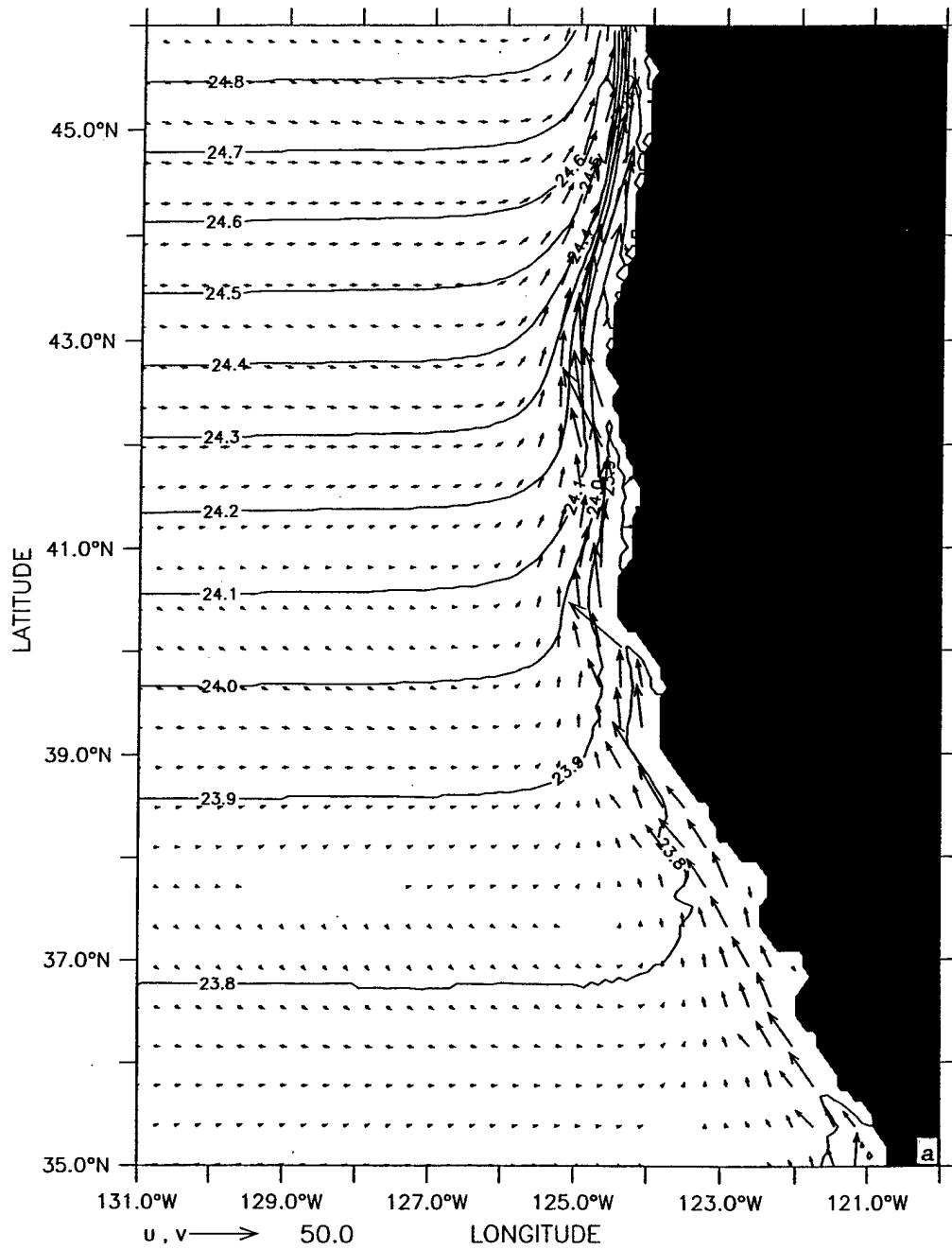
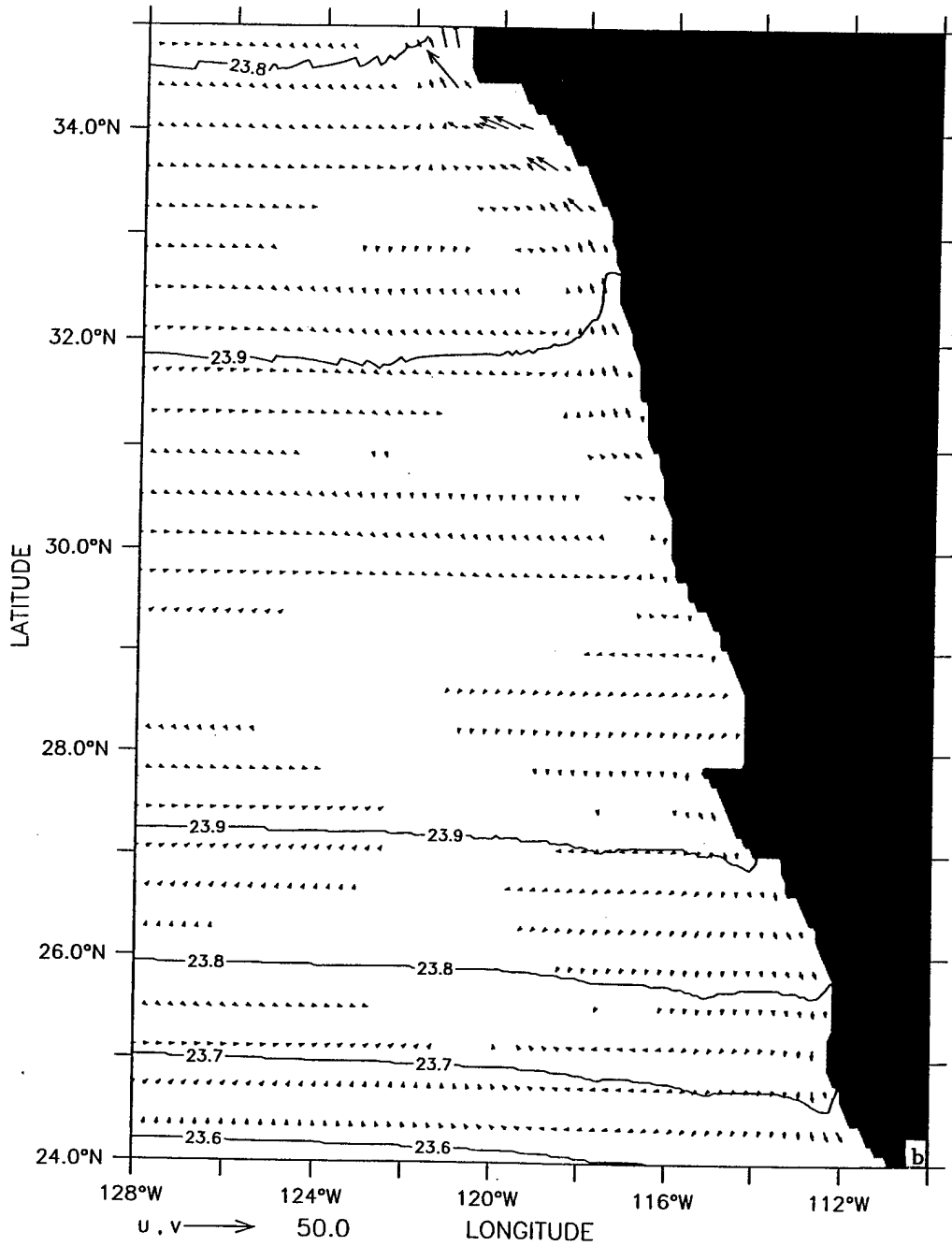


**Figure 6.** Day 15 density contours and velocity vectors at 13 m depth for (a) the northern half and (b) the southern half of the model domain. Contour interval is  $0.1 \text{ g/cm}^3$ ; maximum velocity vector is 50 cm/s.

DEPTH : 13m  
T (DAY) : 15



DEPTH : 13m  
T (DAY) : 45

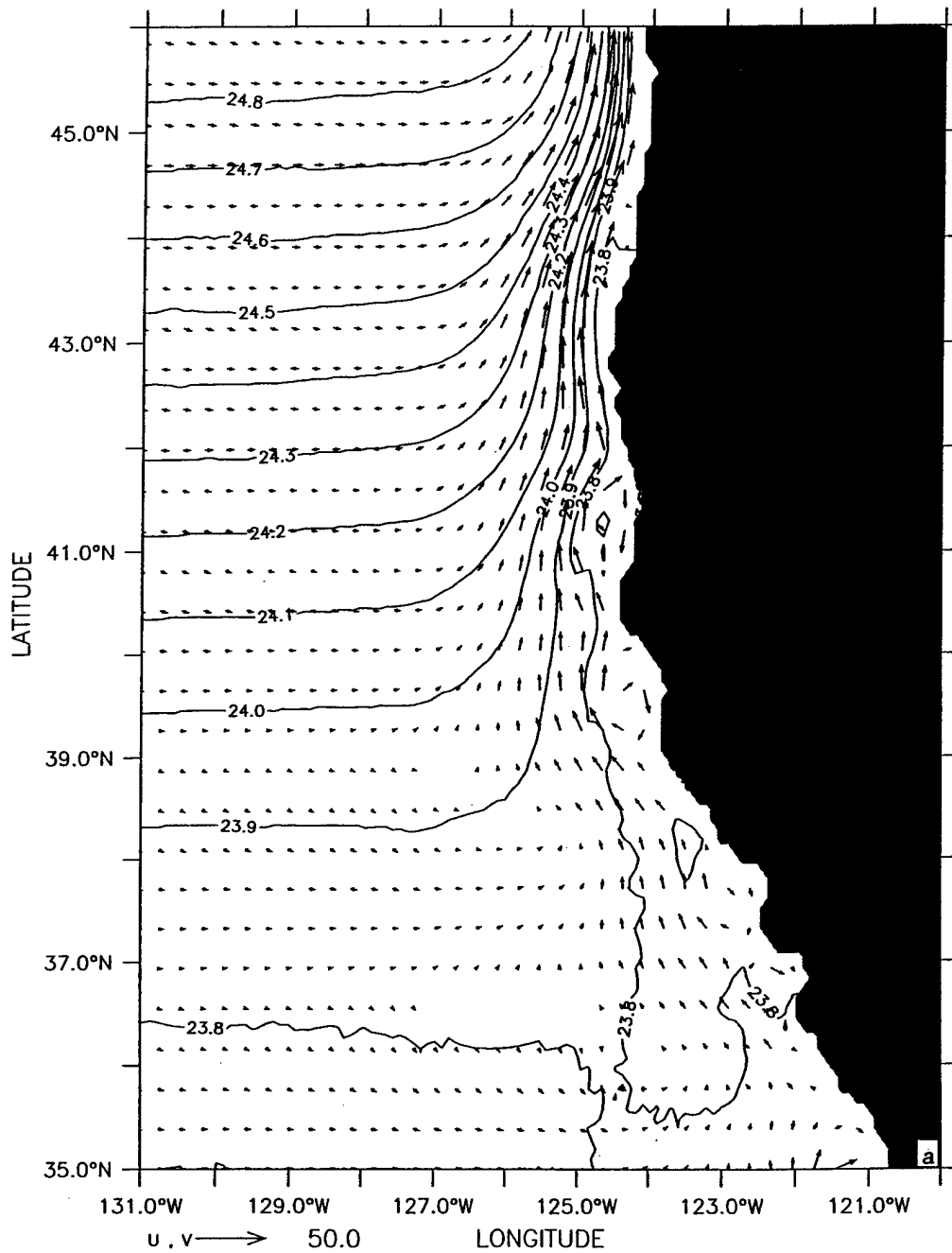
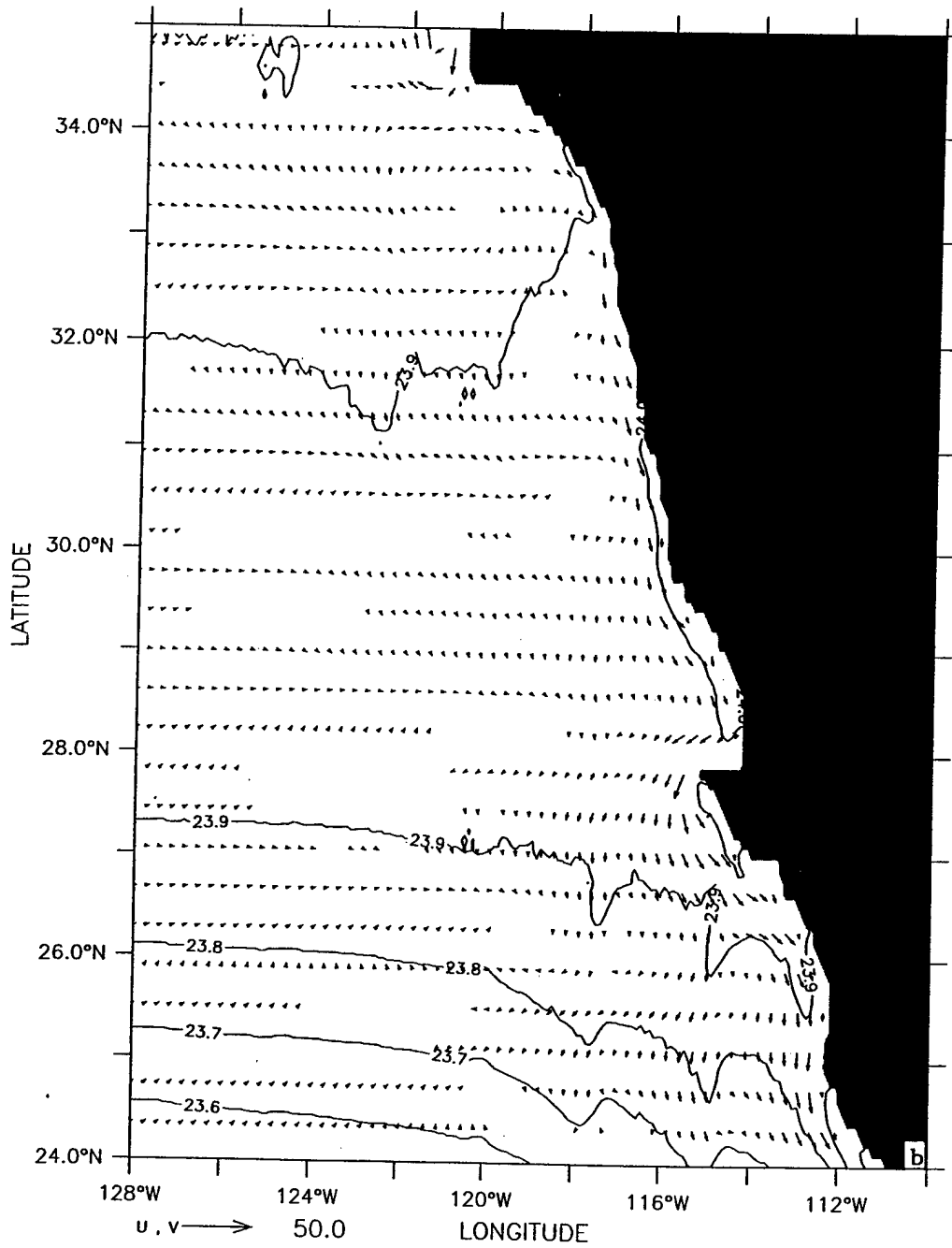


**Figure 7.** Day 45 density contours and velocity vectors at 13 m depth for (a) the northern half and (b) the southern half of the model domain. Contour interval is  $0.1 \text{ g/cm}^3$ ; maximum velocity vector is 50 cm/s.

DEPTH : 13m  
T (DAY) : 45



LATITUDE : 40.5N  
T (DAY) : 45

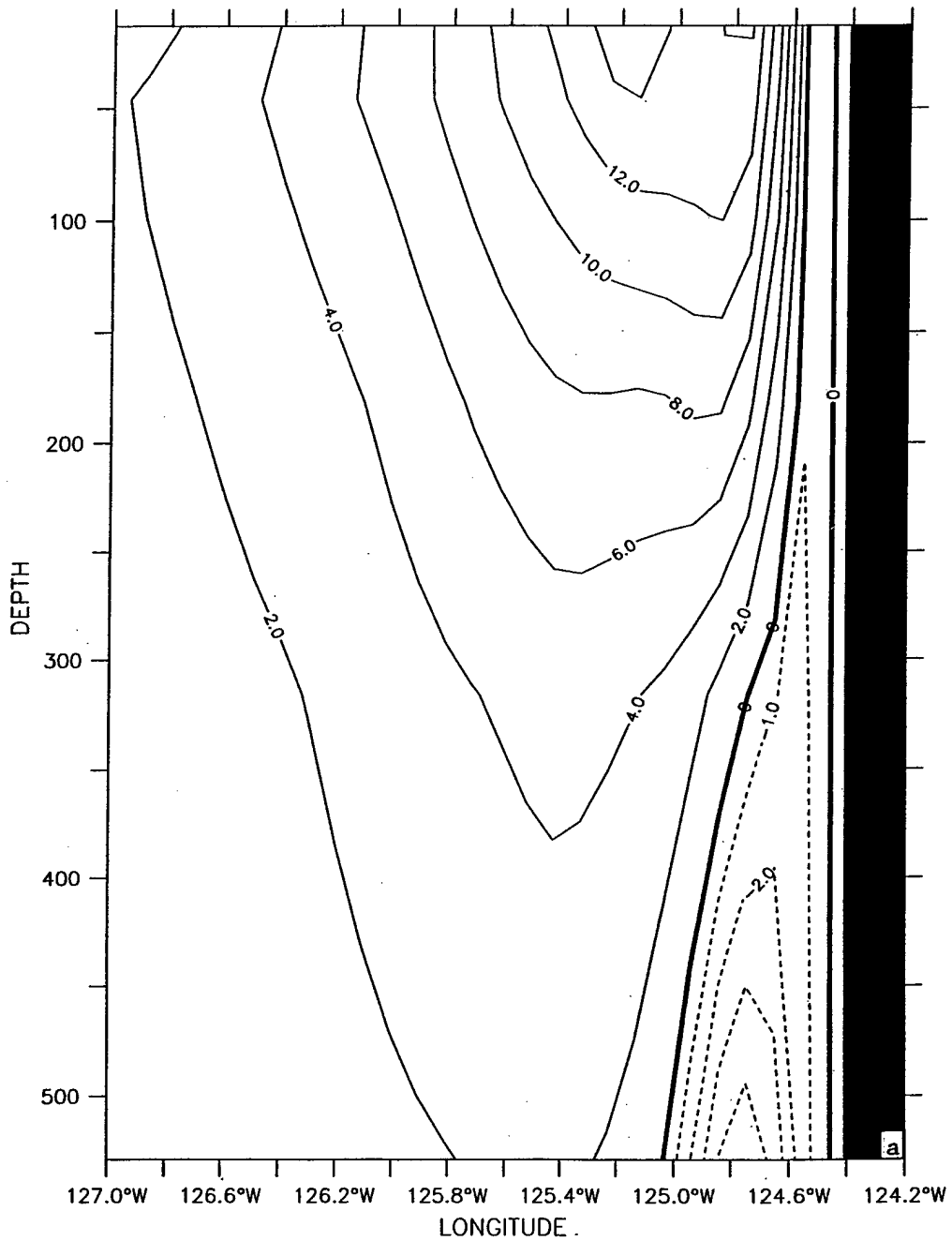
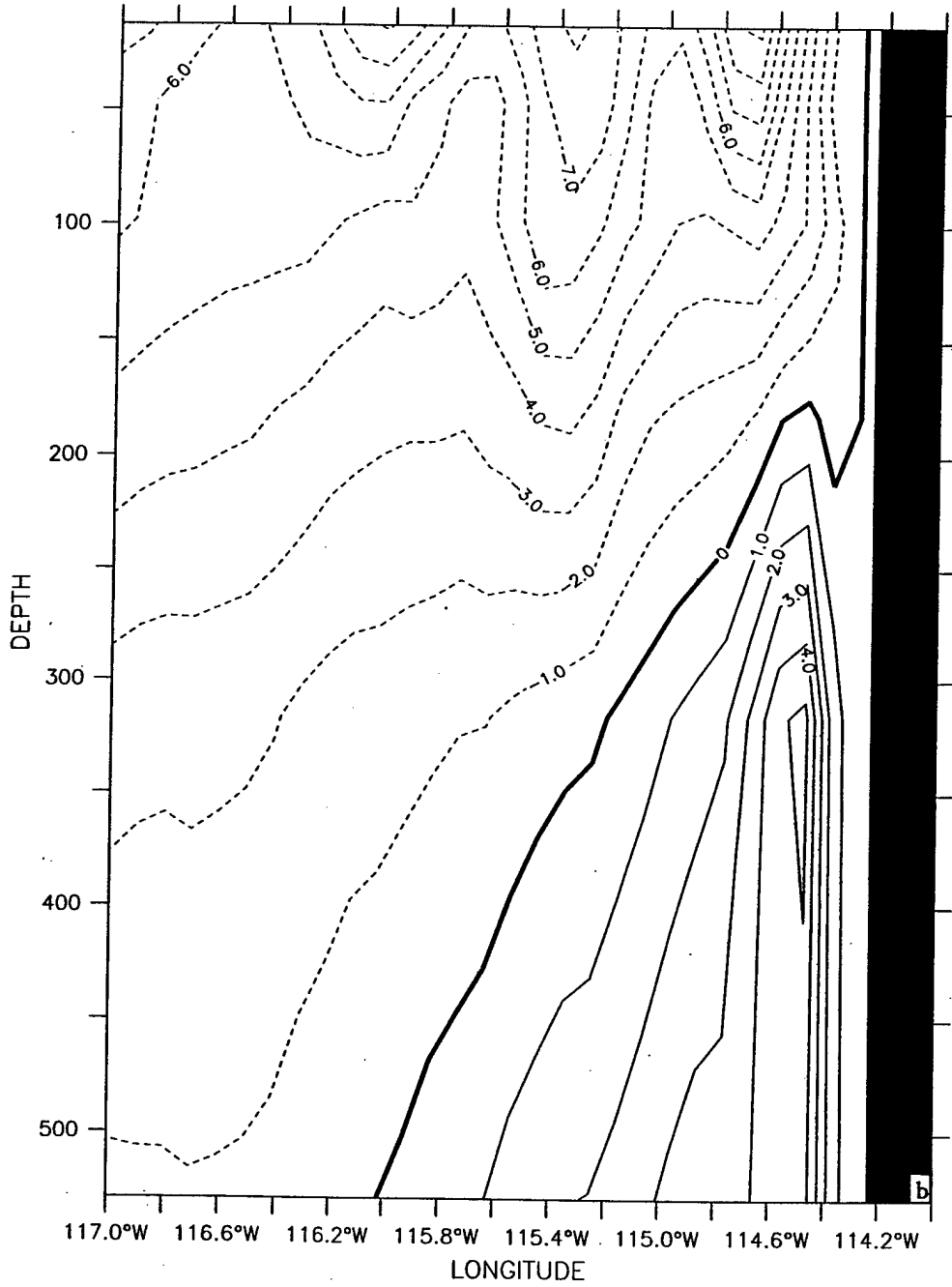


**Figure 8.** Cross-shore sections of meridional velocity ( $v$ ) at (a)  $40.5^\circ$  N (off Cape Mendocino) on day 45, and (b)  $28.5^\circ$  N (north of Point Eugenia) on day 105. Contour interval is 2 cm/s in (a) and 1 cm/s in (b).

LATITUDE : 28.5N  
T (DAY) : 105



DEPTH : 13m  
T (DAY) : 105

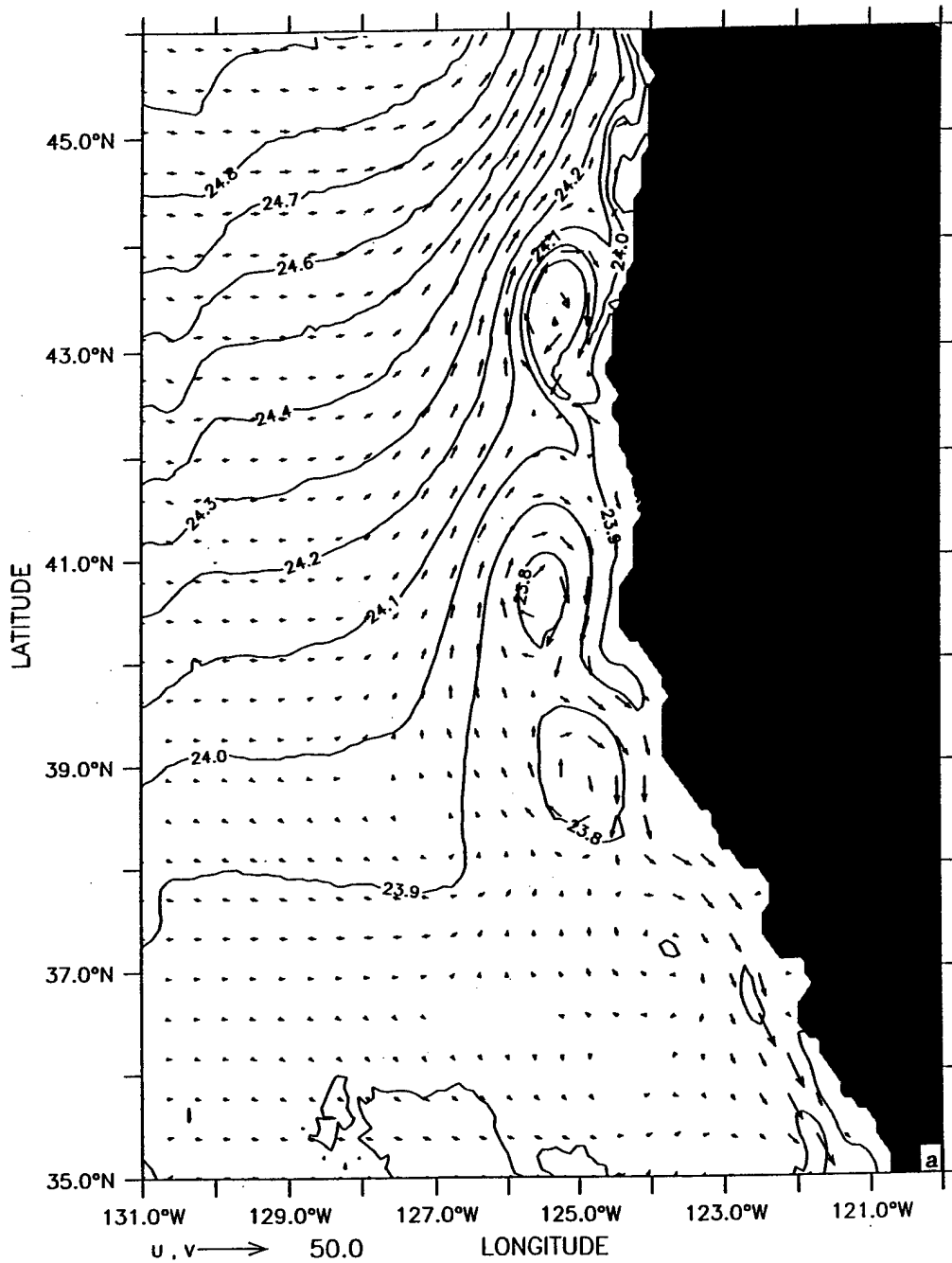
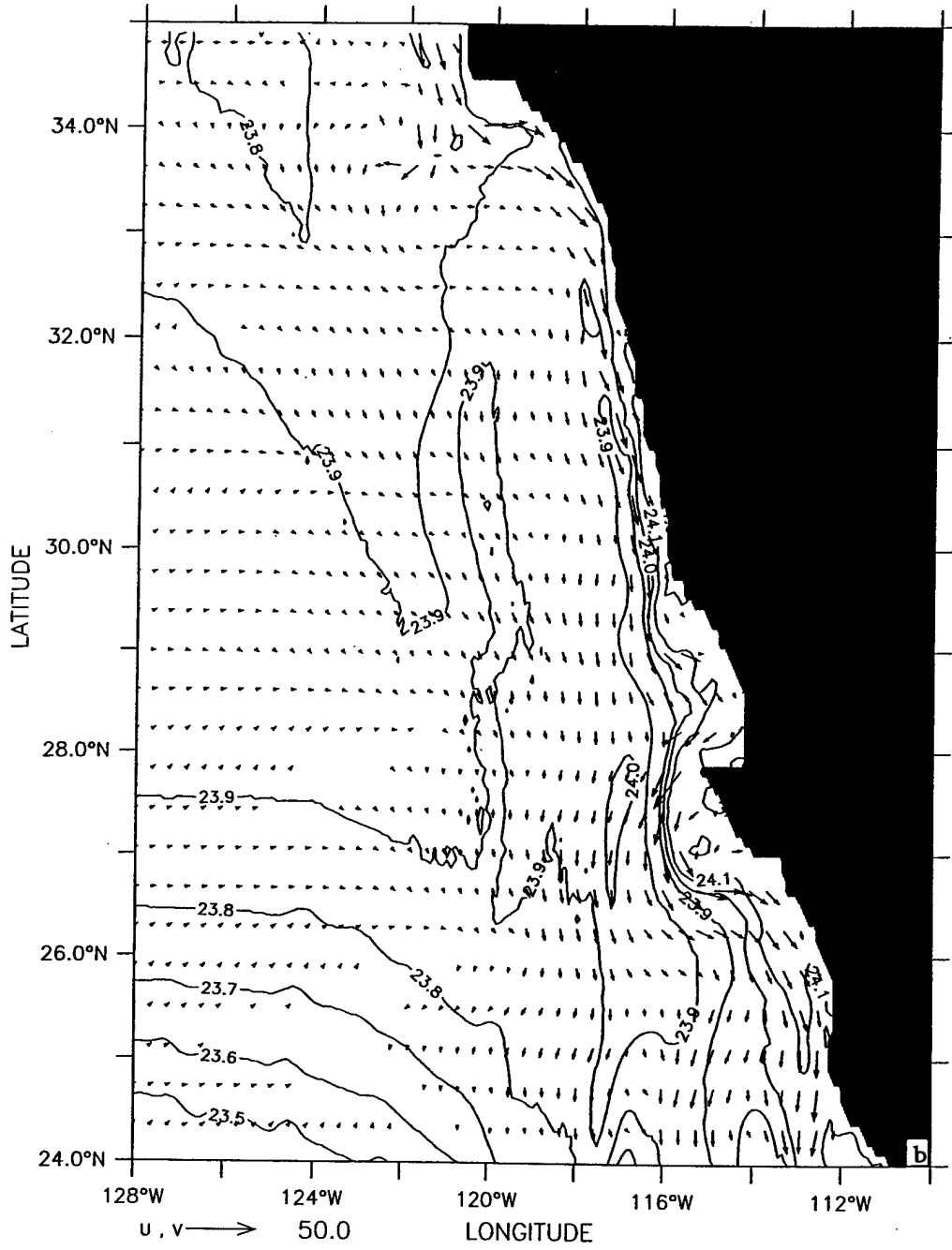


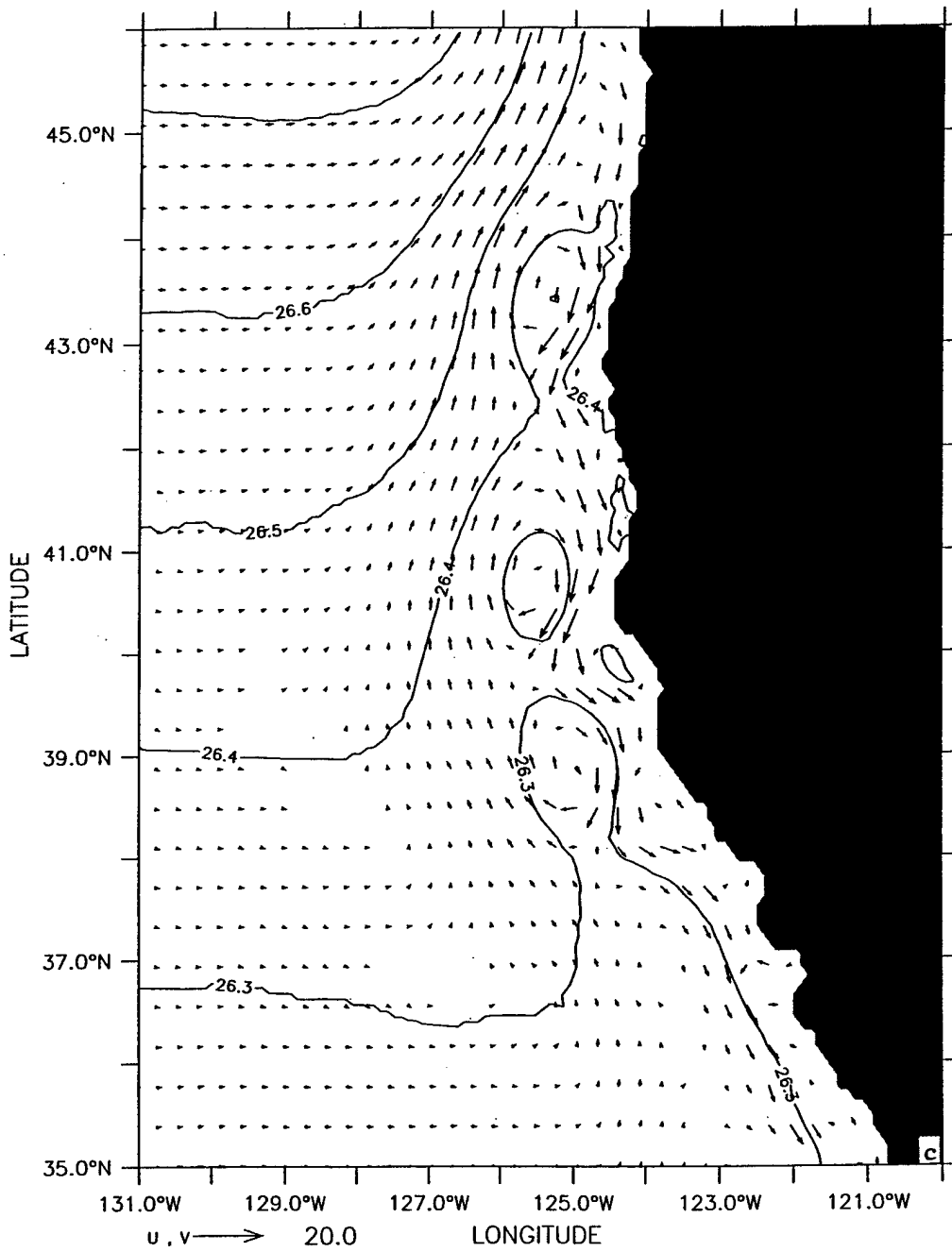
**Figure 9.** Day 105 density contours and velocity vectors for the northern (a,c) and southern (b,d) portions of the model domain at depths 13 m (a,b) and 316 m (c,d). Contour interval is 0.1 g/cm<sup>3</sup>; maximum velocity vector is 50 cm/s in (a) and (b), and 20 cm/s in (c) and (d).

DEPTH : 13m  
T (DAY) : 105

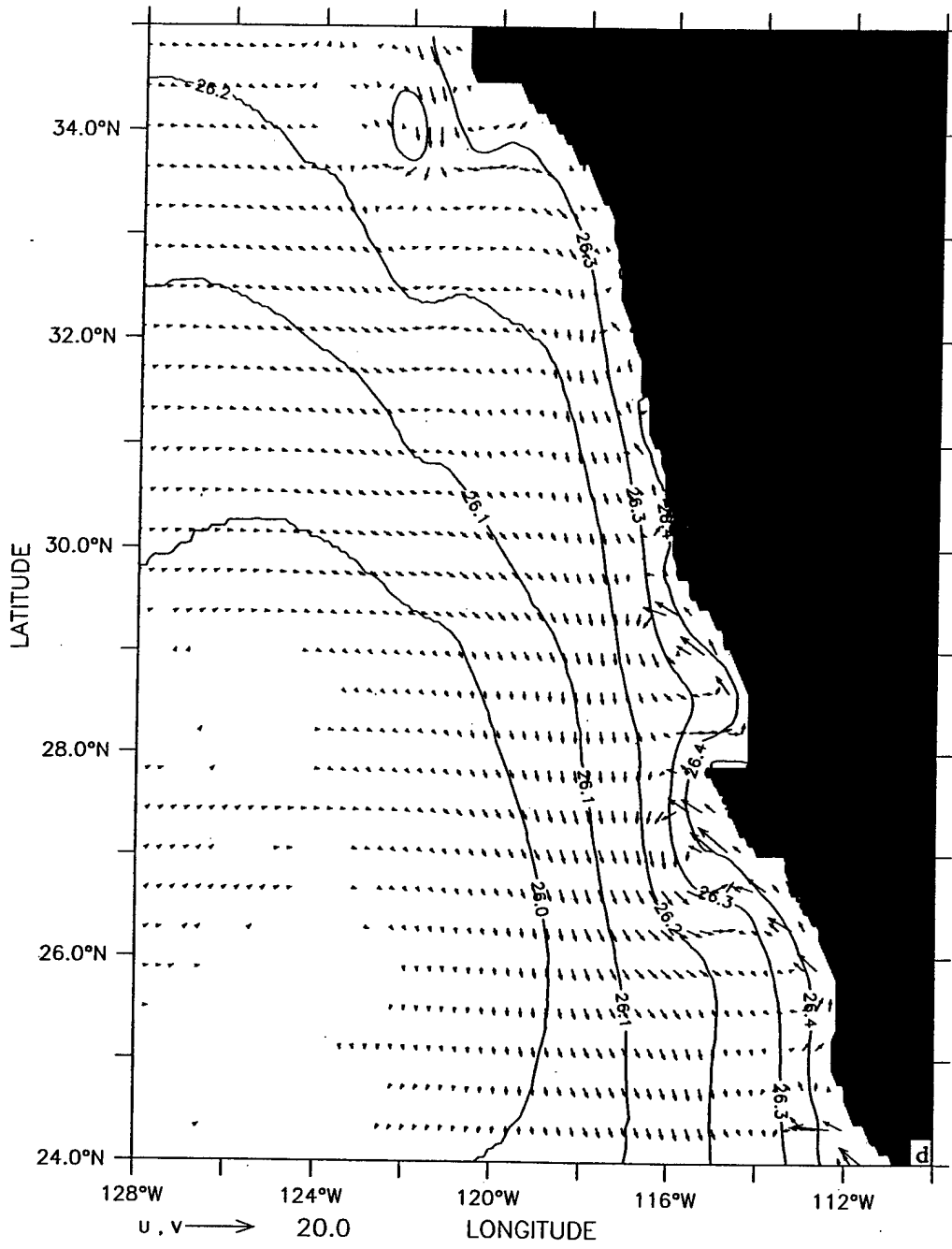




DEPTH : 316m  
T (DAY) : 105



DEPTH : 316m  
T (DAY) : 105



DEPTH : 13m  
T (DAY) : 195

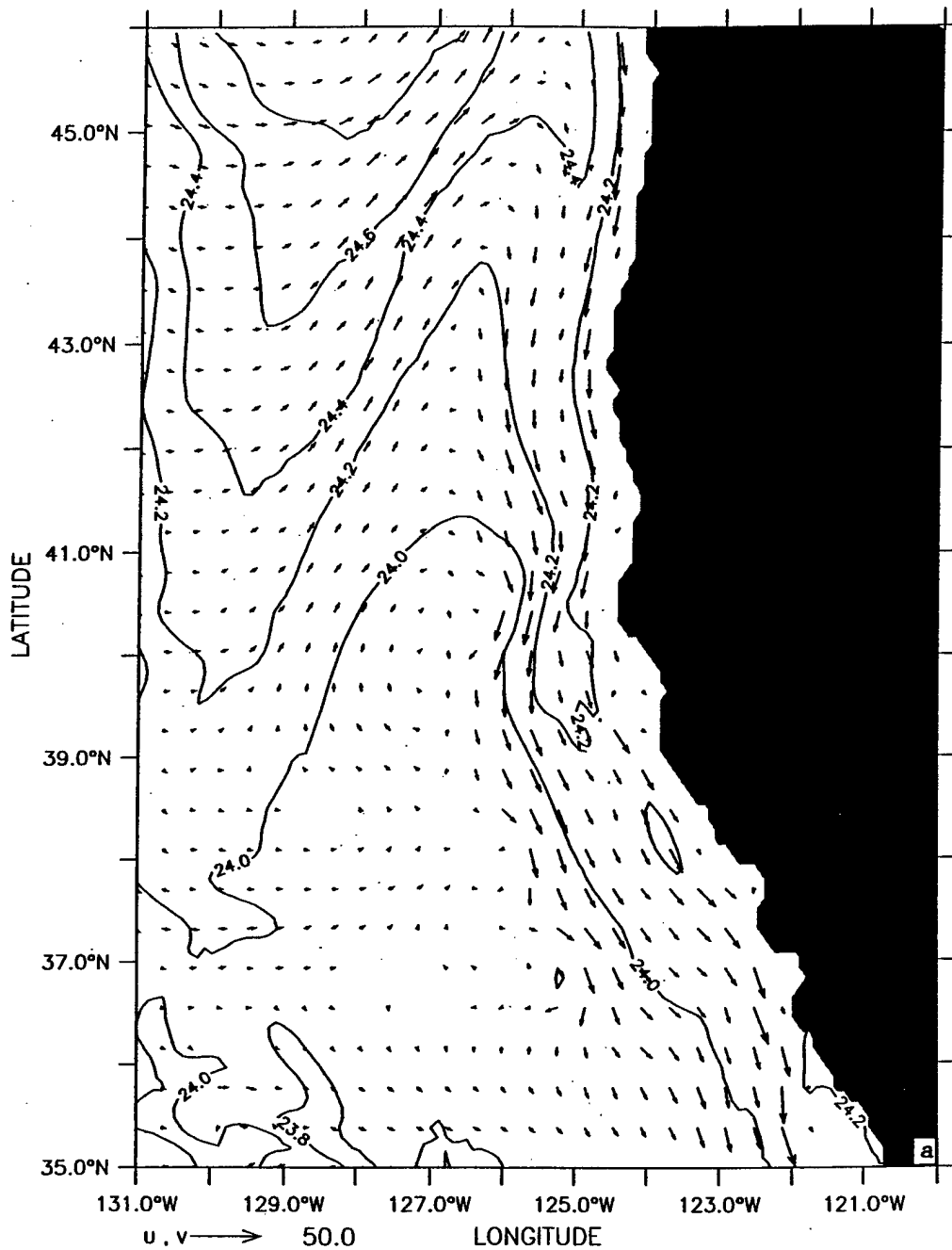
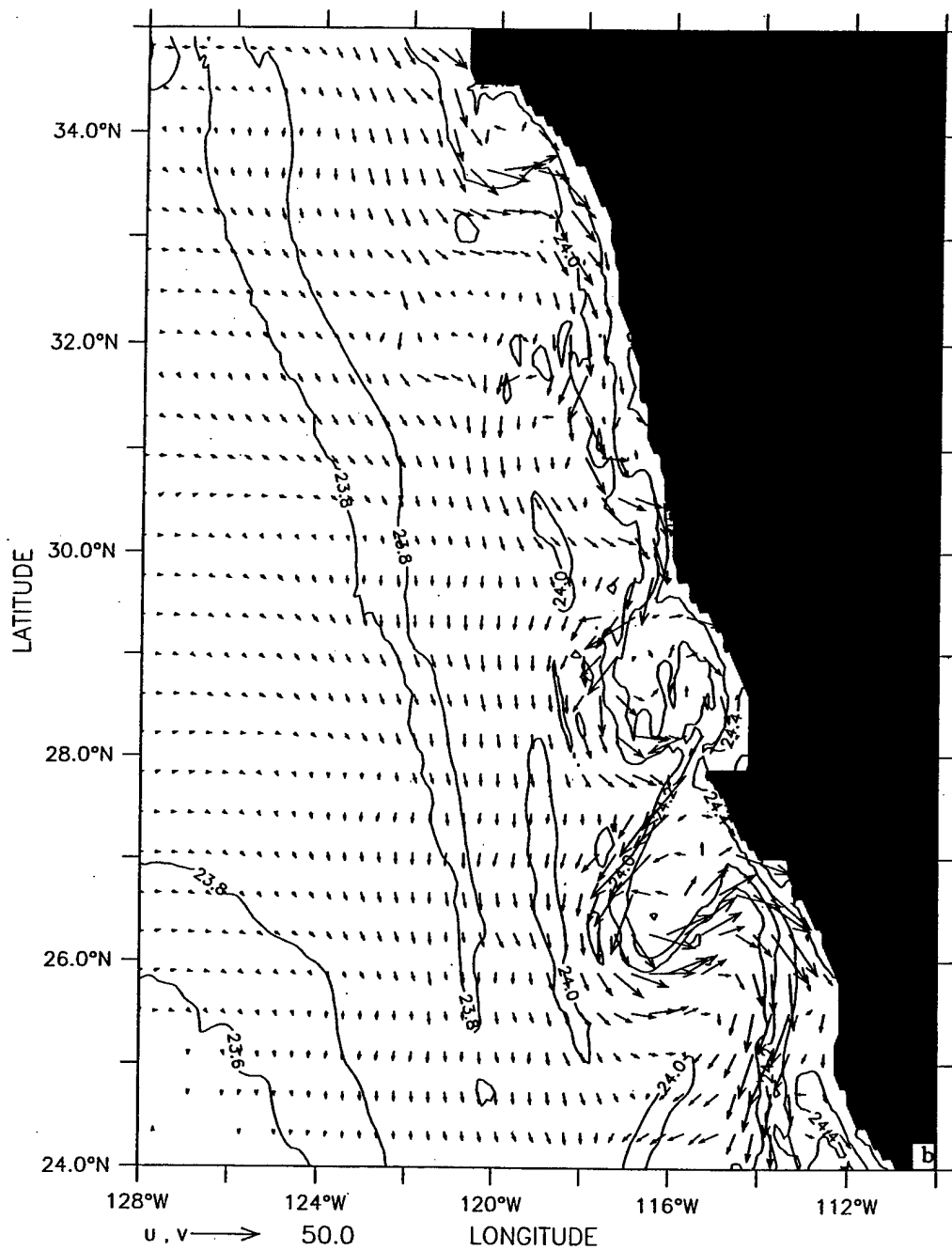
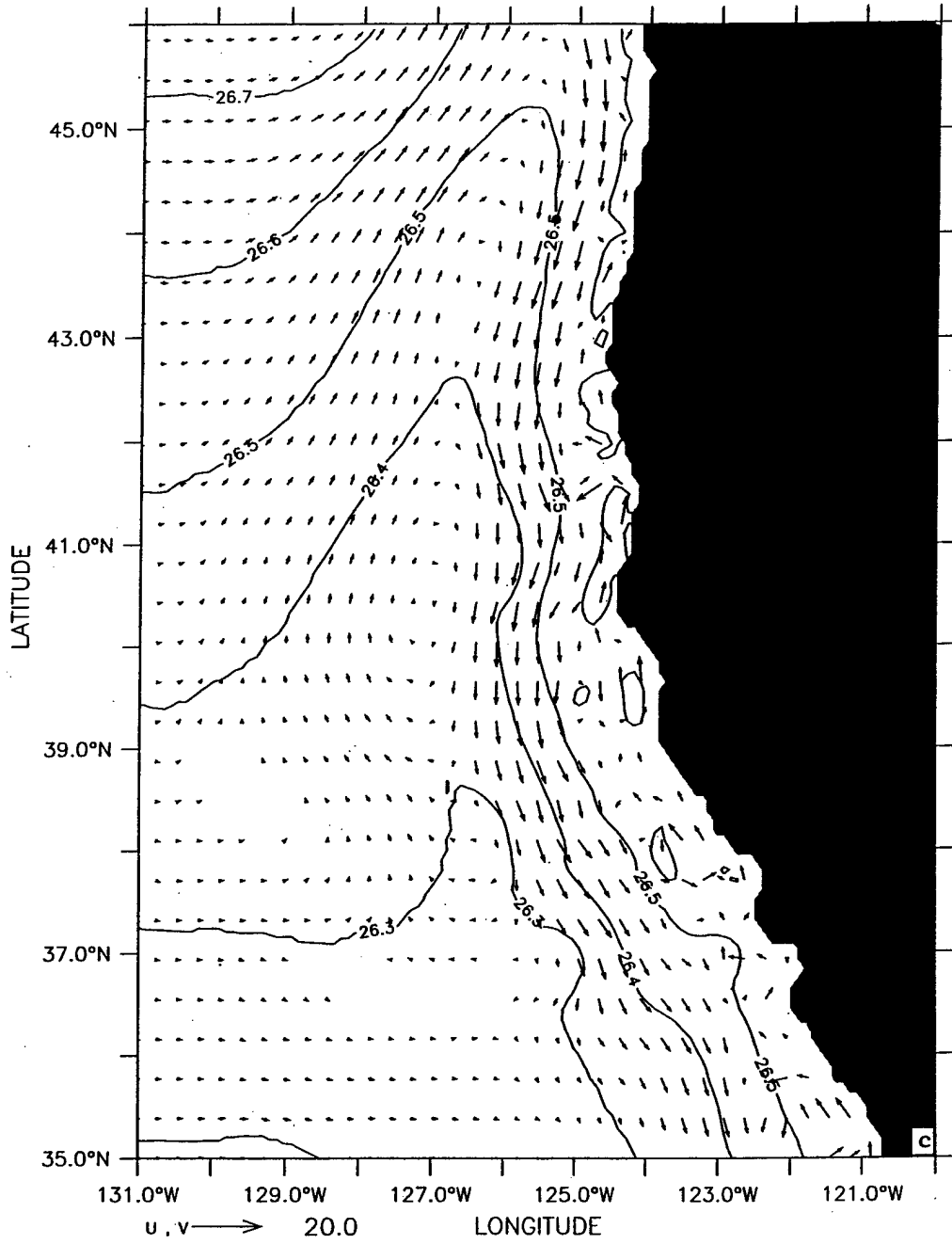


**Figure 10.** Day 195 density contours and velocity vectors for the northern (a,c) and southern (b,d) portions of the model domain at depths 13 m (a,b) and 316 m (c,d). Contour interval is 0.2 g/cm<sup>3</sup> in (a) and (b), and 0.1 g/cm<sup>3</sup> in (c) and (d); maximum velocity vector is 50 cm/s in (a) and (b) and 20 cm/s in (c) and (d).

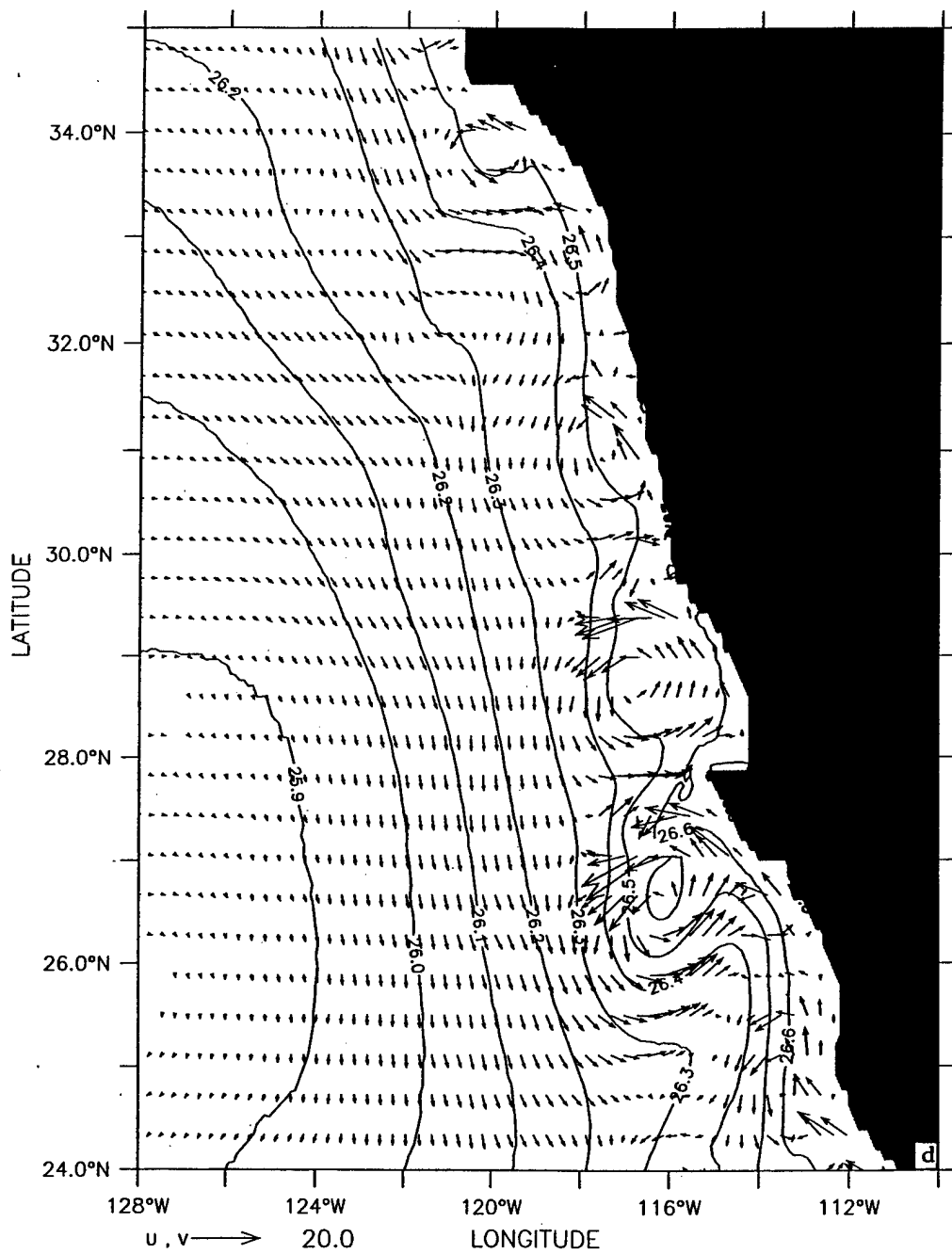
DEPTH : 13m  
T (DAY) : 195



DEPTH : 316m  
T (DAY) : 195



DEPTH : 316m  
T (DAY) : 195



LATITUDE : 46N  
T (DAY) : 195

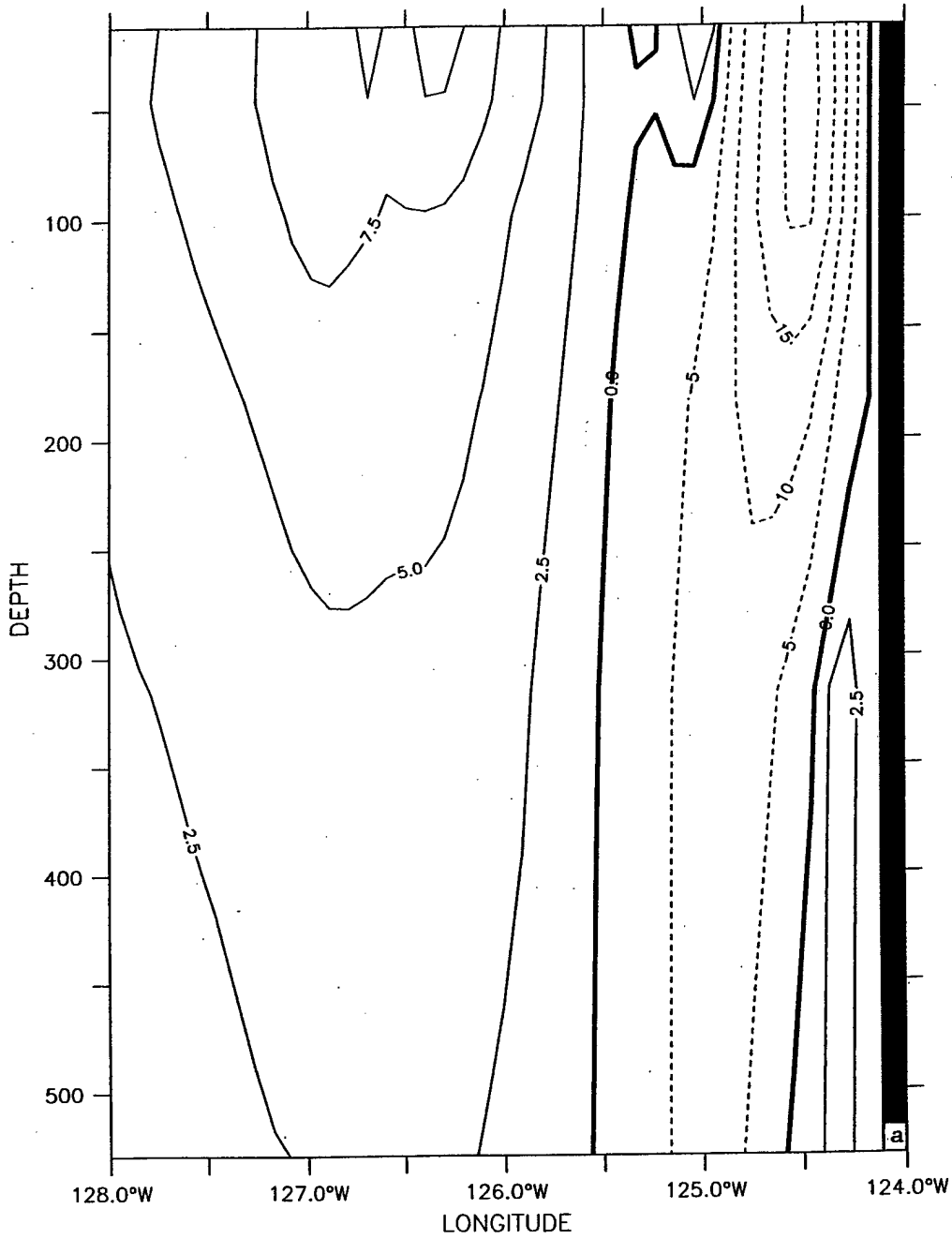
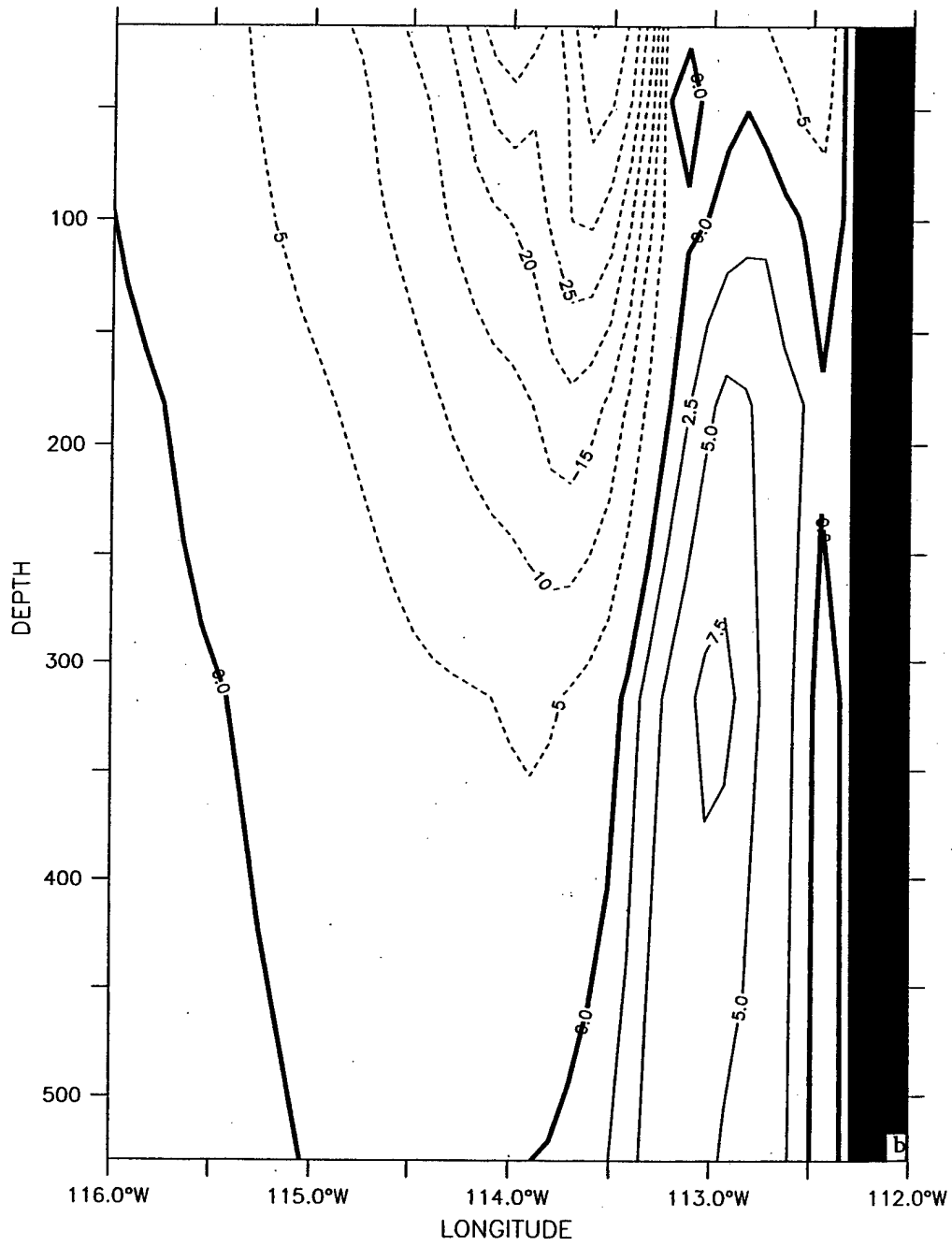


**Figure 11.** Cross-shore sections of  $v$  at (a) 46° N (off northern Oregon) and (b) 25° N (off Cape San Lazaro) for day 195. The contour interval is 2.5 cm/s (5 cm/s) for poleward (equatorward) flow.

LATITUDE : 25N  
T (DAY) : 195





LATITUDE : 25N  
T (DAY) : 285

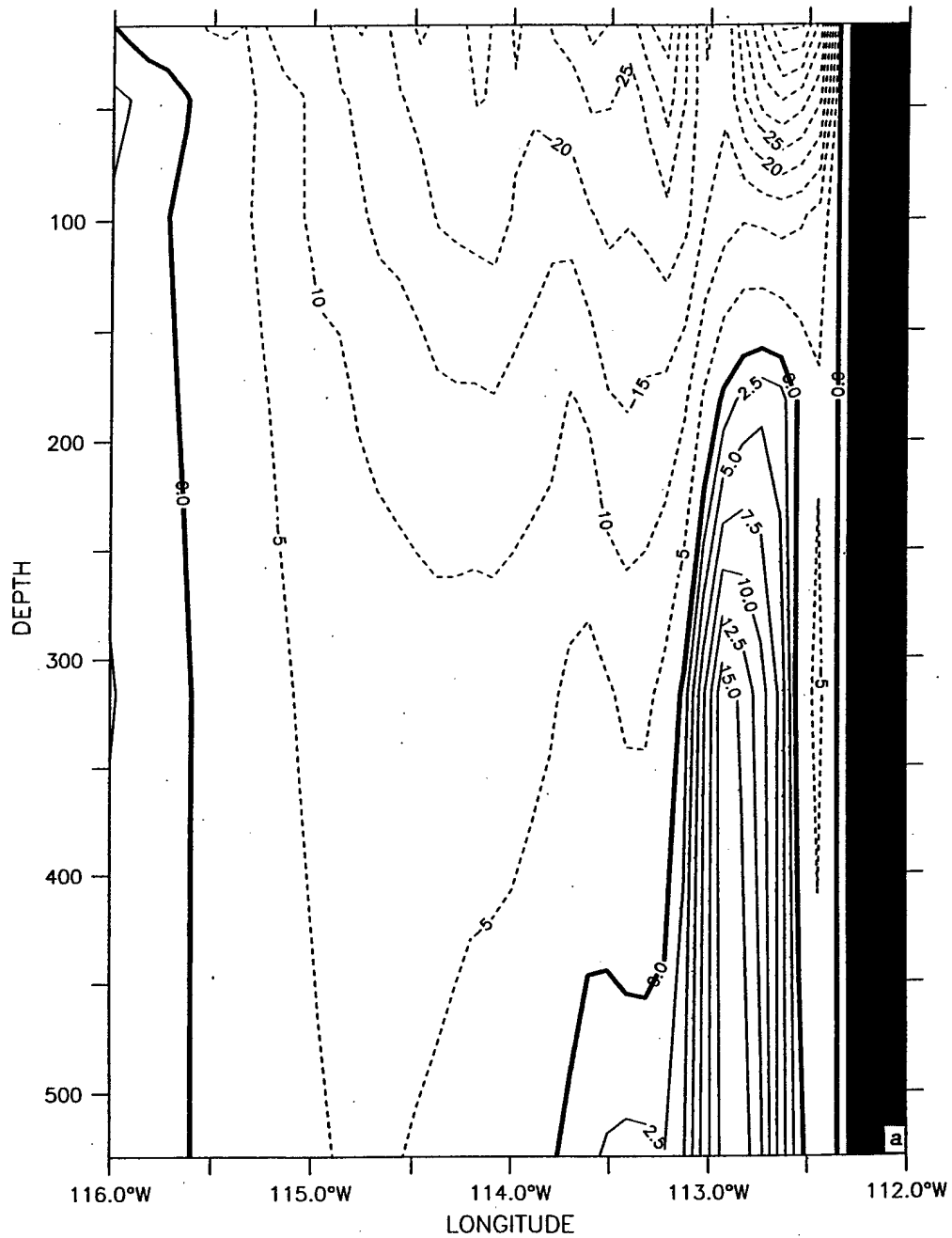
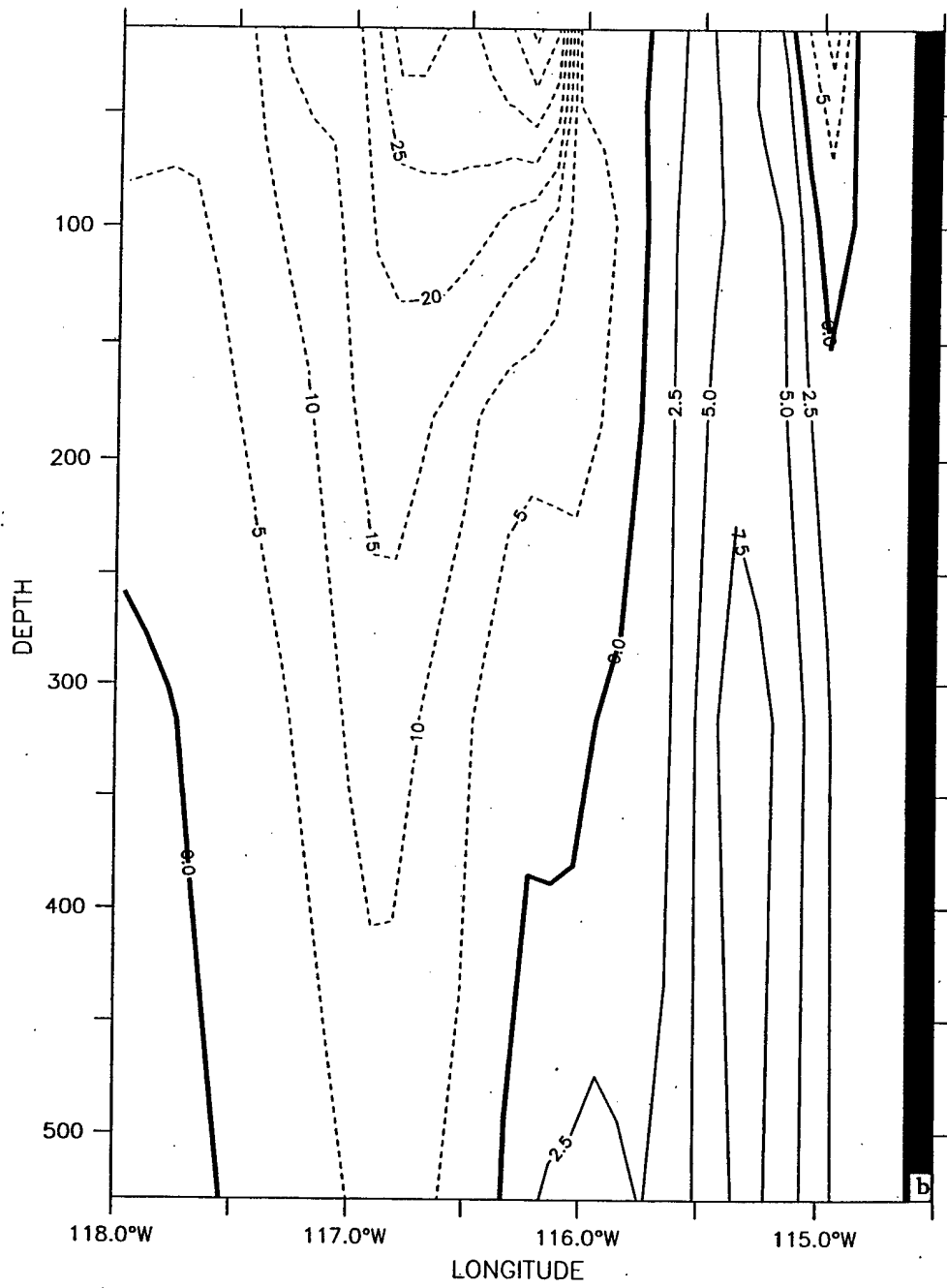
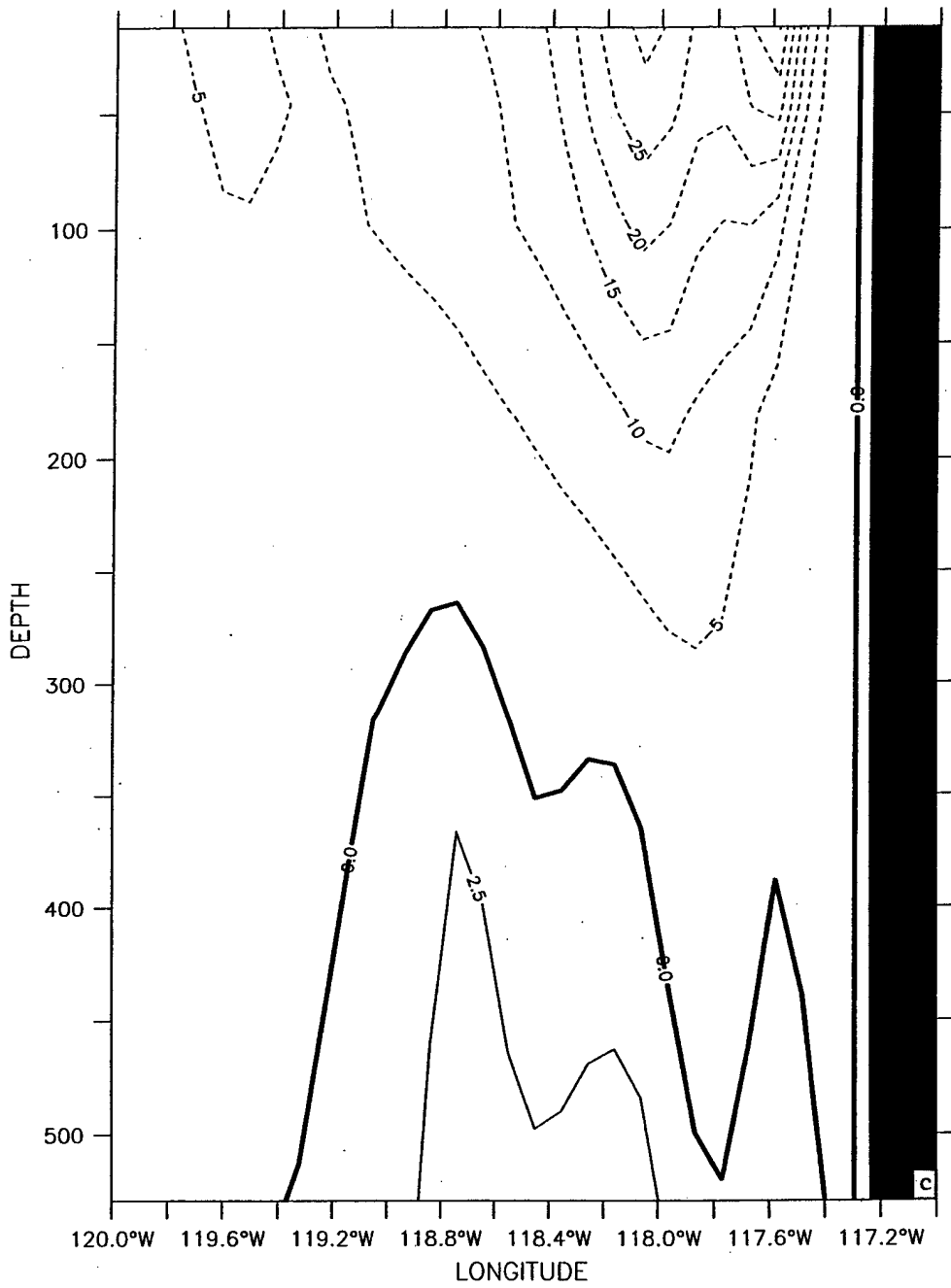


**Figure 12.** Cross-shore sections of  $v$  at (a) 25° N (off Cape San Lazaro), (b) 29° N (north of Point Eugenia), (c) 32.5° N (Southern California Bight), (d) 36.5° N (off Point Sur), and (e) 43° N (off Cape Blanco) on day 285. The contour interval is 2.5 cm/s (5 cm/s) for poleward (equatorward) flow.

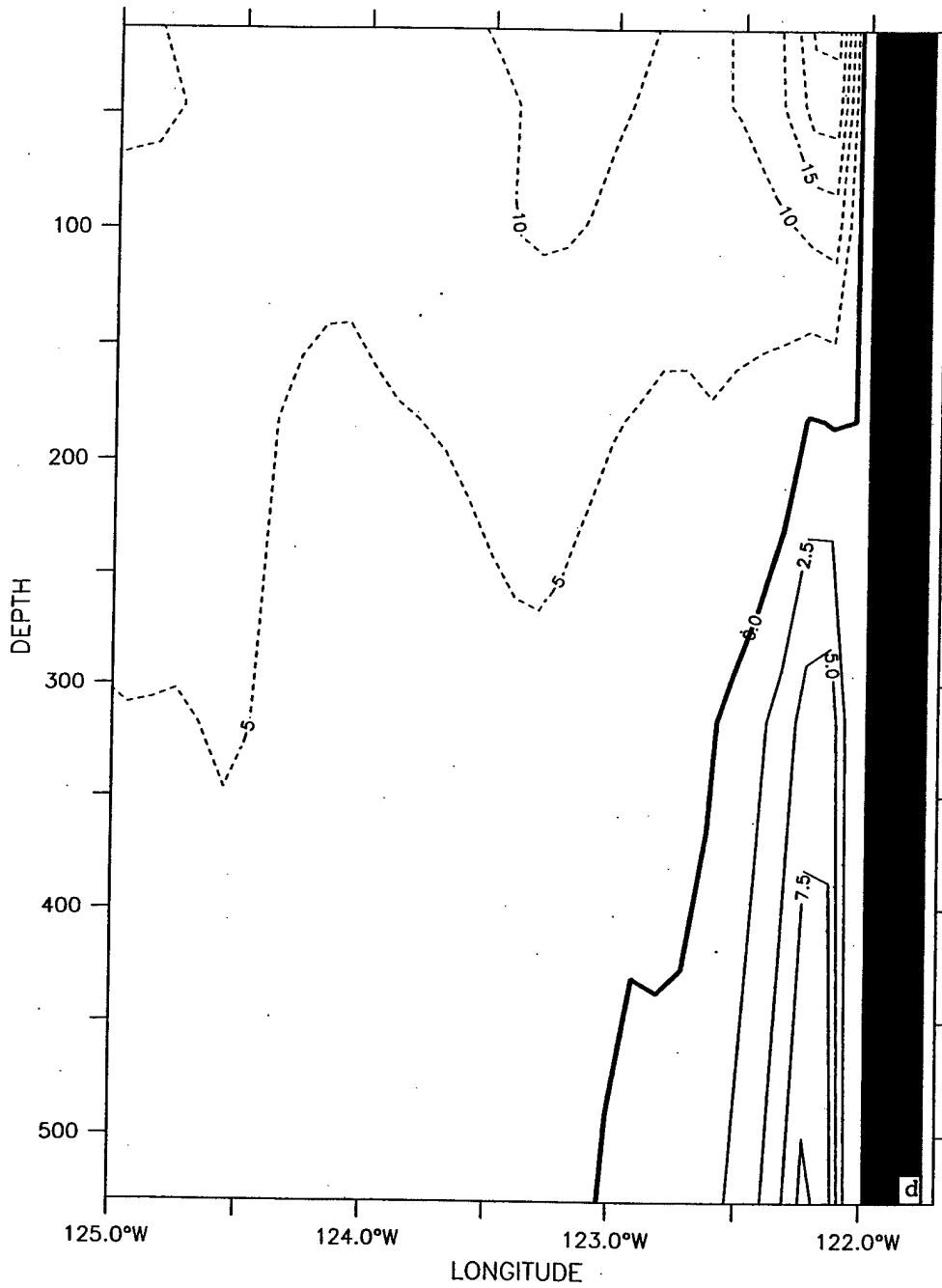
LATITUDE : 29N  
T (DAY) : 285



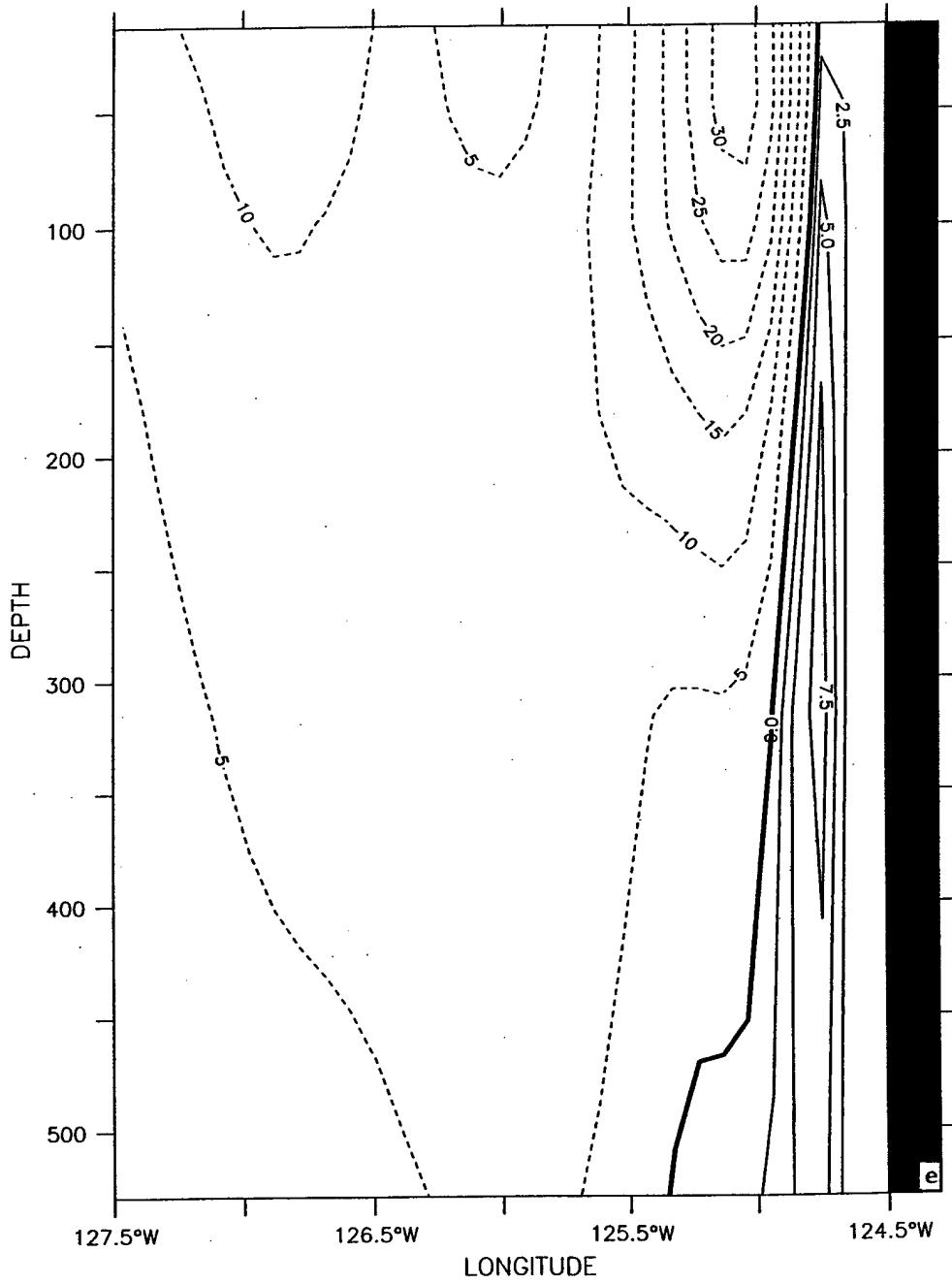
LATITUDE : 32.5N  
T (DAY) : 285



LATITUDE : 36.5N  
T (DAY) : 285



LATITUDE : 4.3N  
T (DAY) : 285



DEPTH : 13m  
T (DAY) : 300

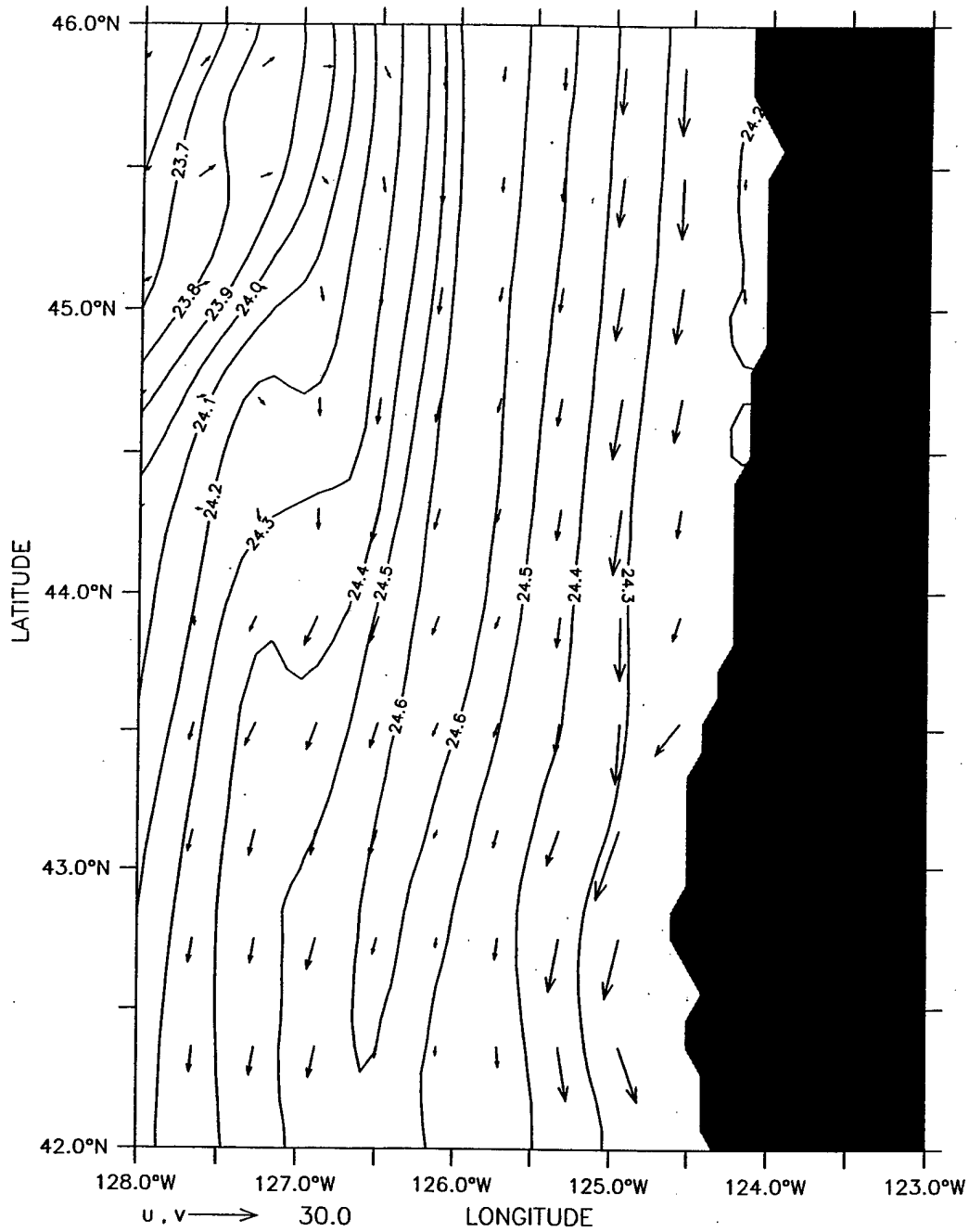


**Figure 13.** Day 300 density contours and velocity vectors at 13 m depth for the northern portion of the domain from 42° N to 46° N. Contour interval is 0.1 g/cm<sup>3</sup>; maximum velocity vector is 30 cm/s.

DEPTH : 13m  
T (DAY) : 300

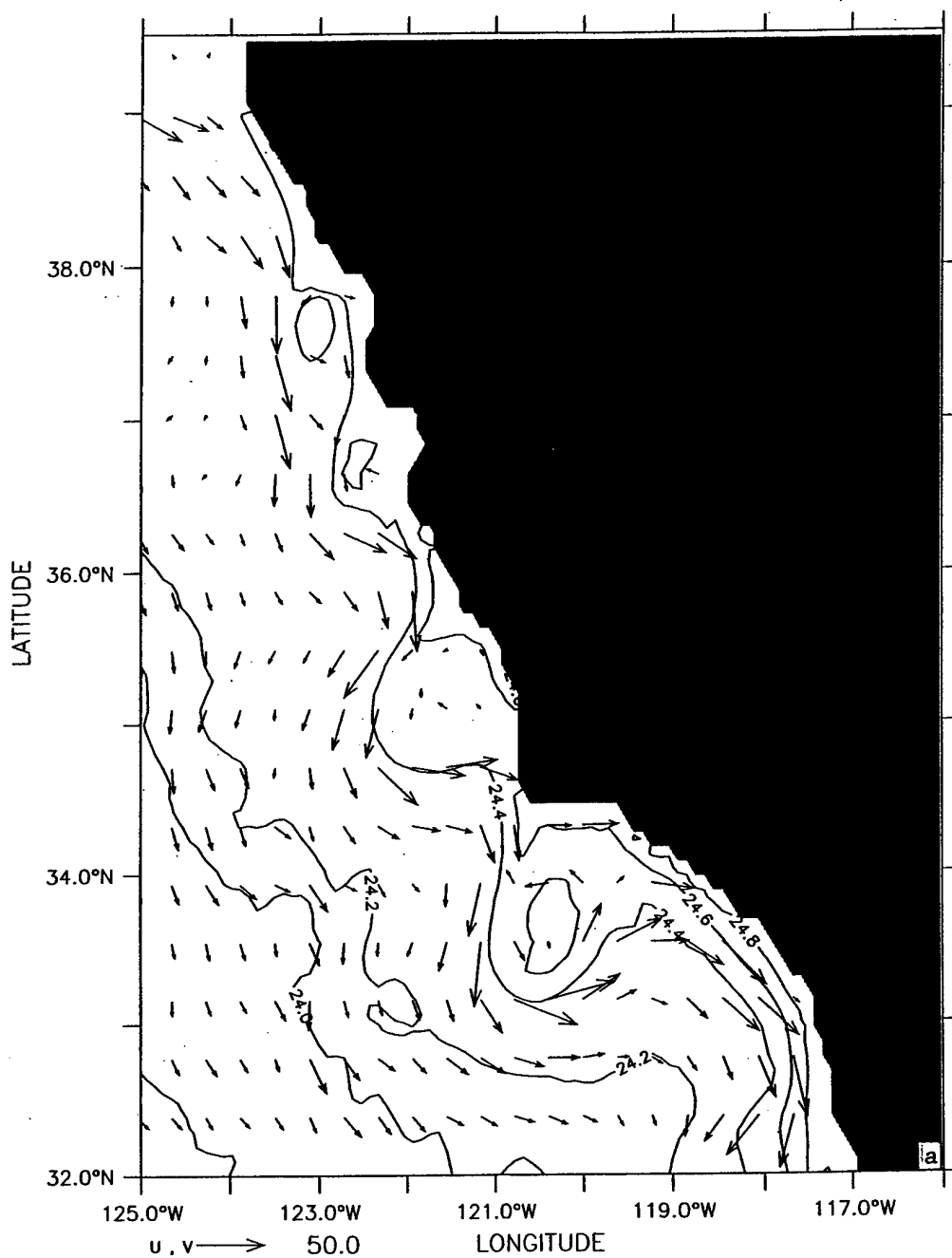
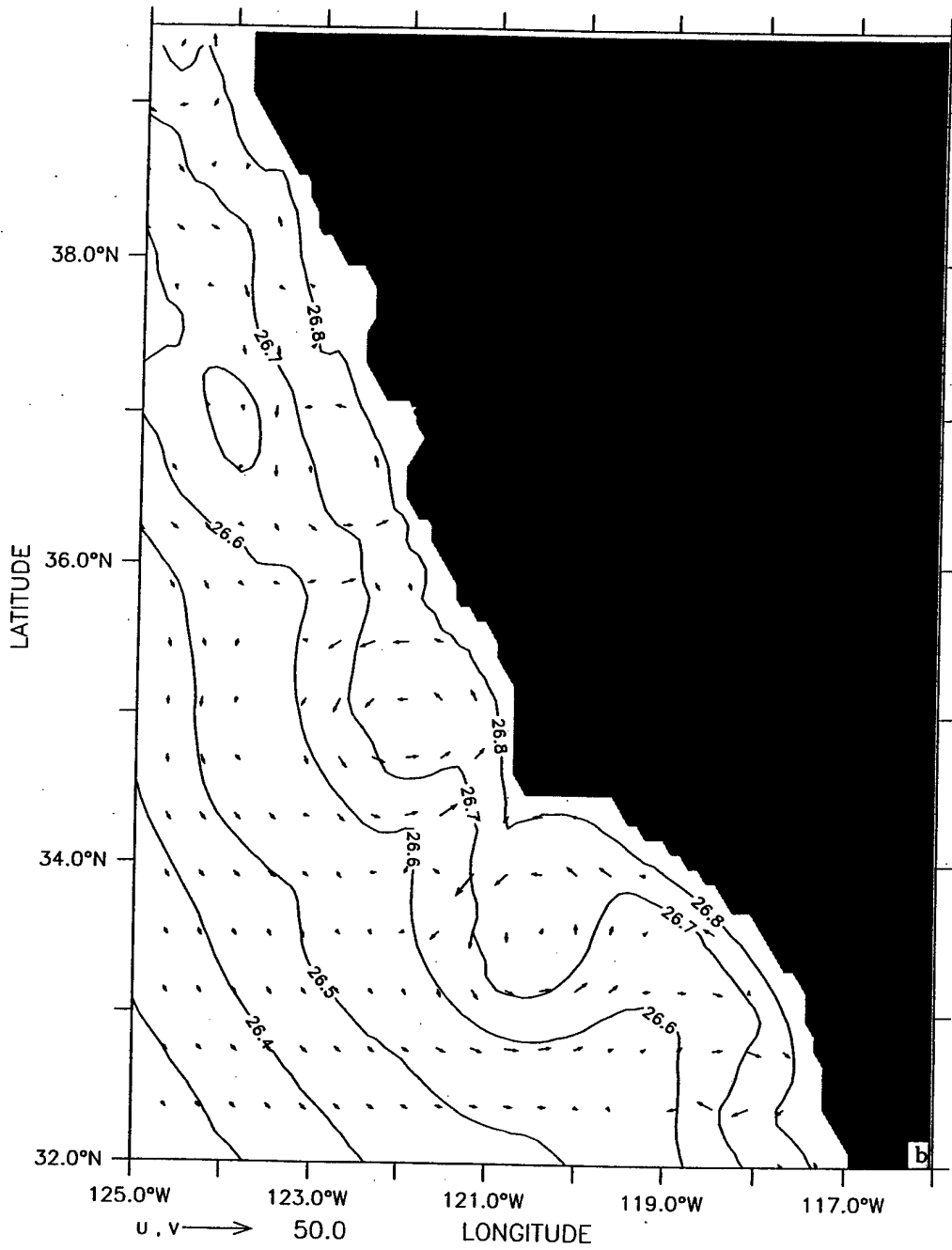


**Figure 14.** Day 300 density contours and velocity vectors at (a) 13 m and (b) 316 m depth for the central portion of the domain from 32° N to 39.5° N. The contour interval is 0.2 g/cm<sup>3</sup> in (a) and 0.1 g/cm<sup>3</sup> in (b). Maximum velocity vector is 50 cm/s.

DEPTH : 316m  
T (DAY) : 300





LATITUDE : 44.2N

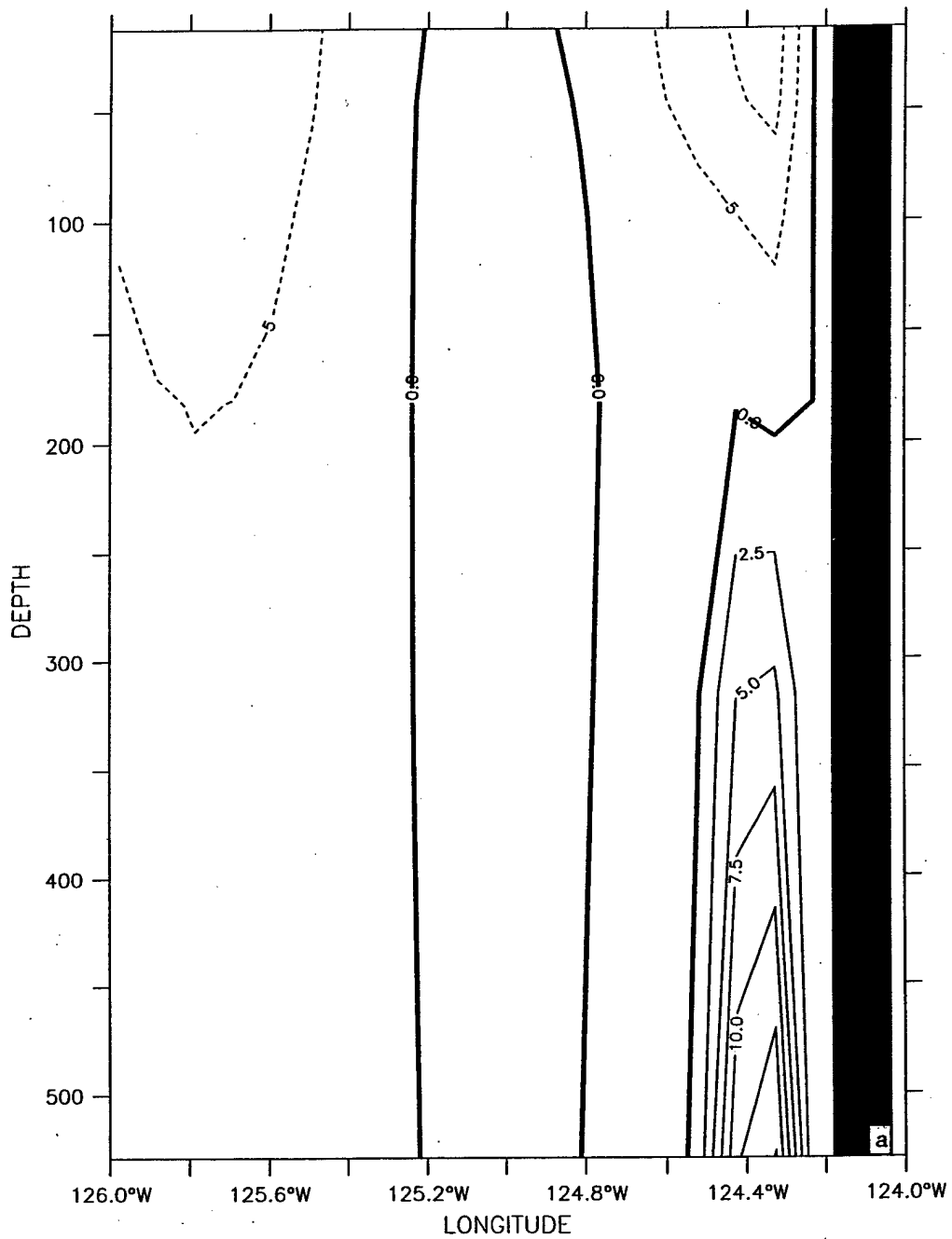
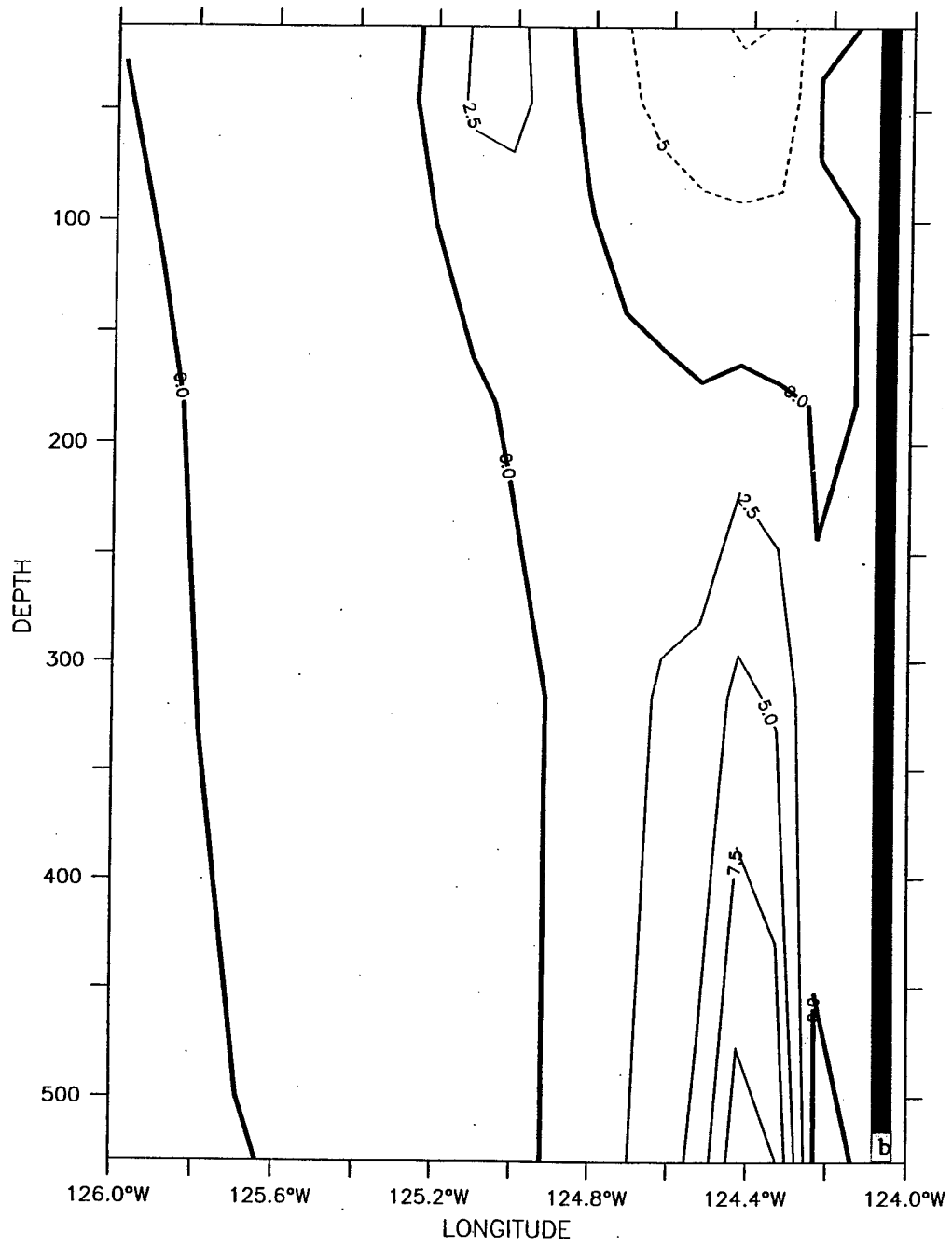


**Figure 15.** Cross-shore sections of mean  $v$  for January of model year 3 at (a) 44.2° N (off Oregon), (b) 41.6° N (off northern California), (c) 34.2° N (south of Point Conception), and (d) 26.3° N (south of Point Eugenia). The contour interval is 2.5 cm/s (5 cm/s) for poleward (equatorward) flow.

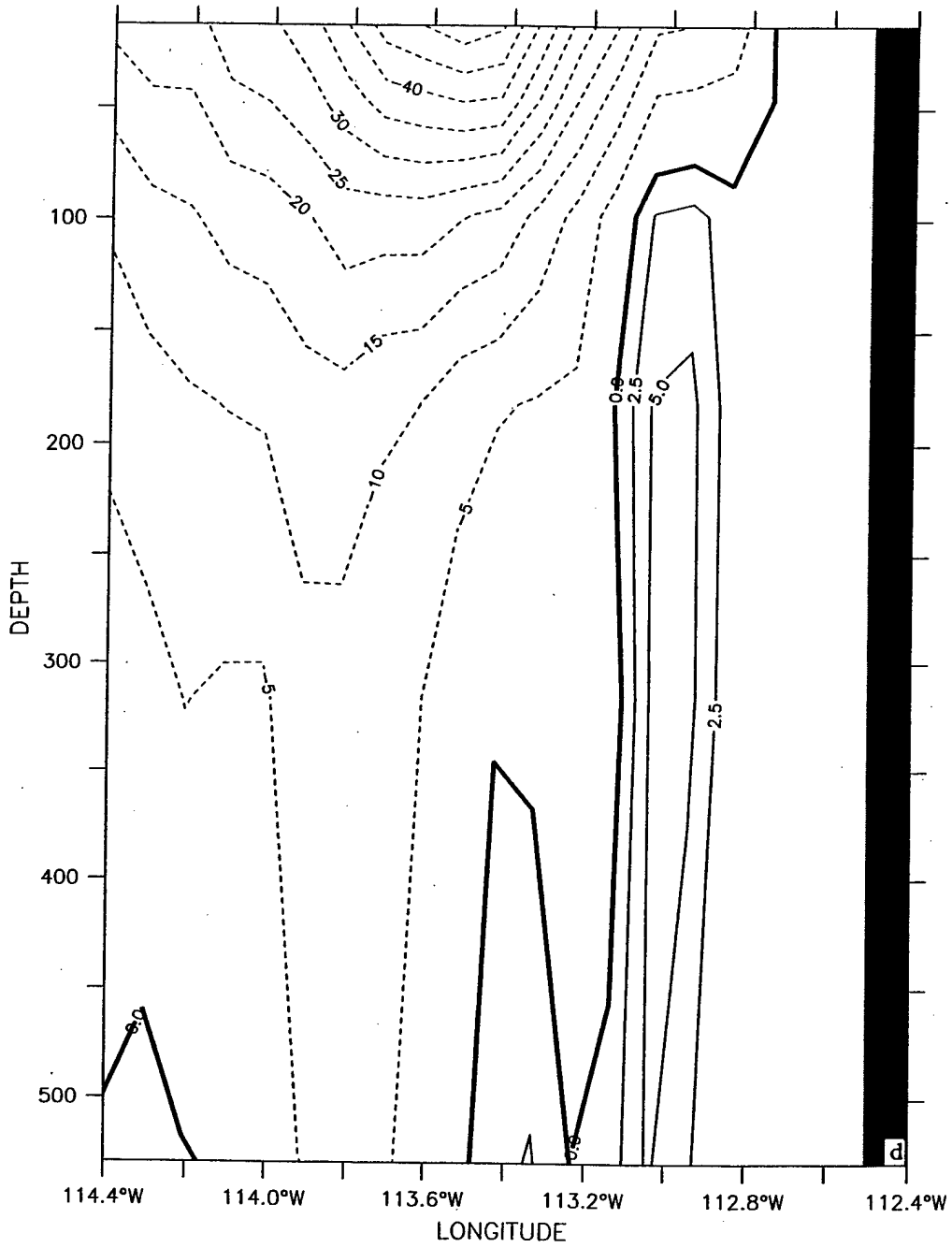
LATITUDE : 41.6N



LATITUDE : 34.2N



LATITUDE : 26.3N



LATITUDE : 44.2N

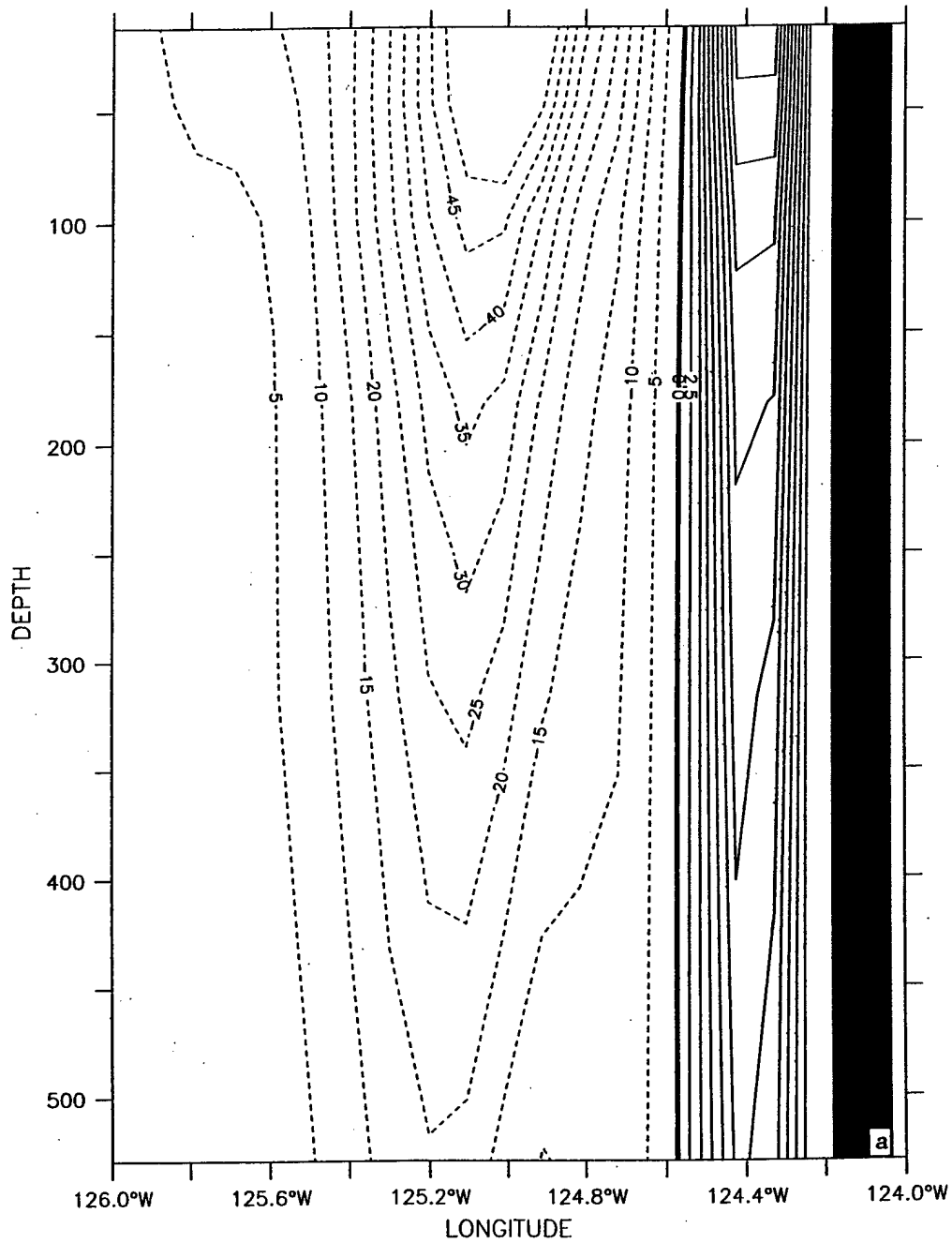
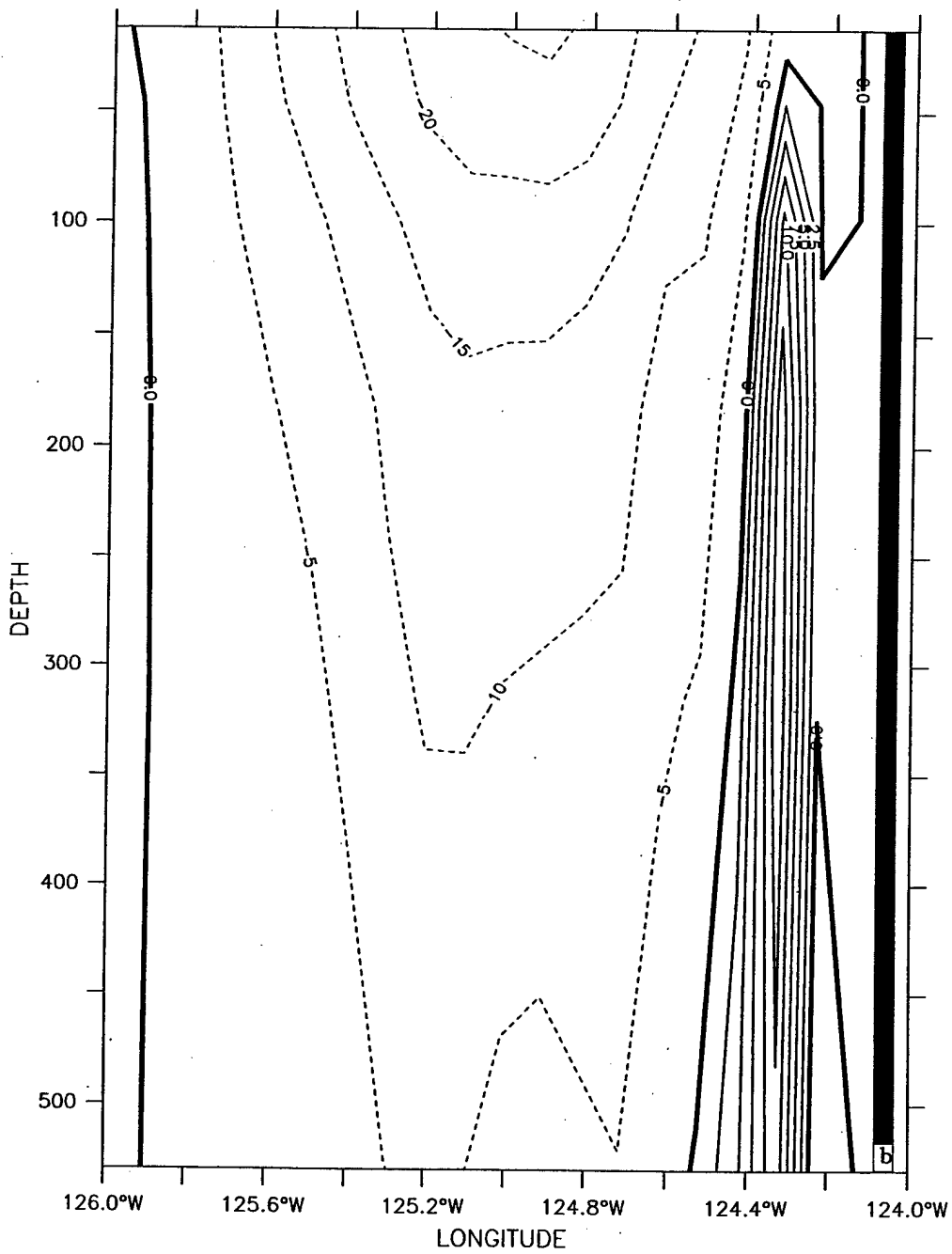
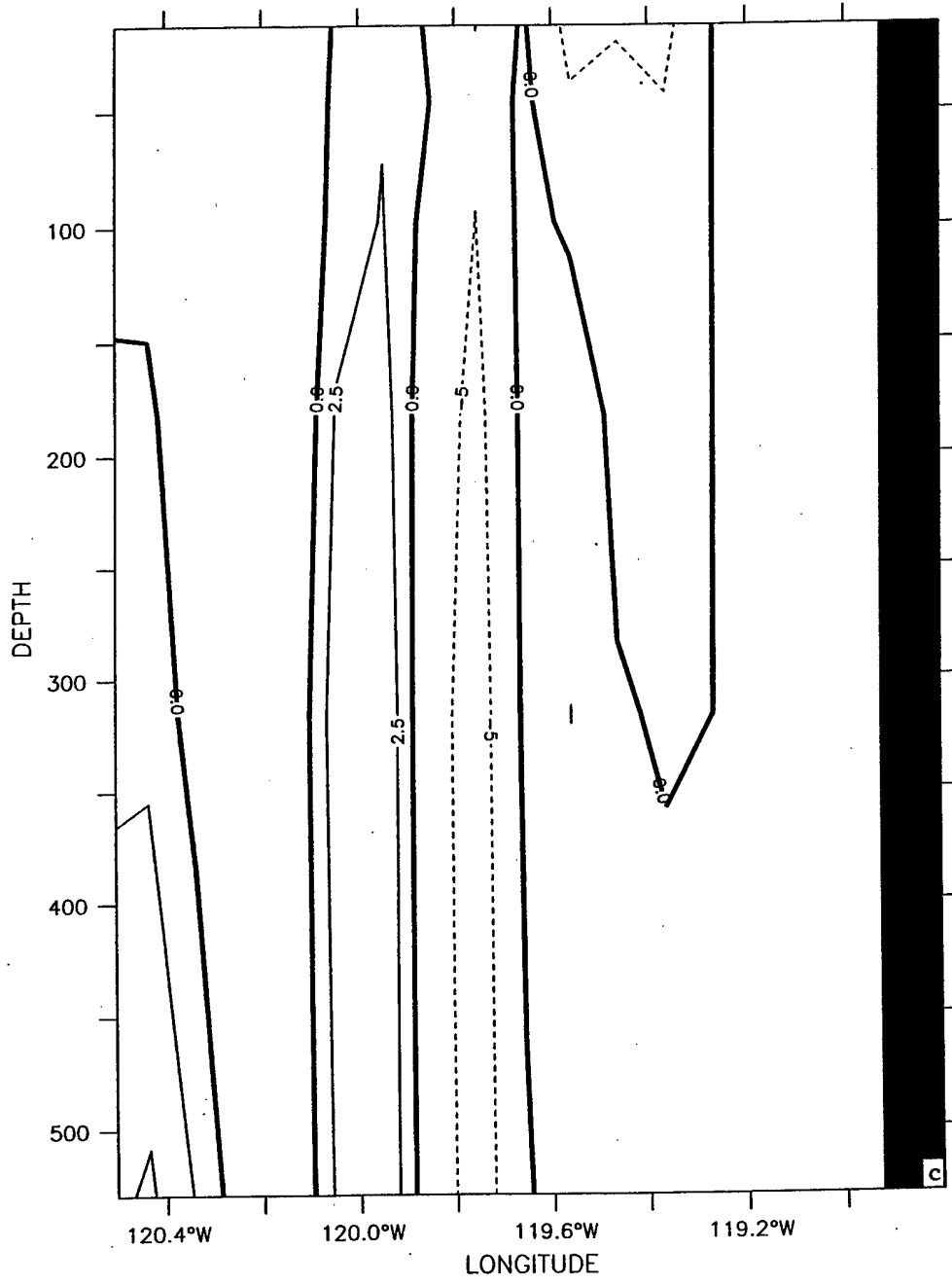


**Figure 16.** Cross-shore sections of mean  $v$  for July of model year 3 at (a) 44.2° N (off Oregon), (b) 41.6° N (off northern California), (c) 34.2° N (south of Point Conception), and (d) 26.3° N (south of Point Eugenia). The contour interval is 2.5 cm/s (5 cm/s) for poleward (equatorward) flow.

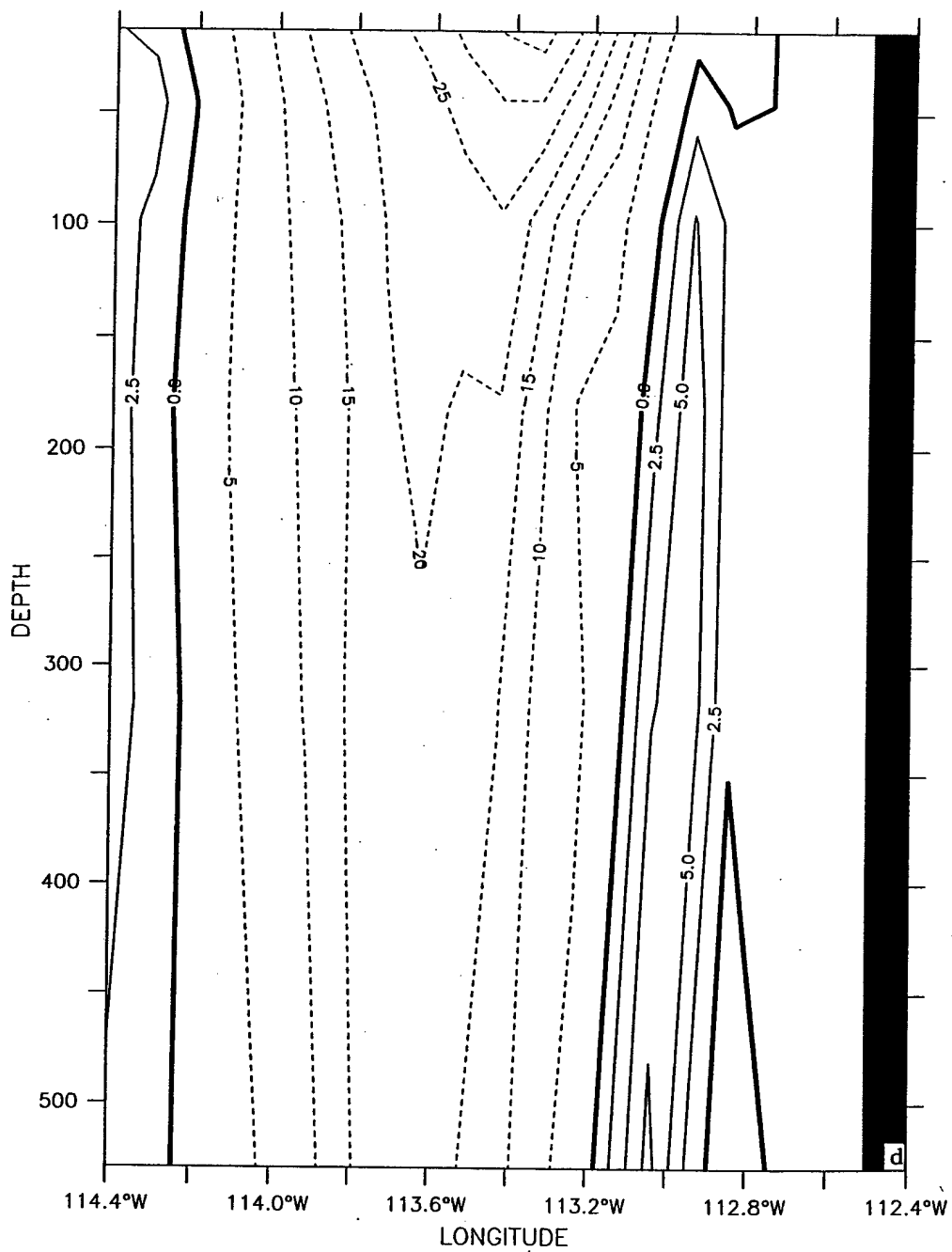
LATITUDE : 41.6N



LATITUDE : 34.2N



LATITUDE : 26.3N





DEPTH : 13m

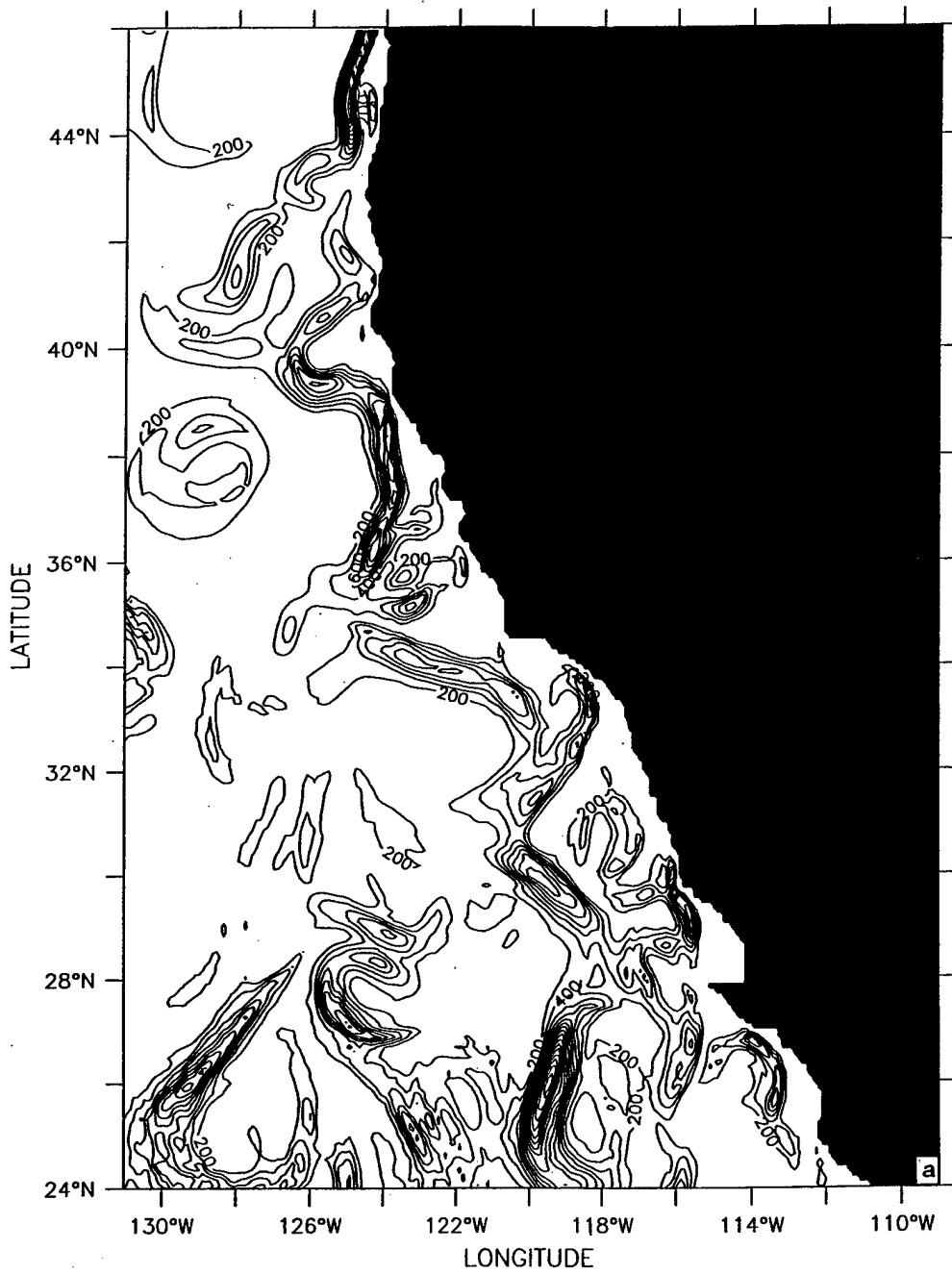
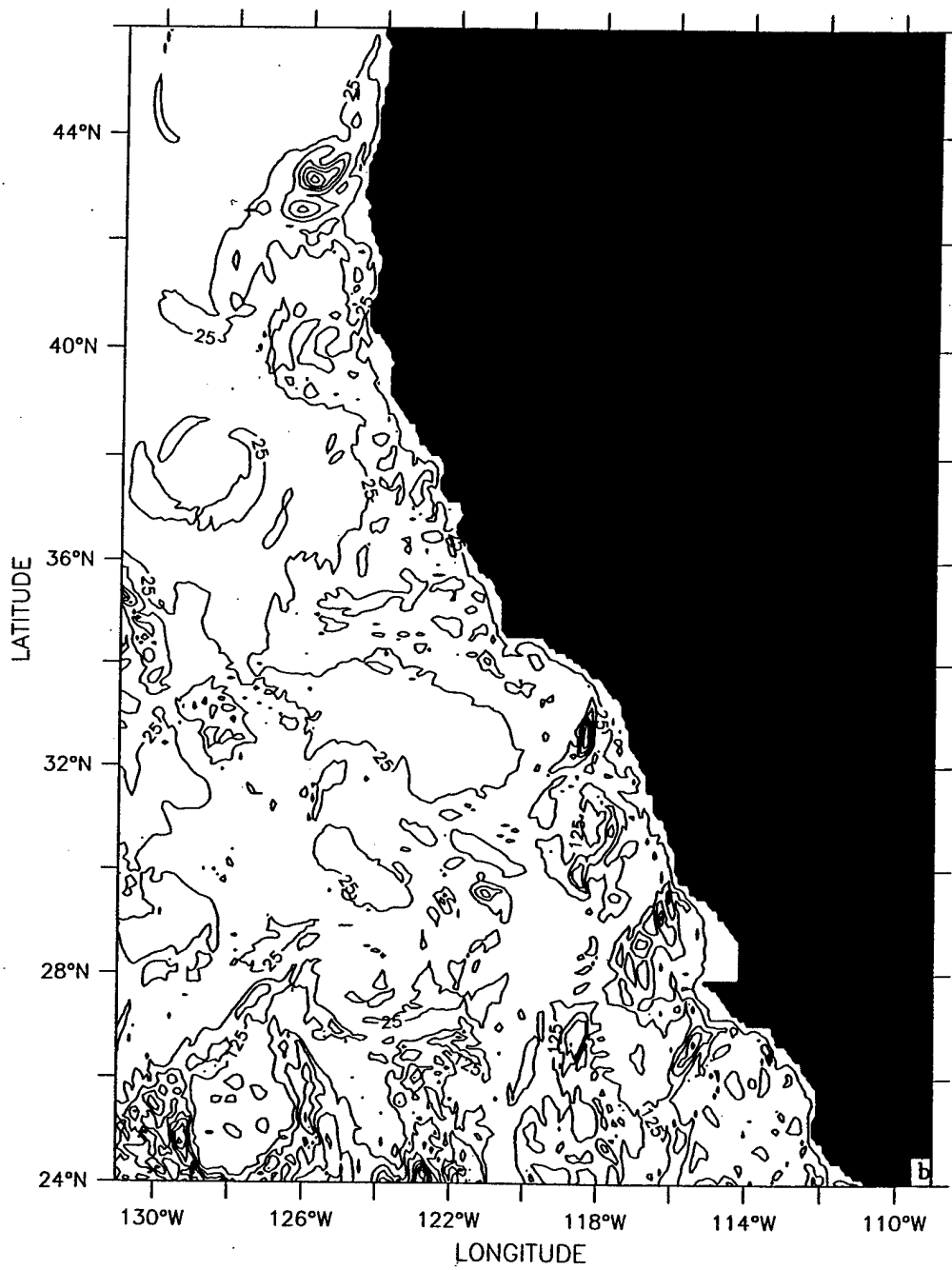


**Figure 17.** Horizontal maps at 13 m depth of (a) mean kinetic energy (MKE), and (b) eddy kinetic energy (EKE) for July of model year 3. Contour interval is  $200 \text{ cm}^2/\text{s}^2$  in (a) and  $100 \text{ cm}^2/\text{s}^2$  in (b).

DEPTH : 13m



LATITUDE : 36.5N

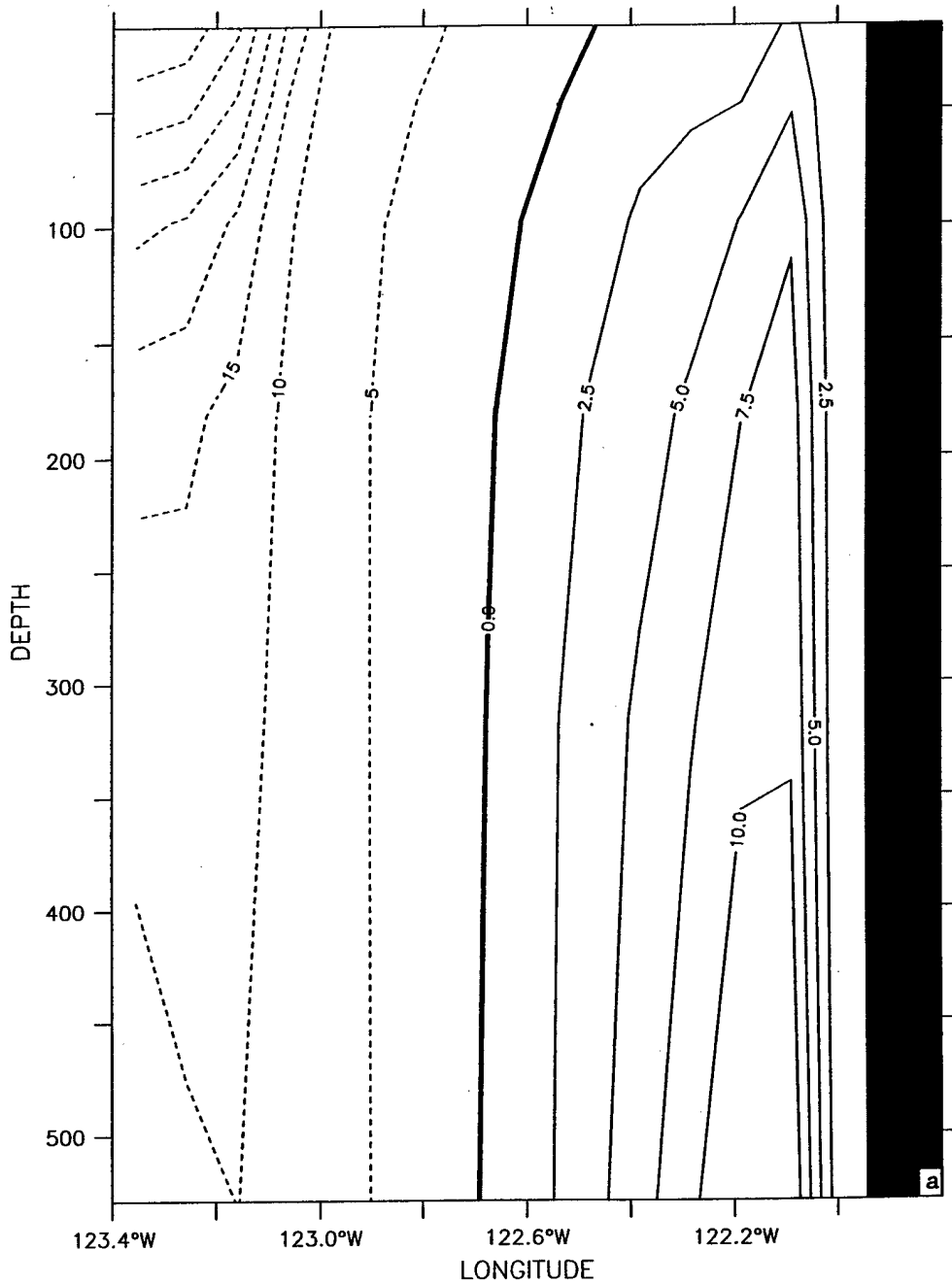
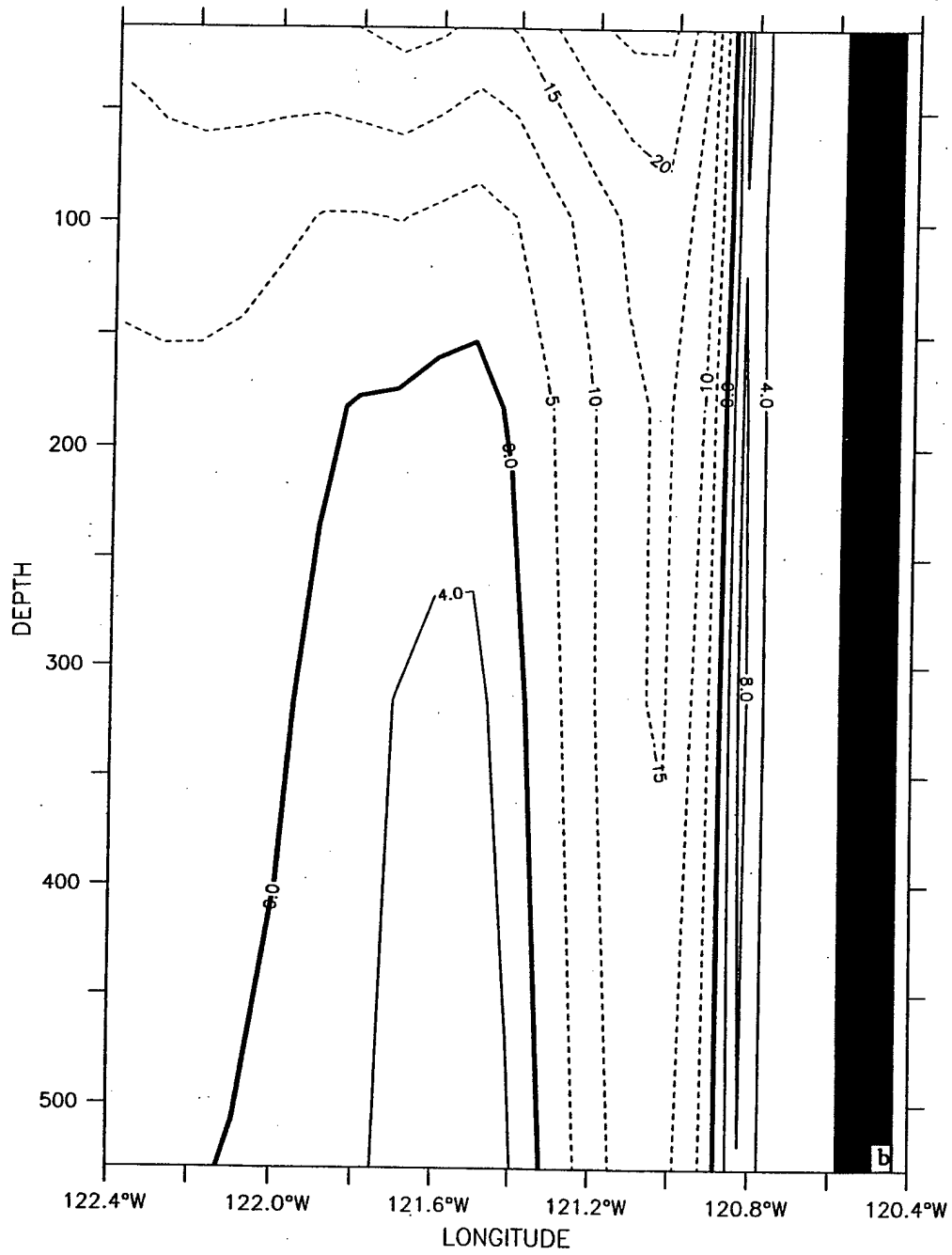
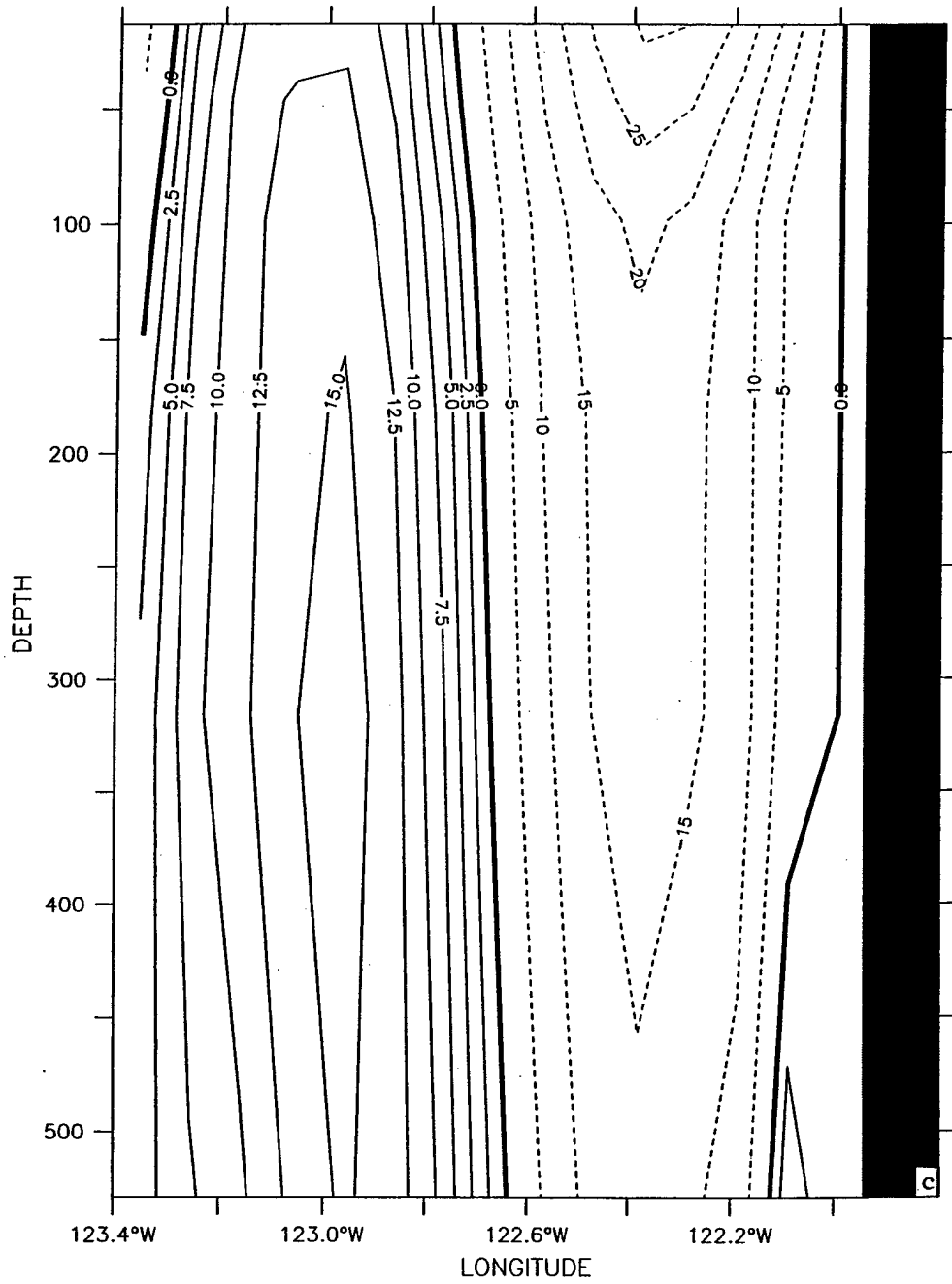


**Figure 18.** Cross-shore sections of mean  $v$  for January of model year 3 at (a) 36.5° N (off Point Sur) and (b) 34.6° N (off Point Conception), and June at (c) 36.5° N and (d) 34.6° N. The contour interval is 2.5 cm/s (5 cm/s) for poleward (equatorward) flow in (a, c, d) and 4 cm/s (5 cm/s) for poleward (equatorward) flow in (b).

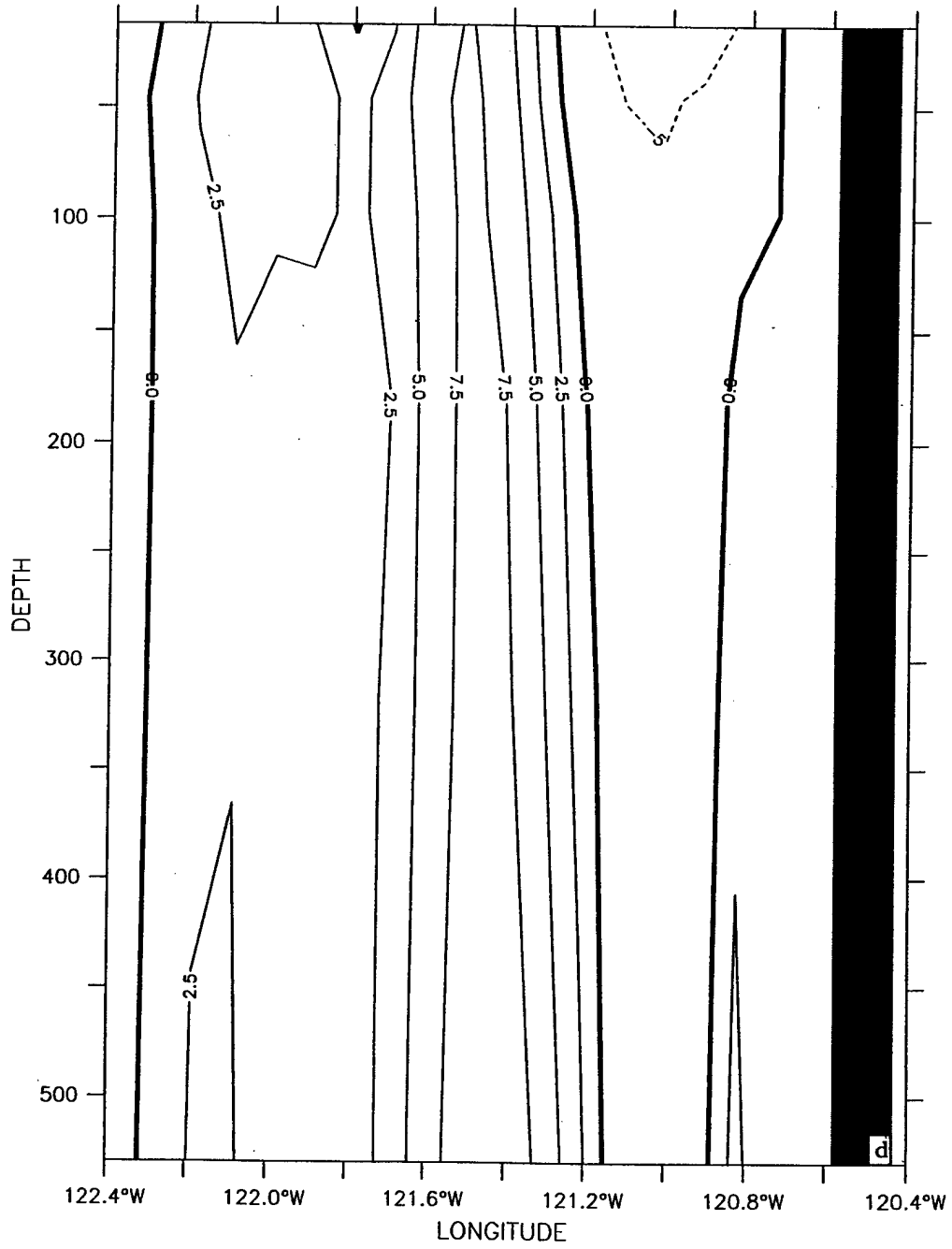
LATITUDE : 34.6N



LATITUDE : 36.5N



LATITUDE : 34.6N



LATITUDE : 33.5N

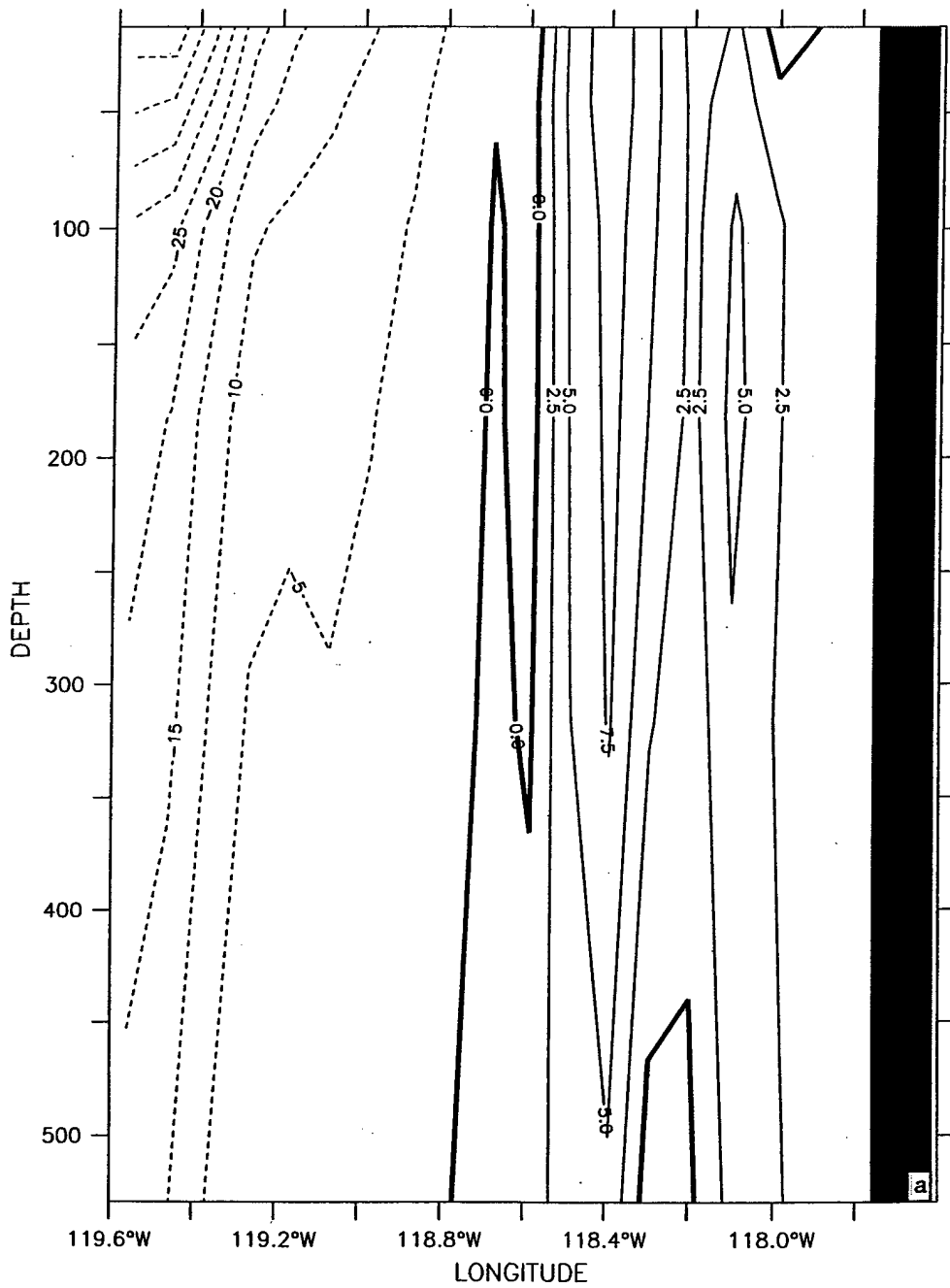
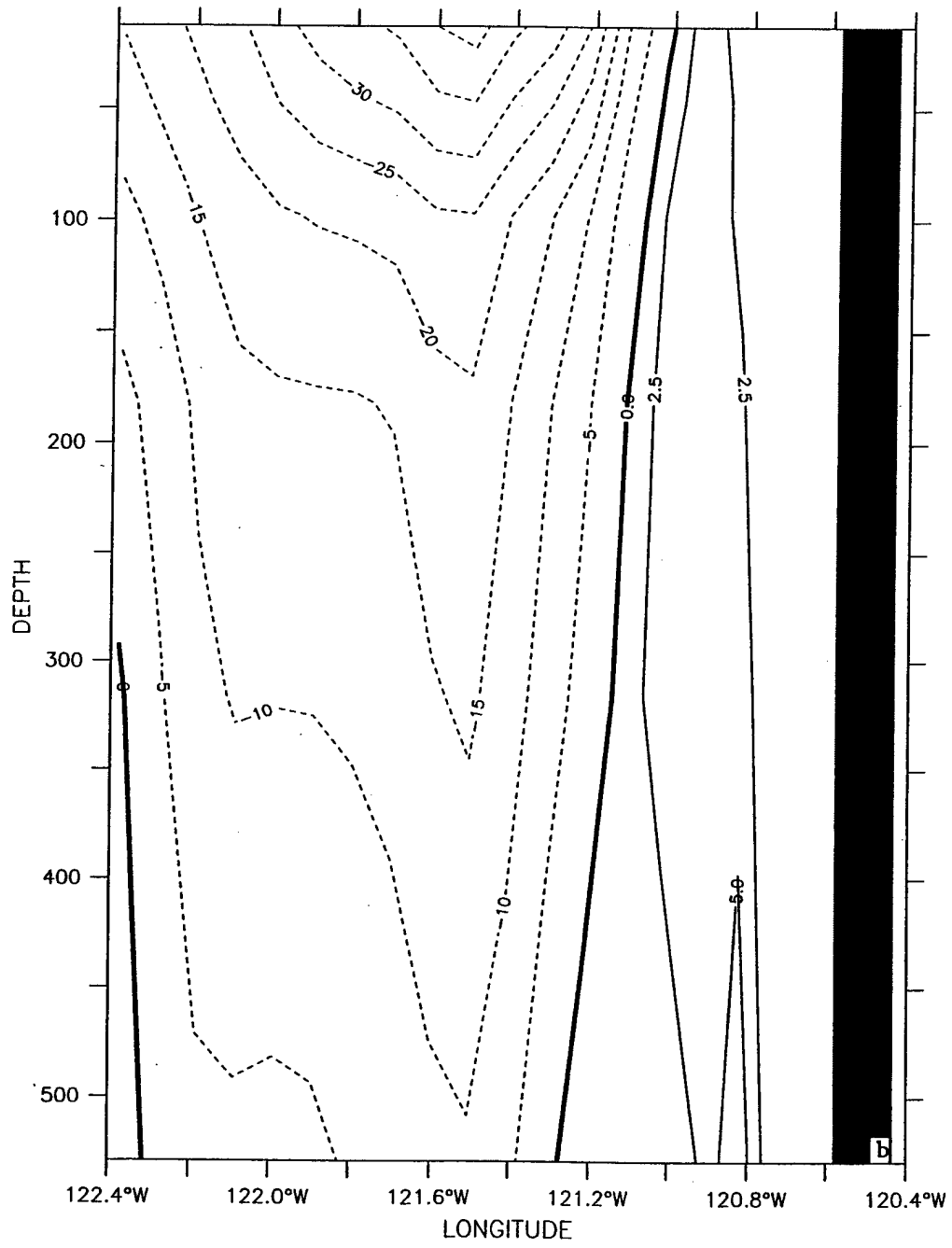


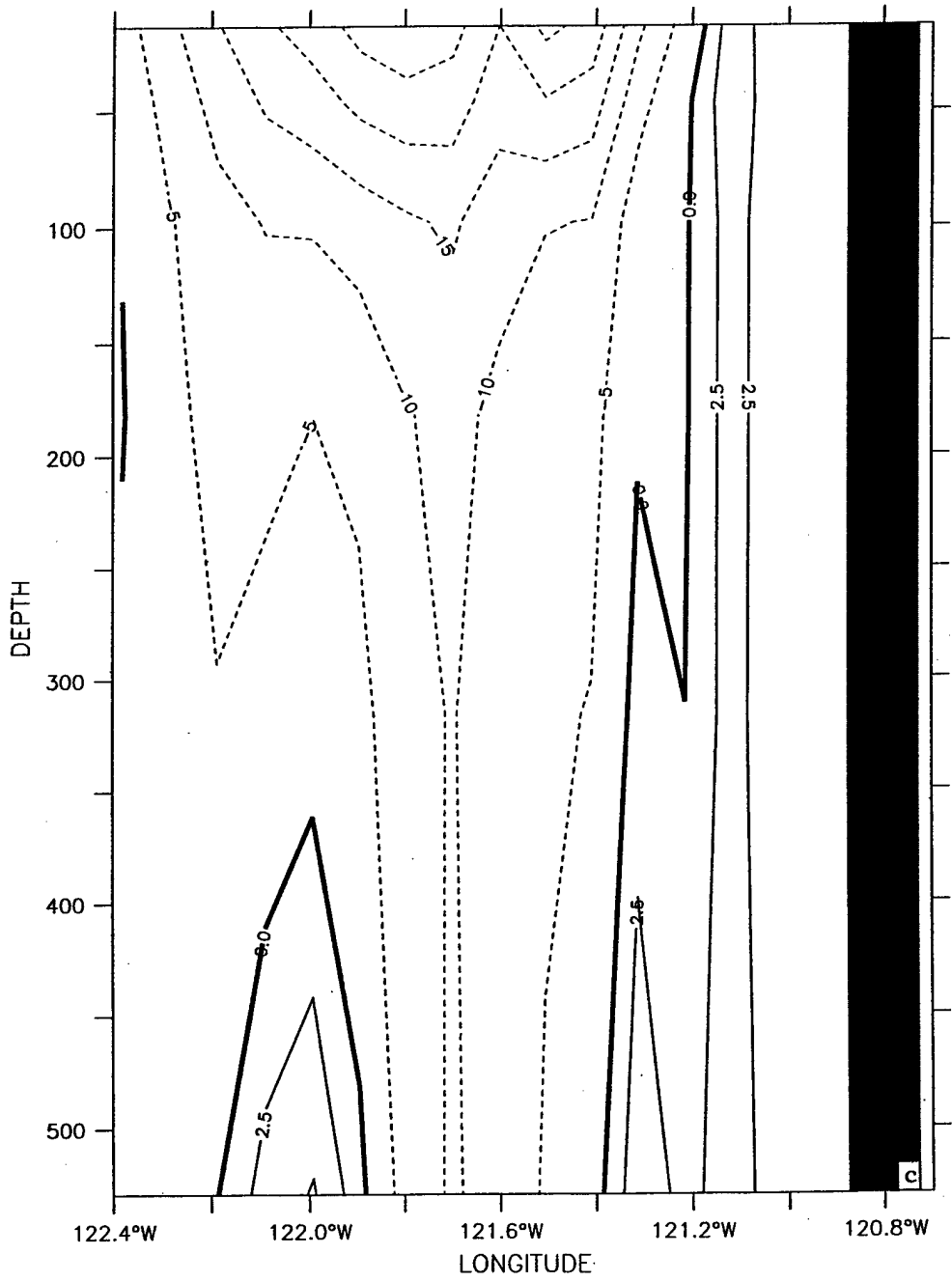
**Figure 19.** Cross-shore sections of mean  $v$  for November of model year 3 at (a) 33.5° N (south of Point Conception), (b) 34.6° N (off Point Conception), and (c) 35.5° N (north of Point Conception). The contour interval is 2.5 cm/s (5 cm/s) for poleward (equatorward) flow.

LATITUDE : 34.6N





LATITUDE : 35.5N



LATITUDE : 32N

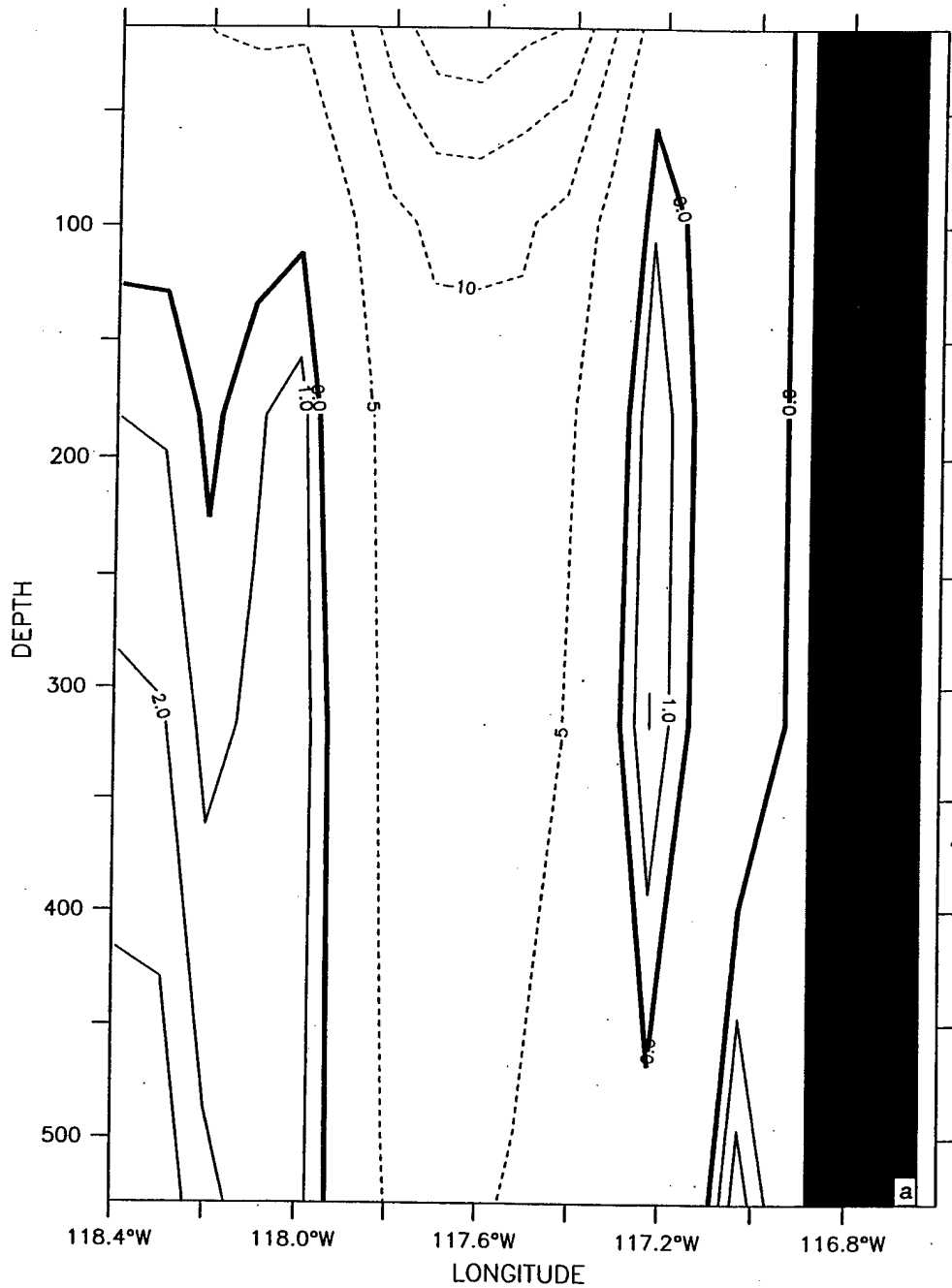
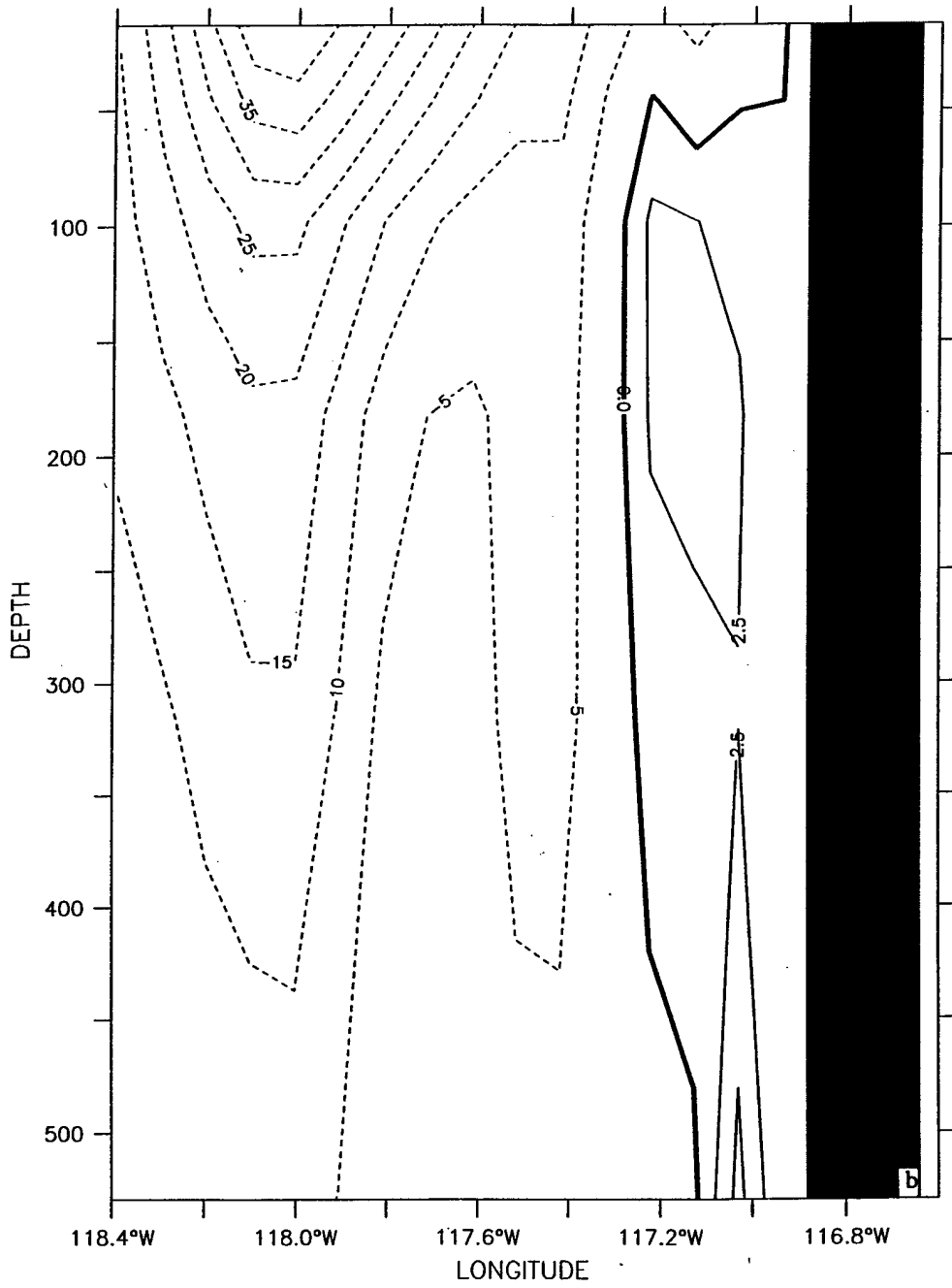
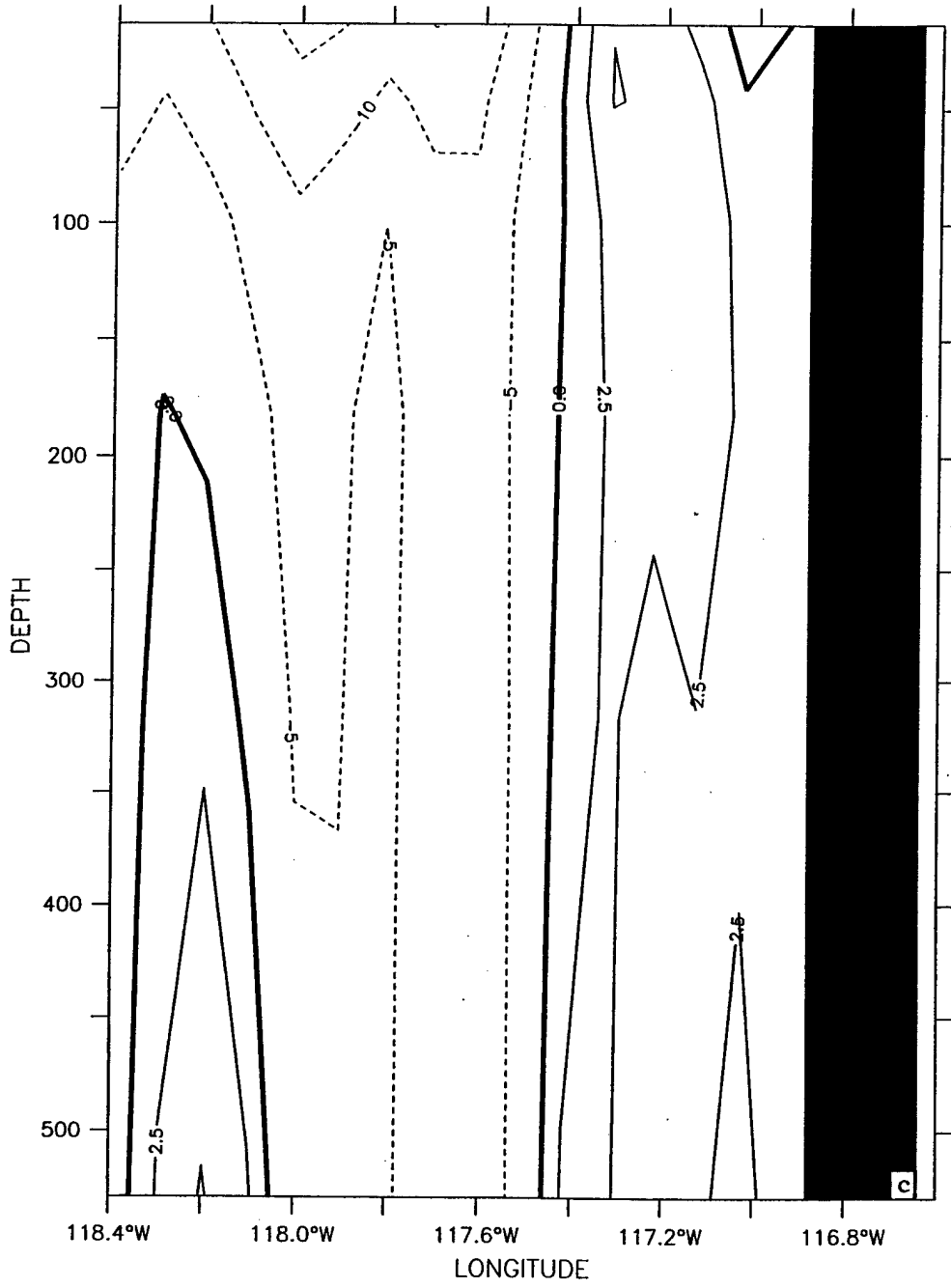


**Figure 20.** Cross-shore sections of mean  $v$  at 32° N for (a) August, (b) September, (c) October, and (d) November of model year 3. The contour interval is 1 cm/s (5 cm/s) for poleward (equatorward) flow in (a) and 2.5 cm/s (5 cm/s) for poleward (equatorward) flow in (b, c, d).

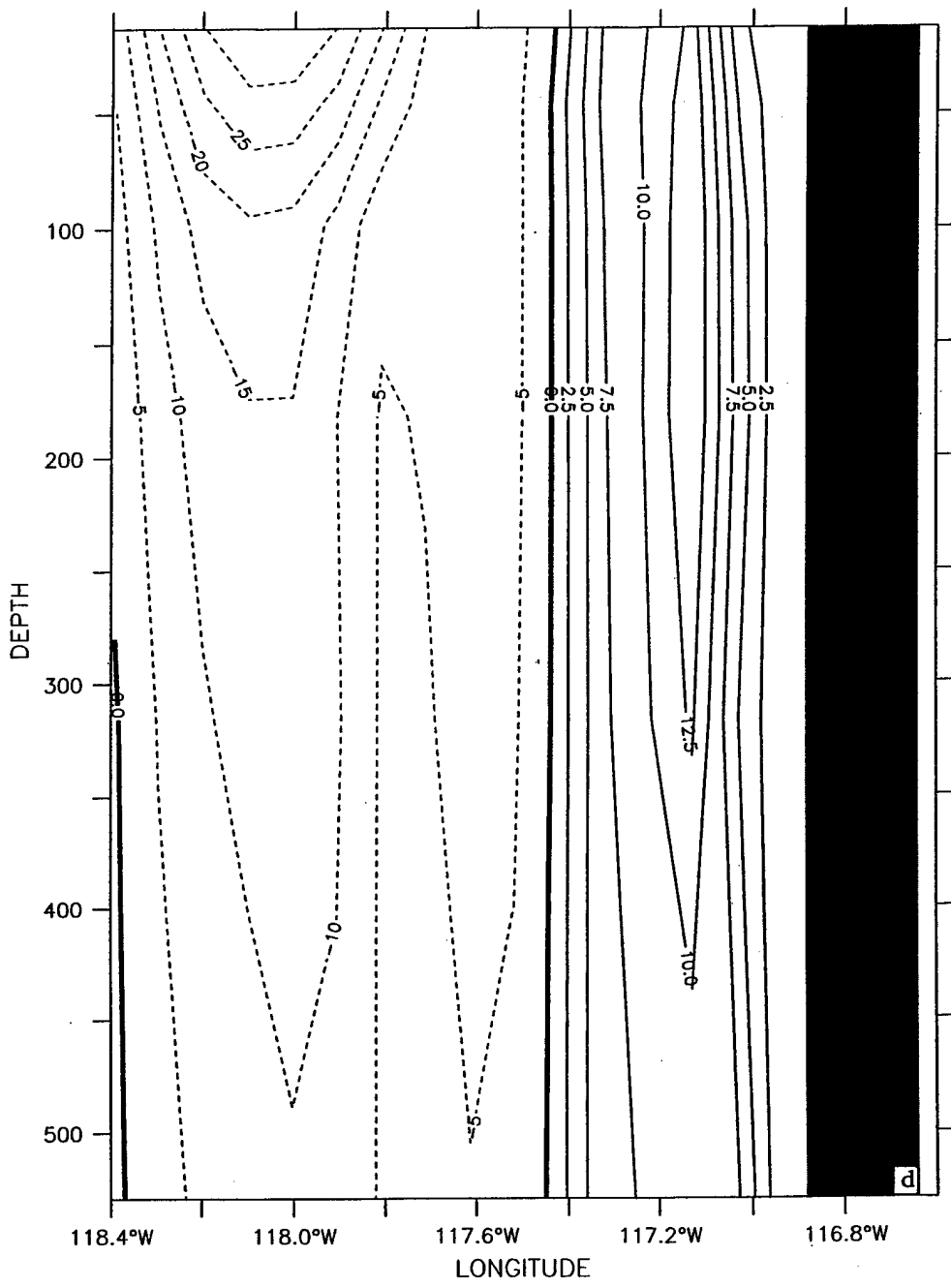
LATITUDE : 32N



LATITUDE : 32N



LATITUDE : 32N



LATITUDE : 26N  
T (DAY) : 924

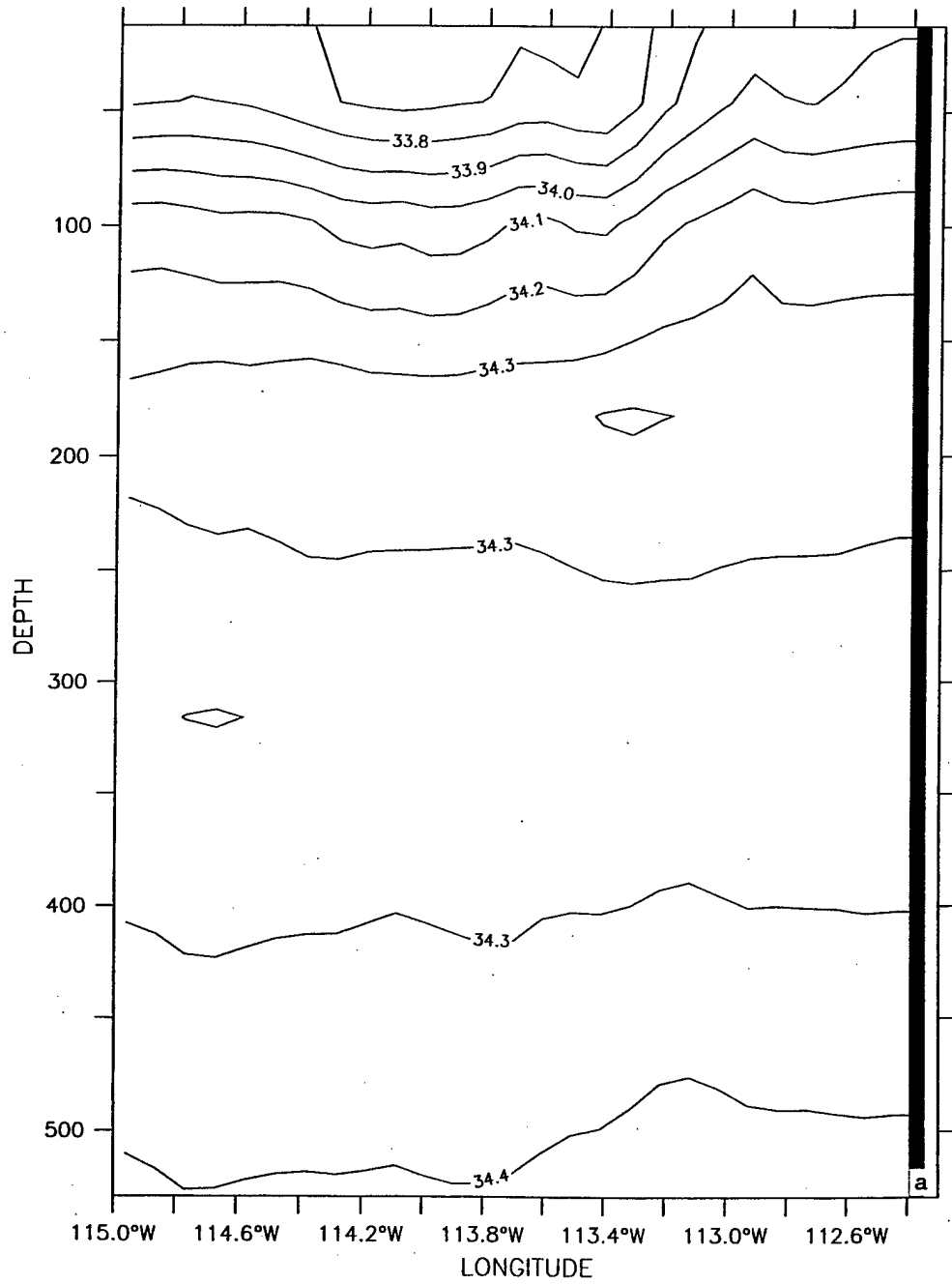


**Figure 21.** Cross-shore sections of (a) salinity on day 924 (mid-July) and (b) mean  $v$  for July of model year 3 at 26° N (south of Point Eugenia). The contour interval is 0.1 ppt in (a) and 2.5 cm/s (5 cm/s) for poleward (equatorward) flow in (b).



LATITUDE : 30.5N  
T (DAY) : 750

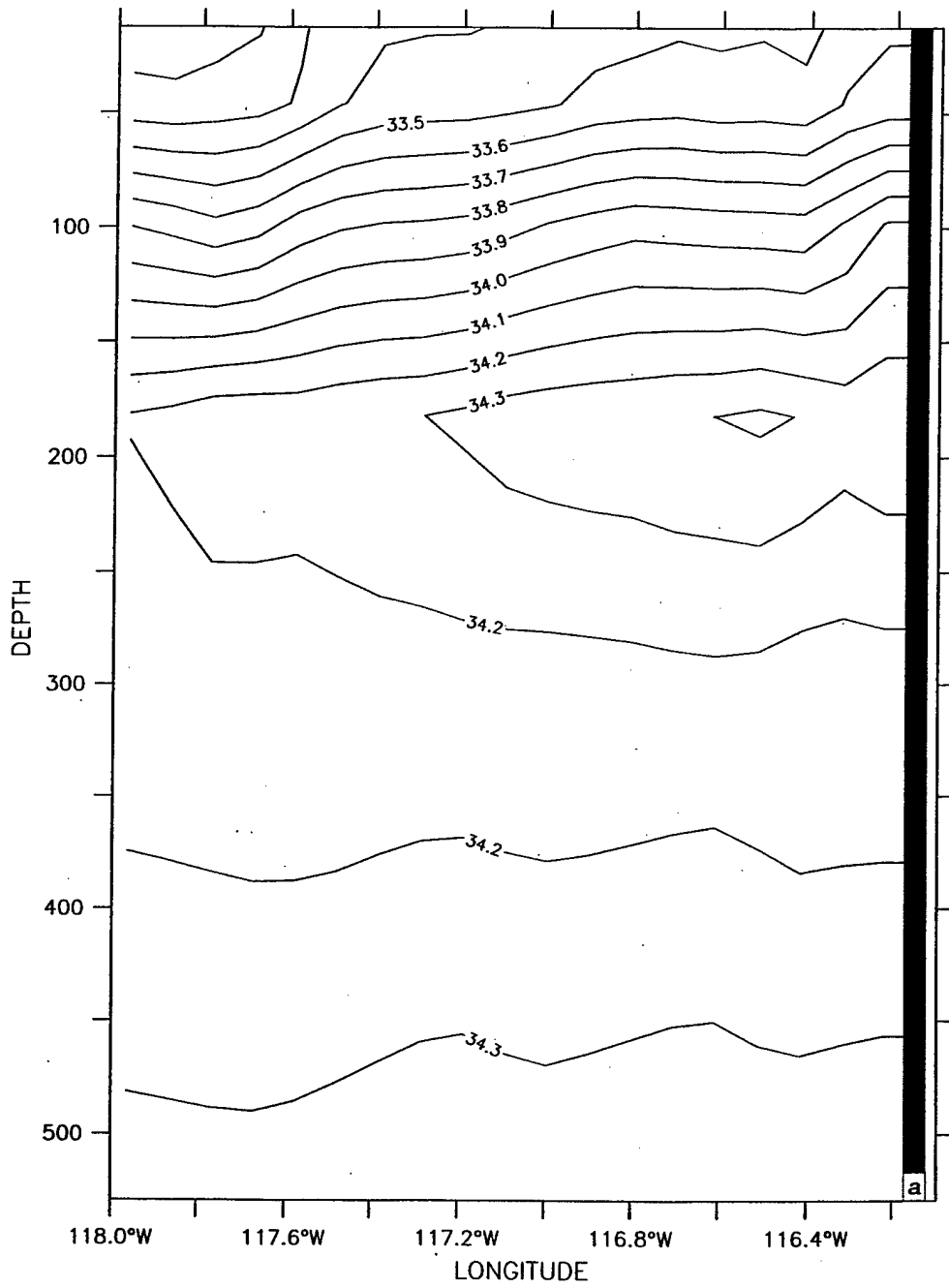
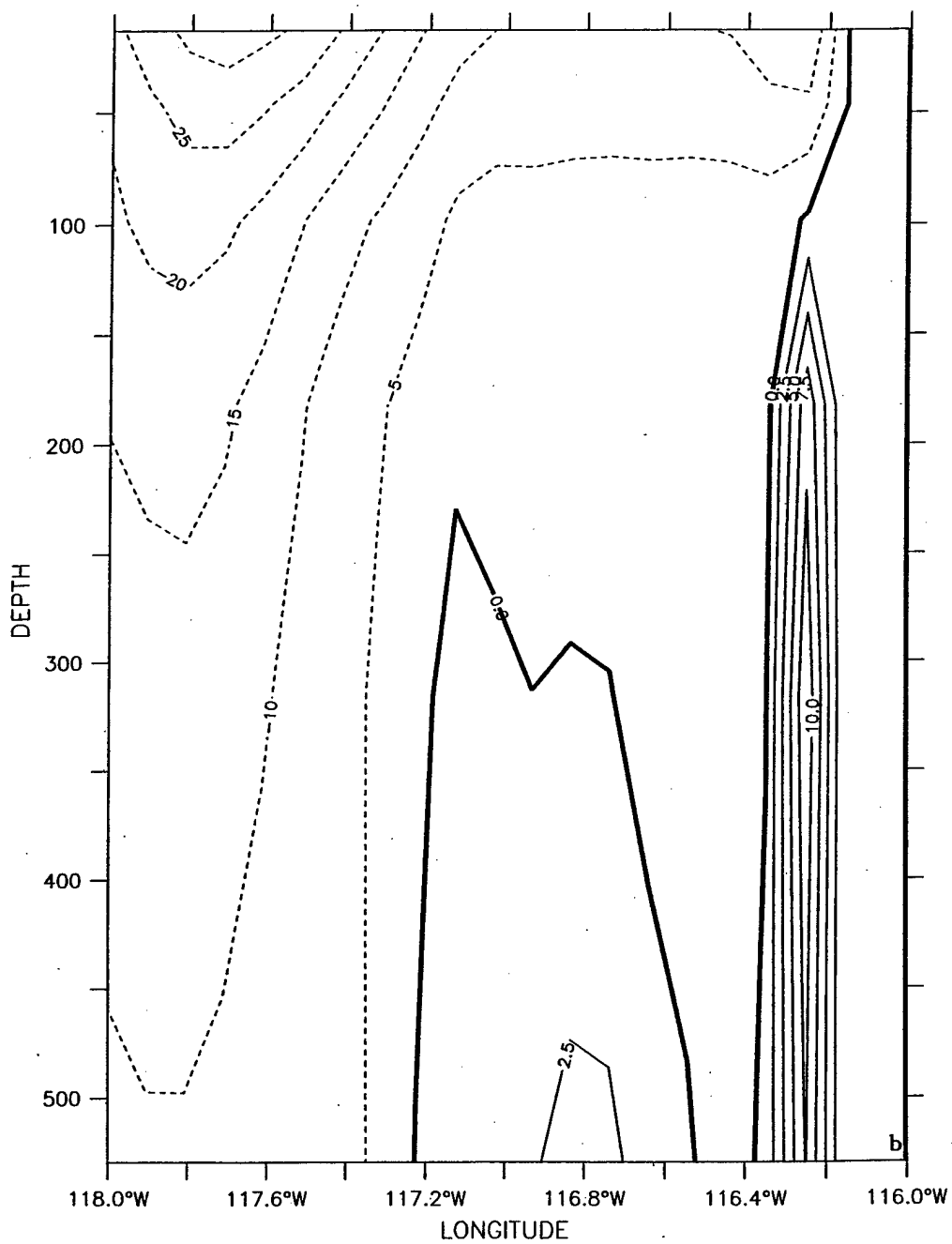


**Figure 22.** Cross-shore sections of (a) salinity on day 750 (mid-January) and (b) mean  $v$  for January of model year 3 at 30.5° N (off northern Baja). The contour interval is 0.1 ppt in (a) and 2.5 cm/s (5 cm/s) for poleward (equatorward) flow in (b).



LATITUDE : 30.5N



LATITUDE : 25N

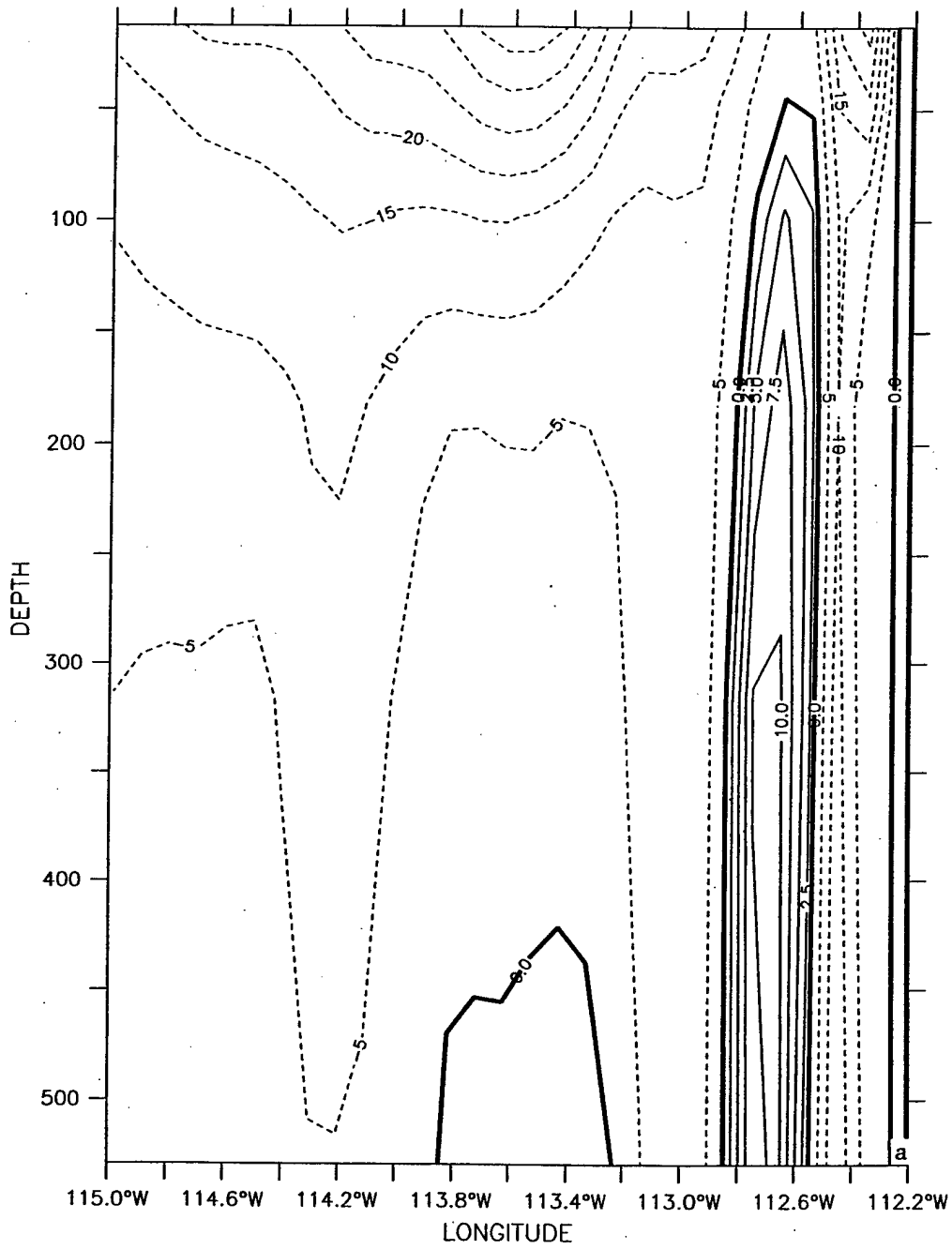
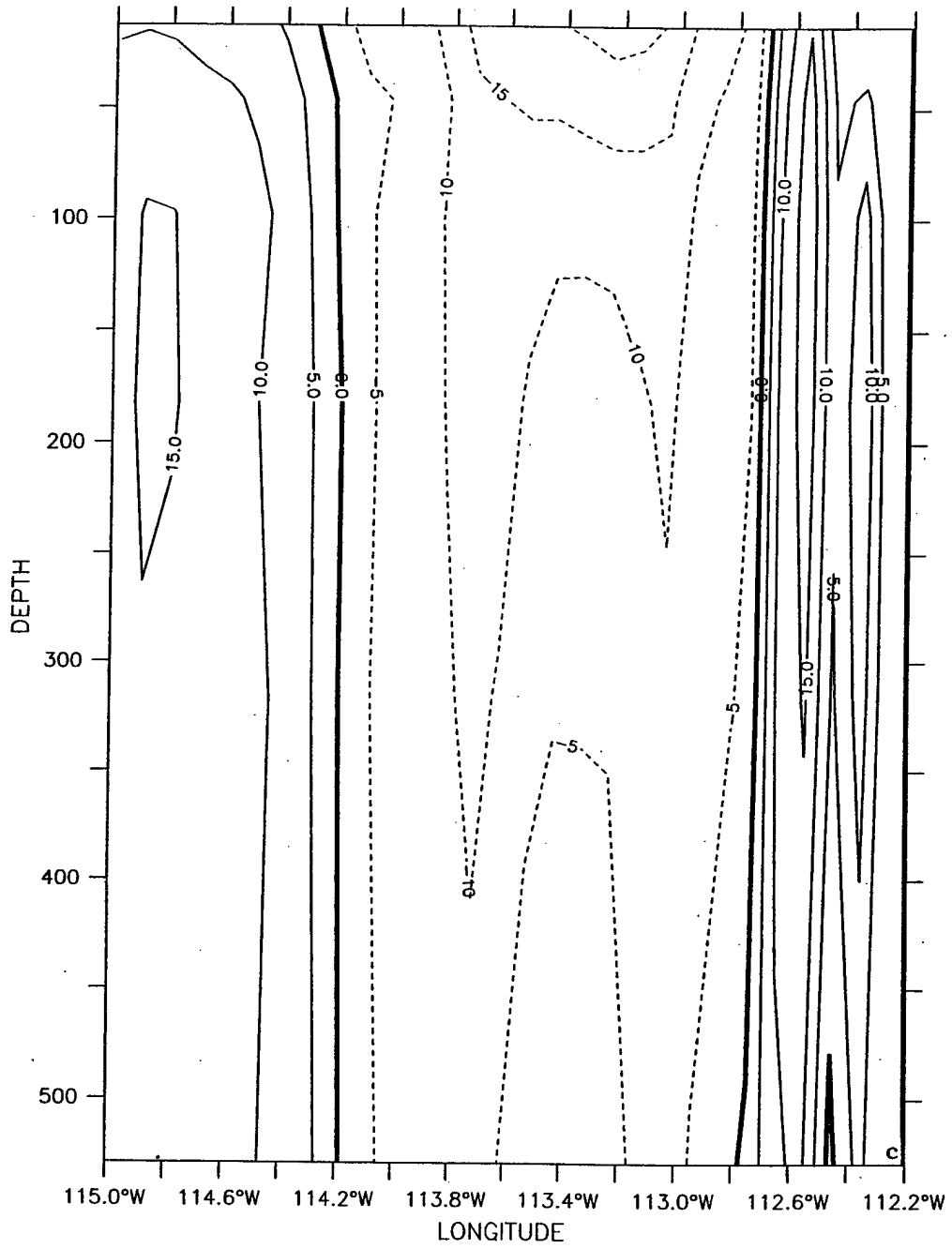


**Figure 23.** Cross-shore sections of mean  $v$  at 25° N (off Cape San Lazaro) for (a) January, (b) April, (c) July, and (d) October of model year 3. The contour interval is 2.5 cm/s (5 cm/s) for poleward (equatorward) flow in (a, b, d) and 5 cm/s for both in (c).

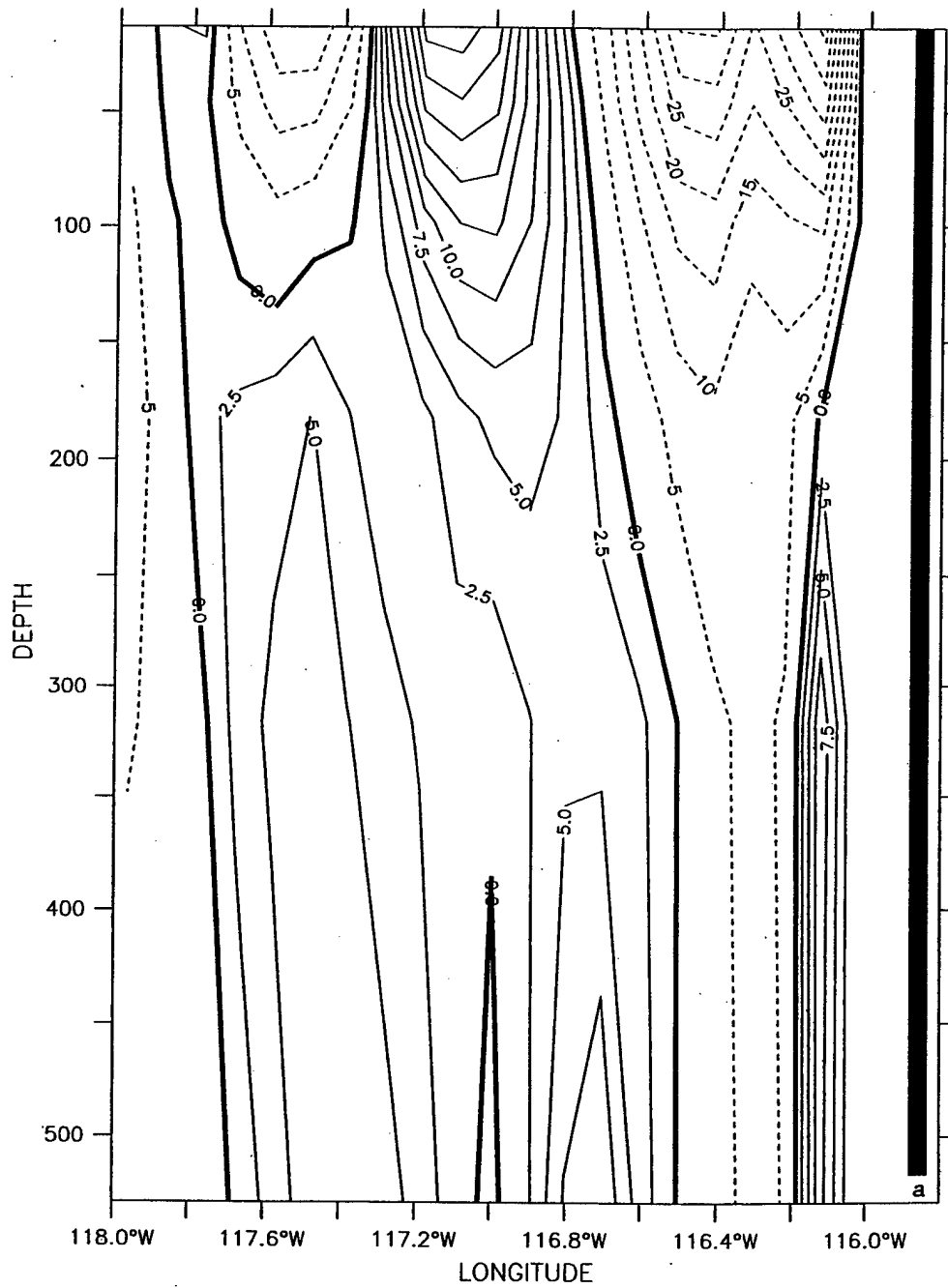


LATITUDE : 25N



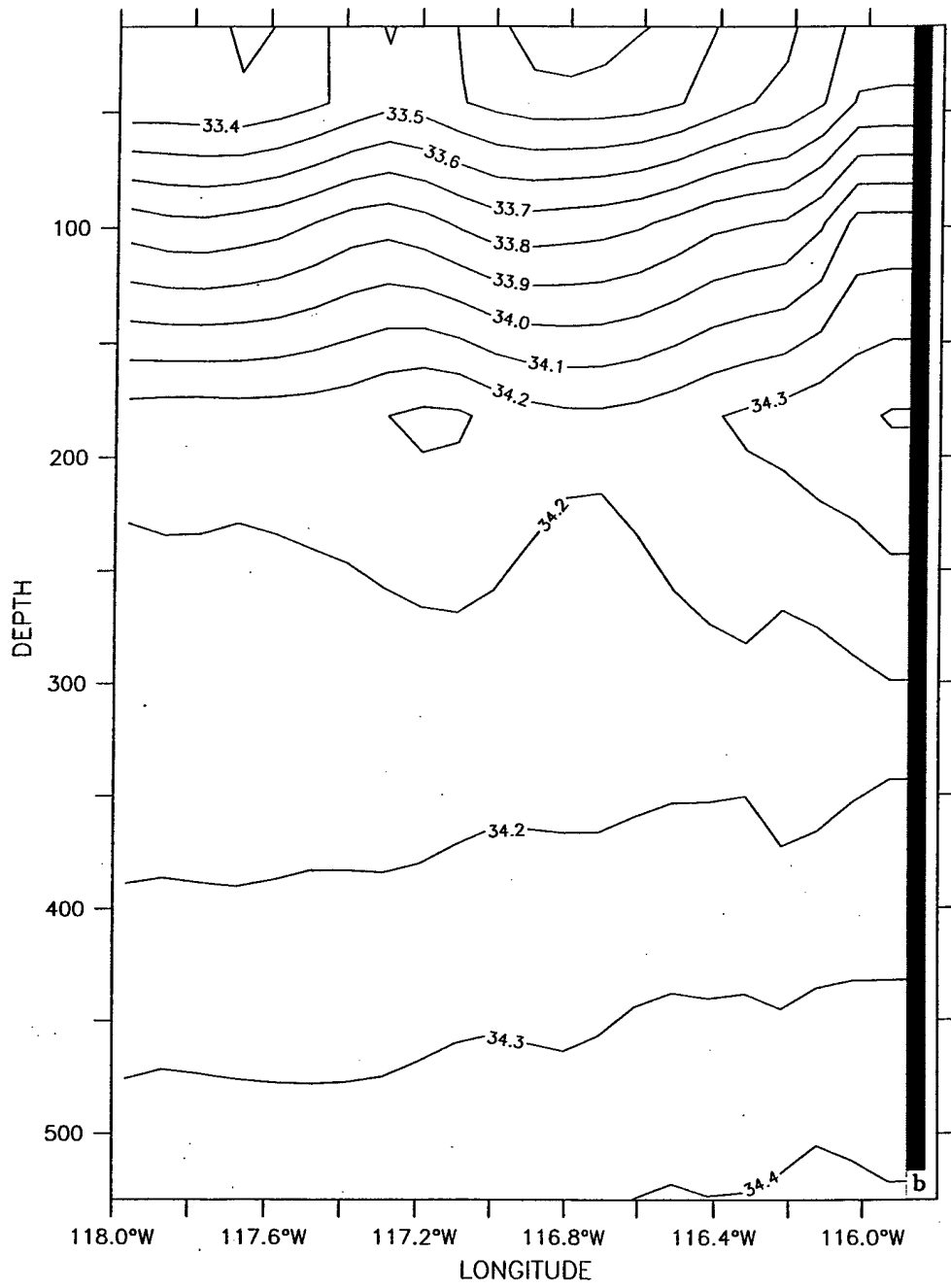


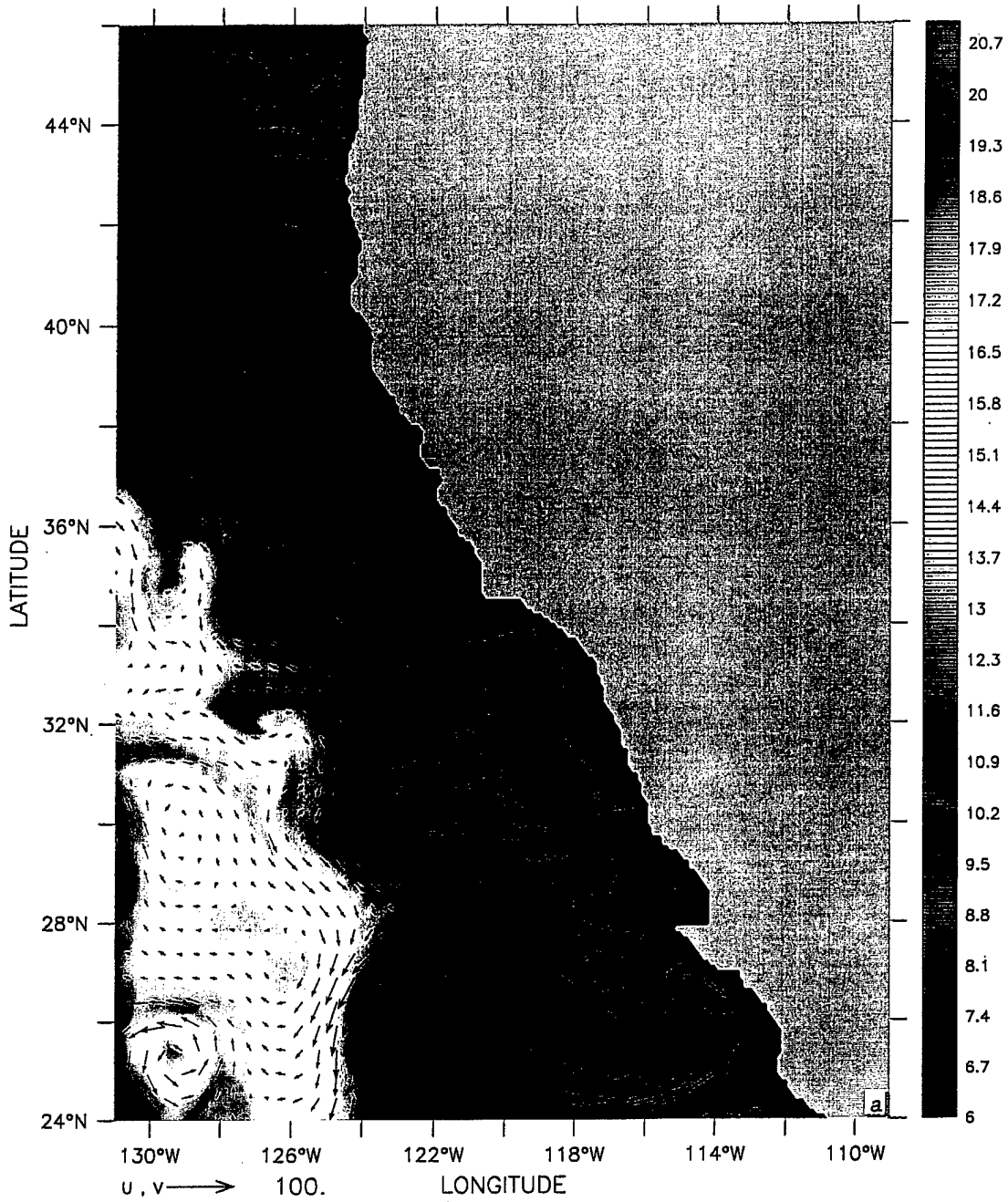
LATITUDE : 29.9N



**Figure 24.** Cross-shore sections of (a)  $v$  and (b) salinity on day 834 (mid-April) of model year 3 at  $29.9^\circ$  N (off Point Baja). The contour interval is 2.5 cm/s (5 cm/s) for poleward (equatorward) flow in (a) and 0.1 ppt in (b).

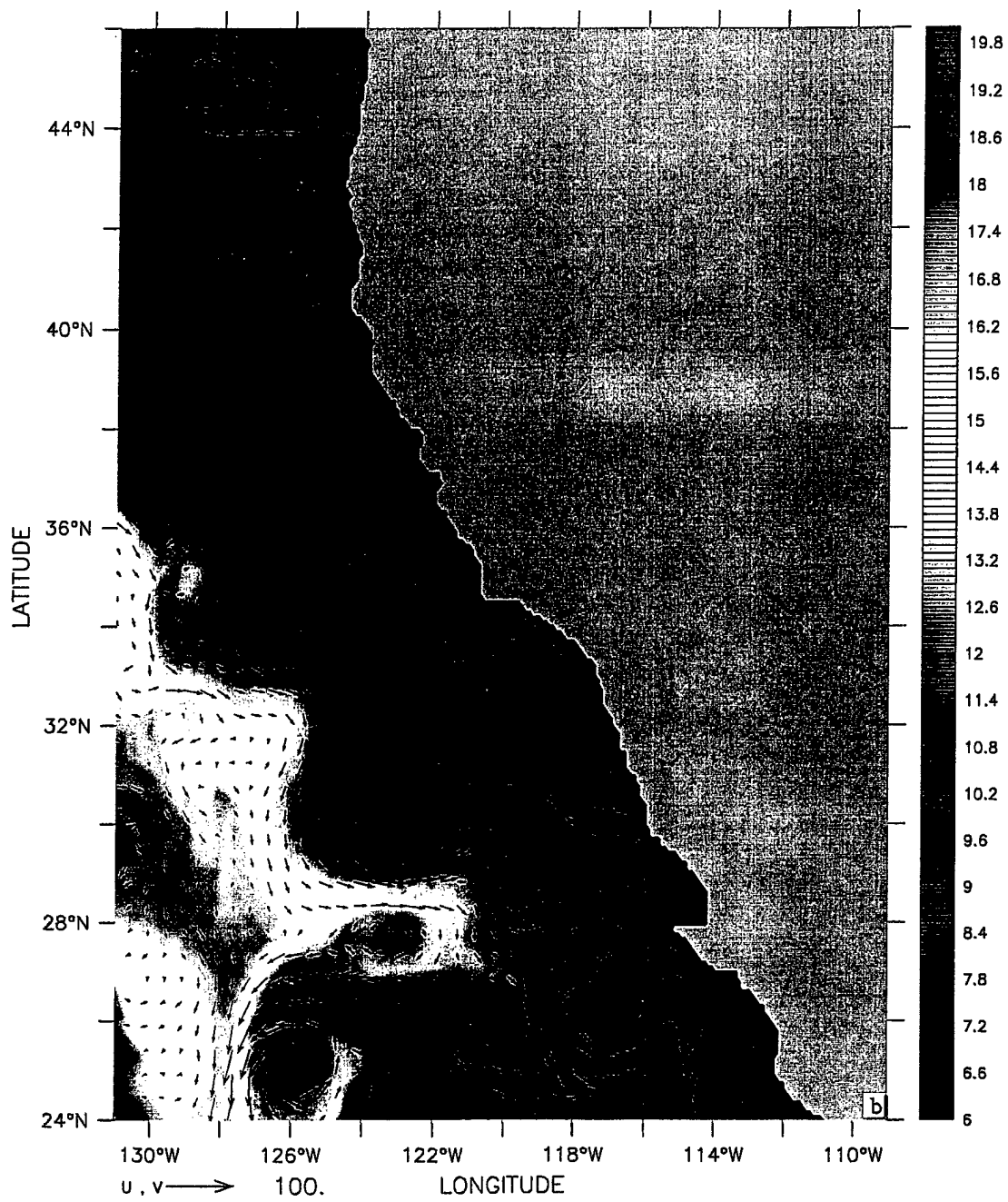
LATITUDE : 29.9N

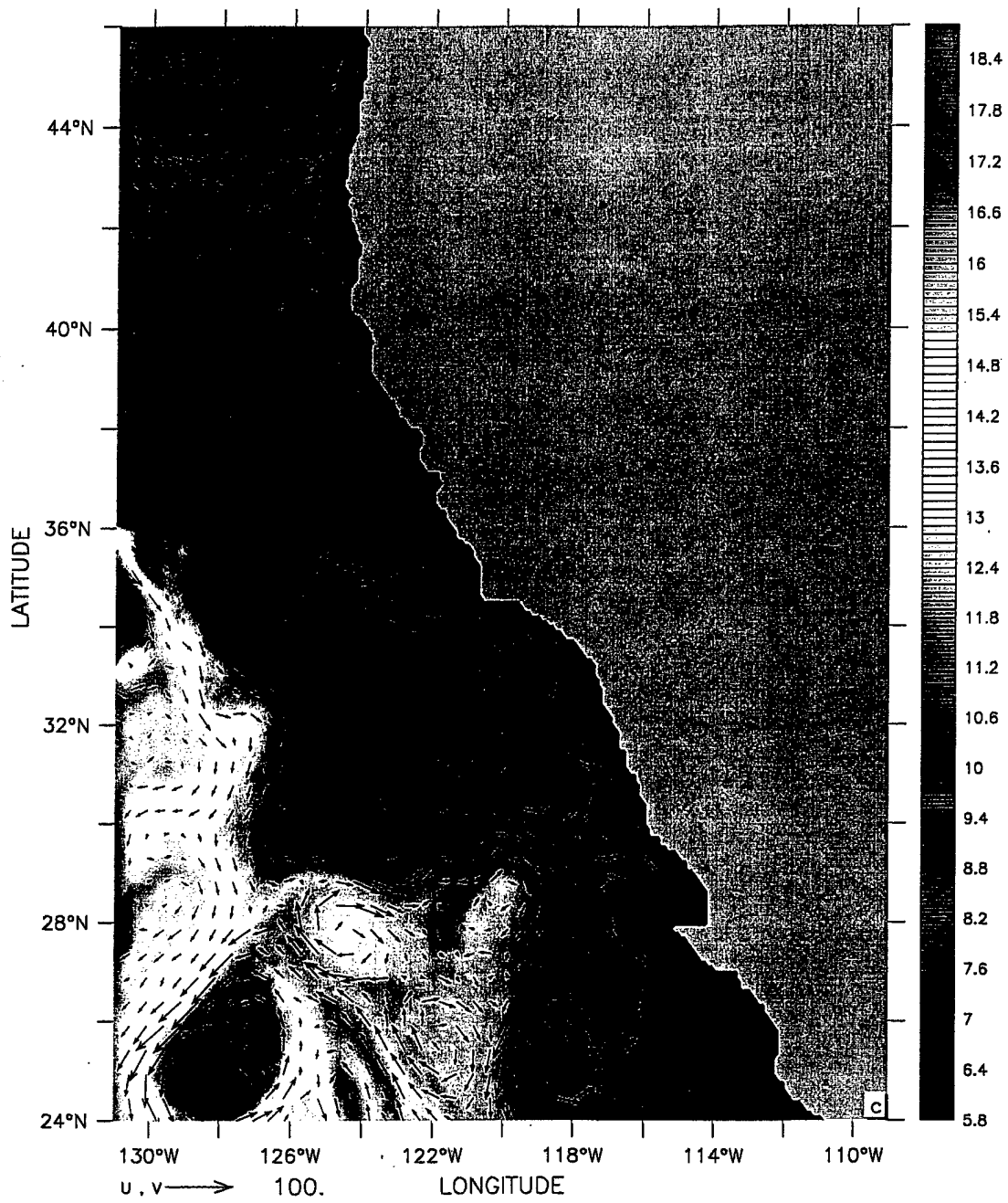




**Plate 1.** Mean temperature and velocity vectors at 13 m depth for (a) January, (b) April, (c) July, and (d) October of model year 3. Contour interval is  $0.1^{\circ}\text{C}$ ; maximum velocity vector is 100 cm/s.







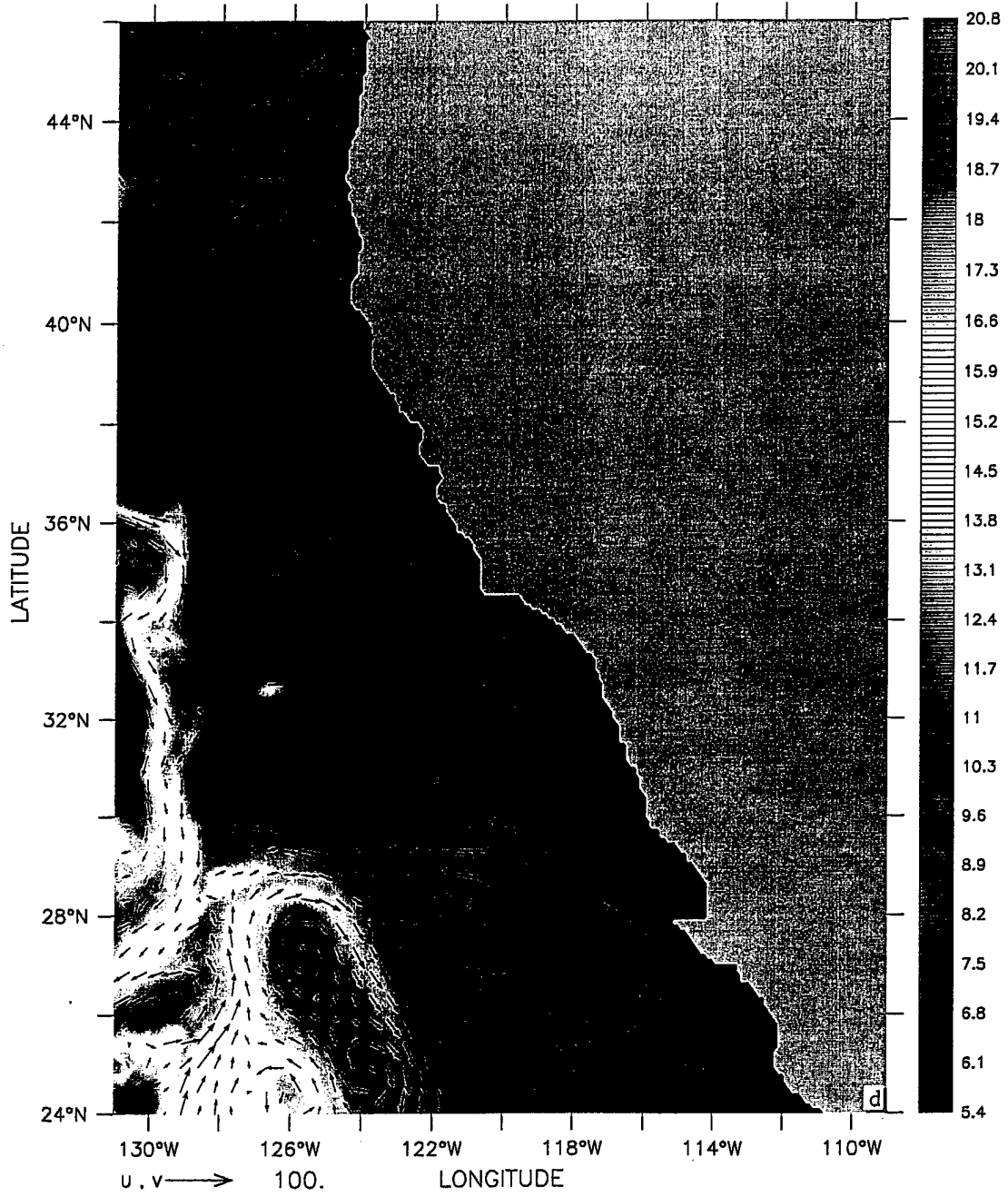


**Table 1. Values of Constants Used in the Model**

<b>Constant</b>	<b>Value</b>	<b>Definition</b>
$T_0$	278.2°K	Constant Reference Temperature
$S_0$	34.7	Constant Reference Salinity
$\rho_0$	1.0276 gm cm <sup>-3</sup>	Density of Sea Water At $T_0$ and $S_0$
$\alpha$	$2.4 \times 10^{-4}$ (°K) <sup>-1</sup>	Thermal Expansion Coefficient
$\beta$	$7.5 \times 10^{-4}$	Saline Expansion Coefficient
$K$	10	Number of Levels In Vertical
$\Delta x$	$9.0 \times 10^5$ cm	Cross-Shore Grid Spacing
$\Delta y$	$1.1 \times 10^6$ cm	Alongshore Grid Spacing
$H$	$4.5 \times 10^5$ cm	Total Ocean Depth
$\Delta t$	800 s	Time Step
$f_0$	$0.84 \times 10^{-4}$ s <sup>-1</sup>	Mean Coriolis Parameter
$g$	980 cm s <sup>-2</sup>	Acceleration of Gravity
$A_M$	$2 \times 10^{17}$ cm <sup>4</sup> s <sup>-1</sup>	Biharmonic Momentum Diffusion Coefficient
$A_H$	$2 \times 10^{17}$ cm <sup>4</sup> s <sup>-1</sup>	Biharmonic Heat Diffusion Coefficient
$K_M$	0.5 cm <sup>2</sup> s <sup>-1</sup>	Vertical Eddy Viscosity
$K_H$	0.5 cm <sup>2</sup> s <sup>-1</sup>	Vertical Eddy Conductivity

## LIST OF REFERENCES

- Arakawa, A., and V. R. Lamb, Computational design of the basic dynamical processes of the UCLA general circulation model, *Methods Comput. Phys.*, 17, 173-265, 1977.
- Auad, G., A. Pares-Sierra, and G.K. Vallis, Circulation and Energetics of a Model of the California Current System, *J. Phys. Oceanogr.*, 21, 1534-1552, 1991.
- Badan-Dangon, A., J.M. Robles, and J. Garcia, Poleward Flows Off Mexico's Pacific Coast, in *Poleward Flows Along Eastern Ocean Boundaries*, edited by S.J. Neshyba, C.N.K. Mooers, R.L. Smith, and R.T. Barber, pp. 176-202, Springer-Verlag, New York, 1989.
- Bakun, A. and C.S. Nelson, Climatology of upwelling related processes off Baja California, Calif. Coop. Oceanic Fish. Invest. Rep. 19, 107-127, 1977.
- Bakun, A. and C.S. Nelson, The seasonal cycle of wind stress curl in subtropical eastern boundary current regions, *J. Phys. Oceanogr.*, 21, 1815-1834, 1991.
- Barth, J.A., and R.L. Smith, Separation of a coastal upwelling jet and pathways for cross-shelf exchange: a Lagrangian perspective, *EOS, Trans. Amer. Geophys. Union*, Ocean Sciences Meeting suppl., OS 130, 1996a.
- Barth, J.A., and R.L. Smith, Coastal ocean circulation off Oregon: recent observations of spatial and temporal variability, in *Estuarine and Ocean Survival of Northeastern Pacific Salmon: A Workshop and Extended Abstracts*, NOAA Technical Memorandum, NMFS, NWFSC, 1996b.
- Barth, J.A., R.L. Smith, and A. Huyer, Separation of a coastal jet and cyclogenesis during coastal upwelling, *EOS, Trans. Amer. Geophys. Union*, 1994 Fall Meeting suppl., 345, 1994.
- Batteen, M.L., Wind-forced modeling studies of currents, meanders, and eddies in the California Current System, *J. Geophys. Res.*, 102, 985-1009, 1997.
- Batteen, M.L., C.A. Collins, C.R. Gunderson, and C.S. Nelson, The effects of salinity and density in the California Current System, *J. Geophys. Res.*, 100, 8733-8749, 1995.
- Batteen, M.L., R.L. Haney, T.A. Tielking, and P.G. Renaud, A numerical study of wind forcing of eddies and jets in the California Current System, *J. Mar. Res.*, 47, 493-523, 1989.

- Batteen, M.L., and Y.-J. Han, On the computational noise of finite-difference schemes used in ocean models, *Tellus*, 33, 387-396, 1981.
- Batteen, M.L., and P.W. Vance, Modeling studies of the effects of wind forcing and thermohaline gradients in the California Current System, *Deep-Sea Research*, in press, 1997.
- Batteen, M.L., M.J. Rutherford, and E.J. Bayler, A Numerical Study of Wind- and Thermal-Forcing Effects on the Ocean Circulation off Western Australia, *J. Phys. Oceanogr.*, 22, 1407-1433, 1992.
- Bernstein, R.L., L.C. Breaker, and R. Whritner, California Current eddy formation: Ship, air, and satellite results, *Science*, 195, 353-359, 1977.
- Camerlengo, A.L., and J.J. O'Brien, Open boundary conditions in rotating fluids, *J. Comput. Phys.*, 35, 12-35, 1980.
- Chelton, D.B., Seasonal variability of alongshore geostrophic velocity off central California, *J. Geophys. Res.*, 89, 3473-3486, 1984.
- Davis, R.E., Drifter observations of coastal surface currents during CODE: The method and descriptive view, *J. Geophys. Res.*, 90, 4741-4755, 1985.
- Haidvogel, D.B., A. Beckmann, and K.S. Hedstrom, Dynamical simulation of filament formation and evolution in the coastal transition zone, *J. Geophys. Res.*, 96, 15017-15040, 1991.
- Haney, R.L., A numerical study of the response of an idealized ocean to large-scale surface heat and momentum flux, *J. Phys. Oceanogr.*, 4, 145-167, 1974.
- Hickey, B.M., The California Current System - Hypothesis and facts, *Prog. Oceanogr.*, 8, 191-279, 1979.
- Hickey, B.M., Western North America, Tip of Baja California to Vancouver Island, in *The Sea*, John Wiley, New York, 1997.
- Holland, W.R., The role of mesoscale eddies in the general circulation of the ocean - Numerical experiments using a wind-driven quasigeostrophic model, *J. Phys. Oceanogr.*, 8, 363-392, 1978.

Holland, W.R., and M.L. Batteen, The parameterization of subgrid scale heat diffusion in eddy-resolved ocean circulation models, *J. Phys. Oceanogr.*, 16, 200-206, 1986.

Holland, W.R., D.E. Harrison, and A.J. Semtner Jr., Eddy-resolving numerical models of large-scale ocean circulation, in *Eddies in Marine Science*, edited by A.R. Robinson, pp. 379-403, Springer-Verlag, New York, 1983.

Huyer, A., and R.L. Smith, A subsurface ribbon of cool water over the continental shelf off Oregon, *J. Phys. Oceanogr.*, 4, 381-391, 1974.

Huyer, A., Coastal upwelling in the California Current System, *Prog. Oceanogr.*, 12, 259-284, 1983.

Ikeda, M. and W.J. Emery, Satellite observations and modeling of meanders in the California Current System off Oregon and northern California, *J. Phys. Oceanogr.*, 14, 1434-1450, 1984.

Ikeda, M., L.A. Mysak, and W.J. Emery, Observations and modeling of satellite-sensed meanders and eddies off Vancouver Island, *J. Phys. Oceanogr.*, 14, 3-21, 1984.

Kelly, K.A., R.C. Beardsley, R. Limeburner, K.H. Brink, J.D. Paduan, and T.K. Chereskin, Variability of the Near-Surface Eddy Kinetic Energy in the California Current Based on Altimetric, Drifter, and Moored Current Data, *J. Geophys. Res.*, submitted 1997.

Levitus, S., R. Burgett, and T.P. Boyer, World ocean atlas 1994, Vol. 3: Salinity, *NOAA Atlas NESDI 3*, 99 pp., U.S. Dept. of Commerce, Washington, D.C., 1994.

Levitus, S., and T.P. Boyer, World ocean atlas 1994, Vol. 4: Temperature, *NOAA Atlas NESDI 4*, 117 pp., U.S. Dept. of Commerce, Washington, D.C., 1994.

Lynn, R.J., and J.J. Simpson, The California Current System: The seasonal variability of its physical characteristics, *J. Geophys. Res.*, 92, 12947-12966, 1987.

Lynn, R.J., *Seasonal variation of temperature and salinity at 10 meters in the California Current*, Calif. Coop. Oceanic Fish. Invest. Rep. 11, 157-186, 1967.

McCreary, J.P., Y. Fukamachi, and P.K. Kundu, A numerical investigation of jets and eddies near an eastern ocean boundary, *J. Geophys. Res.*, 92, 2515-2534, 1991.

- Nelson, C.S., Wind stress and wind stress curl over the California Current, U.S. Department of Commerce, National Oceanic and Atmospheric Administration, *NOAA Technical Report NMFS SSRF-714*, 87pp., 1977.
- Niiler, P.P., P.-M. Poulain, and L.R. Haury, Synoptic three-dimensional circulation in an onshore-flowing filament of the California Current, *Deep-Sea Research*, 36(3), 385-405, 1989.
- Pares-Sierra, A., and J.J. O'Brien, The Seasonal and Interannual Variability of the California Current System: A Numerical Model, *J. Geophys. Res.*, 94, 3159-3180, 1989.
- Pares-Sierra, A., W.B. White and C.-K. Tai, Wind-driven Coastal Generation of Annual Mesoscale Eddy Activity in the California Current, *J. Phys. Oceanogr.*, 23, 1110-1121, 1992.
- Pavlova, Y.V., Seasonal variations in the California Current, *Oceanology*, 6, 806-814, 1966.
- Poulain, P.-M., Near-inertial and diurnal motions in the trajectories of mixed layer drifters, *J. Mar. Res.*, 48, 793-823, 1990.
- Poulain, P.-M., and P.P. Niiler, Statistical Analysis of the Surface Circulation in the California Current System Using Satellite-Tracked Drifters, *J. Phys. Oceanogr.*, 19(10), 1588-1603, 1989.
- Reid, J.L., Jr., Measurements of the California Countercurrent off Baja California, *J. Geophys. Res.*, 68, 4819-4822, 1963.
- Reid, J.L., Jr., Measurements of the California Countercurrent at a depth of 250 m, *J. Mar. Res.*, 20, 134-137, 1962.
- Reid, J.L. Jr., G.I. Roden, and J.G. Wyllie, Studies of the California Current System, *CalCOFI Rep. 6*, pp. 27-56, Calif. Coop. Oceanic Fish. Invest., La Jolla, 1958.
- Robinson, M.K., *Atlas of North Pacific Ocean: monthly mean temperatures and mean salinities of the surface layer*, Ref. Publ. 2, Naval Oceanographic Office, Washington, D.C., 173pp., 1976.
- Strub, P.T., P.M. Kosro, A. Huyer, and CTZ Collaborators, The nature of the cold filaments in the California Current System, *J. Geophys. Res.*, 96, 14743-14768, 1991.



Strub, P.T., and C. James, The large-scale summer circulation of the California Current, *Geophys. Res. Ltrs.*, 22, 207-210, 1995.

Trenberth, K.E., W.G. Large, J.G. Olsen, The mean annual cycle in global ocean wind stress, *J. Phys Oceanogr.*, 20, 1742-1760, 1990.

Weatherly, G.L., A study of the bottom boundary layer of the Florida Current, *J. Phys Oceanogr.*, 2, 54-72, 1972.

Wooster, W.S., and J.L. Reid, Jr., Eastern Boundary Currents in *The Sea*, Vol. 2, M. N. Hill, Ed., Wiley International, New York, 253-280, 1963.

Wooster, W.S., and Y.H. Jones, The California Undercurrent off Baja California, *J. Mar. Res.*, 28 (2), 235-250, 1970.



## INITIAL DISTRIBUTION LIST

	No. Copies
1. Defense Technical Information Center..... 8725 John J. Kingman Rd, STE 0944 Ft. Belvoir, VA 22060-6218	2
2. Dudley Knox Library..... Naval Postgraduate School 411 Dyer Rd Monterey, CA 93943-5101	2
3. Chairman (Code OC/Bf)..... Department of Oceanography Naval Postgraduate School Monterey, CA 93943-5122	1
4. Chairman (Code MR/Wx)..... Department of Meteorology Naval Postgraduate School Monterey, CA 93943-5114	1
5. Dr. Mary L. Batteen, (Code OC/Bv)..... Department of Oceanography Naval Postgraduate School Monterey, CA 93943-5122	3
6. Dr. Curtis A. Collins, (Code OC/Co)..... Department of Oceanography Naval Postgraduate School Monterey, CA 93943-5122	1
7. Dr. Richard Lambert..... National Science Foundation 4201 Wilson Boulevard Arlington, VA 22230	1
8. Dr. T. Kinder..... Physical Oceanography Division Office of Naval Research 800 N. Quiney Street Arlington, VA 22217	1

9. LCDR J.T. Monroe.....3  
159C Sloat Ave.  
Pacific Grove, CA 93950